

AD-A270 059

UMENTATION PAGE

Form Approved
GSA No. 0704 0188



This report contains information that is not to be released to the public without the approval of the appropriate authority. The information contained herein is the property of the Government and is loaned to you for your information only. It is not to be distributed outside your agency without the approval of the appropriate authority. This report is the property of the Government and is loaned to you for your information only. It is not to be distributed outside your agency without the approval of the appropriate authority.

1. AGENCY USE ONLY (Leave blank)		2. REPORT DATE Dec 93	3. REPORT TYPE AND DATES COVERED THESIS/DISSEMINATION	
4. TITLE AND SUBTITLE Correlation of Incoming Boundary Layer Pitot Pressure Fluctuations with the Unsteadiness of Fin-Inducted Shock Waves Turbulent Boundary Layer Interactions			5. FUNDING NUMBERS 1	
6. AUTHOR(S) Scott R. Nowlin				
7. PERFORMING ORGANIZATION NAME(S) AND ADDRESS(ES) AFIT Student Attending: Univ of Texas at Austin			8. PERFORMING ORGANIZATION REPORT NUMBER AFIT/CI/CIA- 93-143	
9. SPONSORING / MONITORING AGENCY NAME(S) AND ADDRESS(ES) DEPARTMENT OF THE AIR FORCE AFIT/CI 2950 P STREET WRIGHT-PATTERSON AFB OH 45433-7765			10. SPONSORING / MONITORING AGENCY REPORT NUMBER	
11. SUPPLEMENTARY NOTES				
12a. DISTRIBUTION / AVAILABILITY STATEMENT Approved for Public Release IAW 190-1 Distribution Unlimited MICHAEL M. BRICKER, SMSgt, USAF Chief Administration			12b. DISTRIBUTION CODE S DTIC ELECTE OCT 05 1993 A D	
13. ABSTRACT (Maximum 200 words)				
14. SUBJECT TERMS			15. NUMBER OF PAGES 134	
			16. PRICE CODE	
17. SECURITY CLASSIFICATION OF REPORT	18. SECURITY CLASSIFICATION OF THIS PAGE	19. SECURITY CLASSIFICATION OF ABSTRACT	20. LIMITATION OF ABSTRACT	

03 10 4 04 4

93-23212



155P8

**CORRELATION OF INCOMING BOUNDARY LAYER PITOT
PRESSURE FLUCTUATIONS WITH THE UNSTEADINESS
OF FIN-INDUCED SHOCK WAVE TURBULENT
BOUNDARY LAYER INTERACTIONS**

Accession For	
NBS CRA&I	<input checked="" type="checkbox"/>
DAAG F&E	<input type="checkbox"/>
Unpublished	<input type="checkbox"/>
Classification	
By	
Laboratory	
Administrative Codes	
Accession Number	
DAAG F&E	
A-1	

DISCONTINUED

APPROVED:

Supervisor:

David S. Dolling
Dr. David S. Dolling

Noel P. Clemens
Dr. Noel P. Clemens

Copyright
by
Scott Raymond Nowlin
1993

**CORRELATION OF INCOMING BOUNDARY LAYER PITOT
PRESSURE FLUCTUATIONS WITH THE UNSTEADINESS
OF FIN-INDUCED SHOCK WAVE TURBULENT
BOUNDARY LAYER INTERACTIONS**

by

SCOTT RAYMOND NOWLIN, B.S.

THESIS

Presented to the Faculty of the Graduate School of

The University of Texas at Austin

in Partial Fulfillment

of the Requirements

for the Degree of

MASTER OF SCIENCE IN ENGINEERING

THE UNIVERSITY OF TEXAS AT AUSTIN

December, 1993

ACKNOWLEDGMENTS

I am deeply grateful to Dr. David S. Dolling, who understood the time constraints imposed by my service in the United States Air Force and focused my research efforts accordingly. I am also indebted to the other members of the bullpen who generously shared their knowledge and time. Mehmet Erengil, Leon Brusniak, and Kelly Kleifges were especially helpful during the development and execution of the test program as well as the analysis and interpretation of data. Eddie Zhilman Jr., Joe Edgar, and Frank Wise were invaluable for their timely technical support and advice. Thanks go out to my parents, relatives, and friends from around the country who provided a constant source of encouragement. To my wife and best friend, Joelyn, thank you for your patience, understanding, strength, and unconditional love.

I gratefully acknowledge the financial support for this research provided by NASA Grant NAG1-1471, monitored by Dr. W.E. Zorumski. The valuable opportunity to complete this degree while on active duty was made possible by the United States Air Force Academy Department of Aerospace Engineering Graduate School Program under the auspices of the Air Force Institute of Technology. The United States Air Force paid all tuition and fees.

Above all, I thank our Lord Jesus Christ for His unlimited strength and endless blessings.

August 20, 1993

ABSTRACT

CORRELATION OF INCOMING BOUNDARY LAYER PITOT PRESSURE FLUCTUATIONS WITH THE UNSTEADINESS OF FIN-INDUCED SHOCK WAVE TURBULENT BOUNDARY LAYER INTERACTIONS

by

SCOTT RAYMOND NOWLIN, B.S.

SUPERVISOR: DR. DAVID S. DOLLING

This study aims to extend the current knowledge of the effects of boundary layer pitot pressure fluctuations on fin-induced separation shock wave unsteadiness. Miniature high frequency-response pressure transducers have been used to measure fluctuating pressures in a turbulent boundary layer and a separated flow induced by a blunt unswept fin. Experiments were performed in two phases under adiabatic wall conditions in a Mach 5 blowdown tunnel. In Phase 1, pitot probes were used to make mean and fluctuating measurements in a turbulent boundary layer developing naturally over a flat plate. Results of standard time series analysis and a conditional sampling algorithm indicate that the frequency band of the boundary layer/freestream interface pitot pressure fluctuations does not correlate with the frequency band of aperiodic separation shock motion in sharp fin-induced shock wave turbulent boundary layer interactions. In Phase 2, correlations between incoming boundary layer pressure fluctuations, intermittent region fluctuating wall pressures, separation shock dynamics, and fin leading edge fluctuating surface pressures were obtained

from a hemi-cylindrical fin-induced shock wave turbulent boundary layer interaction. Correlations revealed the presence of both a broad, low frequency component at approximately 500 Hz, and a high frequency component associated with turbulent structures in the incoming boundary layer. Strong correlations were observed between boundary layer pitot pressure fluctuations and the fin leading edge surface pressure fluctuations, indicating that a large fraction of turbulent structures remain coherent over a significant distance and are not greatly altered by the separation process. Ensemble-averaged pressure histories also show contributions from both low and high frequencies. The low frequencies are apparent in the gradually rising (falling) pitot pressure which correlates with a gradually rising (falling) leading edge surface pressure. High frequencies are indicated by rising-falling-rising (falling-rising-falling) pressure signatures which correspond to downstream (upstream) shock sweeps. There are also indications of a high frequency signature in the incoming boundary layer ensembles whose timing and separation distance corresponds with the separation shock motion. These results provide the first direct evidence of a correlation between upstream turbulent boundary layer pitot pressure fluctuations and separation shock dynamics. This evidence adds to a growing body of knowledge which should eventually allow accurate modelling and control of separation shock unsteadiness and associated fluctuating aeroacoustic loads.

TABLE OF CONTENTS

Section	Page
LIST OF TABLES	x
LIST OF FIGURES	xi
NOMENCLATURE	xvi
Arabic	xvi
Greek	xvii
Subscripts	xviii
Abbreviations	xix
1 INTRODUCTION	1
1.1 Overview	1
1.2 Interaction Classification	4
1.3 General Characteristics of Swept Interactions	4
1.3.1 The Sharp Fin Interaction	4
1.3.2 The Blunt Fin Interaction	7
1.4 Summary of Objectives	9
2 LITERATURE REVIEW	10
2.1 Introduction	10
2.2 Sharp Fin Interaction Mean Characteristics	11
2.2.1 Quasi-Conical Symmetry	11
2.2.2 Wall Mean and RMS Pressure Distributions	12
2.2.3 Flowfield Structure	13
2.2.4 CFD Results	16
2.3 Blunt Fin Interaction Mean Characteristics	17
2.3.1 Wall Mean and RMS Pressure Distributions	17
2.3.2 Leading Edge Pressures	18
2.3.3 Flowfield Structure	18
2.3.4 CFD Results	19
2.4 Interaction Unsteadiness	20
2.4.1 Characteristics	21

2.4.2	Driving Mechanisms	24
2.5	Summary	26
3	EXPERIMENTAL PROGRAM	28
3.1	Introduction	28
3.2	Wind Tunnel Facility	28
3.3	Instrumentation	29
3.4	Phase 1: Turbulent Boundary Layer Study Test Setup	31
3.5	Phase 1: Experimental Procedures	32
3.5.1	Freestream Flow Conditions	32
3.5.2	Undisturbed Boundary Layer Survey	33
3.5.2.1	Mean Boundary Layer Properties	34
3.5.3	Boundary Layer/Freestream Interface Characteristics	34
3.6	Phase 2: Blunt Fin-Induced Interaction Test Setup	35
3.7	Phase 2: Experimental Procedures	36
3.7.1	Freestream Flow Conditions and Boundary Layer Properties	36
3.7.2	Simultaneous Intermittent Region and Leading Edge Pressure Measurements	37
3.7.3	Probe-Wall Interference Test	38
3.7.4	Simultaneous Near-Wall Boundary Layer, Intermittent Region, and Leading Edge Pressure Measurements	39
4	ANALYSIS TECHNIQUES	40
4.1	Standard Statistical and Time Series Analysis	40
4.2	LEAST Analysis of Mean Boundary Layer Properties	40
4.3	Two Threshold Method For Separation Shock Statistics	42
4.4	VITA Conditional Sampling Technique	43
4.5	Separation Shock Position and Velocity Histories	44
5	RESULTS	46
5.1	Probe/Wall Interference Tests	46
5.2	Phase 1: Turbulent Boundary Layer Study	47
5.2.1	Boundary Layer Survey	47
5.2.2	Mean Boundary Layer Properties	47

5.2.3	Boundary Layer/Freestream Interface Fluctuating Characteristics	49
5.3	Phase 2: Blunt Fin-Induced Interaction	51
5.3.1	Upstream Near-Wall Pitot Probe Signal Characteristics	52
5.3.2	Intermittent Region Wall Pressure Signal Characteristics	52
5.3.3	Separation Shock Dynamic Characteristics	54
5.3.4	Leading Edge Stagnation Pressure Signal Characteristics	55
5.3.5	Summary of Upstream Probe Effects on Interaction Characteristics	56
5.3.6	Cross-Correlations	56
5.3.6.1	Correlations Between Pressure Fluctuations Only	57
5.3.6.2	Correlations Between Pressure Fluctuations and Shock Dynamics	60
5.3.7	Ensemble-Averaged Pressure Histories	61
6	CONCLUSIONS AND RECOMMENDATIONS	64
6.1	Conclusions	64
6.2	Recommendations for Future Work	67
	FIGURES	68
	REFERENCES	128
	VITA	135

LIST OF TABLES

Table	Title	Page
3-1:	Kulite Transducer Specifications	30
3-2:	Phase 1 Freestream Flow Conditions	32
3-3:	Flat Plate Mean Boundary Layer Properties	34
3-4:	Phase 2 Freestream Flow Conditions	36
3-5:	Tunnel Wall Mean Boundary Layer Properties (McClure 1991)	37
5-1:	Differences in Flat Plate Mean Boundary Layer Properties Between Gibson (1990) and the Current Study	48

LIST OF FIGURES

Figure	Title	Page
1-1:	Blunt Fin Interaction Features and Nomenclature (Lakshamanan and Tiwari 1993, Brusniak 1989)	68
1-2:	Swept Shock Wave Boundary Layer Interaction Classification (Settles and Dolling 1986)	69
1-3:	Sharp Fin Interaction (a) Features and Nomenclature, (b) Coordinate System (Settles and Dolling 1990)	70
2-1:	Quasi-Conical Collapse of (a) Surface Pressure Measurements (Zubin and Ostapenko 1979) and (b) PLS Images (Alvi and Settles 1990)	71
2-2:	Mean Pressure Distribution, Mach 3 Sharp Fin Interaction (Tran 1987)	72
2-3:	RMS Pressure Distribution, Mach 3 Sharp Fin Interaction (Tran 1987)	73
2-4:	Quasi-Conical Collapse of Normalized Distributions, Mach 5 Sharp Fin Interaction (Schmisser 1992)	74
2-5:	Inception Region Effects on Quasi-Conical Mean Pressure Distribution, Mach 3.44, $\alpha = 14^\circ$ (Lu 1993)	75
2-6:	(a) Shadowgraph, (b) PLS Image, and (c) Flowfield Map for Mach 4, $\alpha = 20^\circ$ Sharp Fin Interaction (Alvi and Settles 1990, 1991)	76
2-7:	Mean and RMS Pressure Distributions with Corresponding Flowfield, Mach 4, $\alpha = 20^\circ$ Sharp Fin Interaction (Garg and Settles 1993)	77
2-8:	Flowfield Pressure Contours, Mach 8.2, $\alpha = 15^\circ$ Sharp Fin Interaction (Kussoy and Horstman 1993)	78

2-9:	Experimental and Computed Mean Wall Pressures, Mach 3, $\alpha = 17.5^\circ$ Sharp Fin Interaction (Zang and Knight 1989)	79
2-10:	Mach 3 Blunt Fin Interaction Mean Wall Pressure Distributions, (a) Experimental (Dolling and Bogdonoff 1982) and (b) Experimental and Computational (Hung and Buning 1985)	80
2-11:	(a-c) Mach 3 Blunt Fin Interaction Leading Edge Mean Pressure Distributions (Dolling and Bogdonoff 1982)	81
2-12:	Mach 3 Blunt Fin Interaction (a) Experimental and Computational Leading Edge Mean Pressure Distribution, and (b) Particle Flow Paths on Centerline (Hung and Buning 1985)	82
2-13:	(a-h) Surface Pressure Signals Beneath the Translating Separation Shock Upstream of a Compression Corner, Mach 5, $\alpha = 17.5^\circ$ (McClure 1992)	83
2-14:	(a-e) Wall Intermittent Pressure Signals and Probability Density Distributions from a Mach 3 Blunt Fin Interaction (Dolling and Bogdonoff 1981)	84
2-15:	Surface Pressure Probability Density Distributions Upstream of a Compression Corner, Mach 5, $\alpha = 17.5^\circ$ (McClure 1992)	85
2-16:	(a-f) Wall Pressure Signals, PDDs and PSDs, Mach 5 Sharp Fin Interaction (Schmisseur 1992)	86
2-17:	Effects of Interaction Sweep on PSDs, Mach 5 Compression Ramp Interactions (Erengil and Dolling 1993a)	87
2-18:	Sharp Fin Interaction PSDs, Mach 5, $\alpha = 18^\circ$ (Gibson 1990)	88
2-19:	(a) RMS Pressure Distribution and (b) PSDs, Mach 5 Cylinder- Induced Interaction (Brusniak 1991)	89
2-20:	Mach 5, 28° Compression Ramp Ensemble-Averaged Wall Pressure Histories, 3-Channel (a) Downstream and (b) Upstream Sweeps (Trigger on Channel 7) (McClure 1992)	90

2-21: Qualitative Model of Fin-Induced Interaction Separated Region Recirculation (Kleifges 1993)	91
3-1: Phase 1 Test Setup	92
3-2: Pitot Probes	93
3-3: Phase 2 Test Setup	94
3-4: Blunt Fin Body and Instrumented Leading Edge	95
3-5: Near-Wall Boundary Layer Probe	96
4-1: Two-Threshold Method (Erengil 1989)	97
4-2: Determination of $X_S(t)$ and $V_S(t)$ from Nested Boxcar Signals (Erengil and Dolling 1993a)	98
5-1: Probe Interference Effects on Wall Static Pressure and Pitot Pressure	99
5-2: Boundary Layer (a) Pitot Pressure Profile and (b) u^+ , y^+ Velocity Profiles from the Current Study and Gibson (1990)	100
5-3: Boundary Layer/Freestream Intermittency and Interface Crossing Frequency Distributions	101
5-4: Boundary Layer/Freestream Intermittency Profile	102
5-5: Boundary Layer/Freestream Interface Crossing Frequency Profile	103
5-6: Turbulent Boundary Layer/Mach 5 Freestream Interface Region Raw Data Signals, PDDs, and PSDs (McClure 1992)	104
5-7: Turbulent Boundary Layer/Mach 5 Freestream Interface Region Raw Data Signals, PDDs, and PSDs	106
5-8: Pitot Probe Raw Data Signals, PDDs, and PSDs; $X/D = -10.73$ ($X/\delta_0 = 13.64$)	108
5-9: Intermittent Region Raw Data Signals, PDDs, and PSDs; No Upstream Probe	109

5-10: Intermittent Region Raw Data Signals, PDDs, and PSDs; Upstream Probe at $X/D = -10.73$, $Z/\delta_o = 0.51$	111
5-11: Blunt Fin Interaction Intermittent Region Pressure Distributions	113
5-12: Blunt Fin Interaction Intermittency and Zero Crossing Frequency Profiles	114
5-13: Characteristic Separation Shock Position and Velocity Histories and PSDs	115
5-14: Leading Edge Surface Pressures - Raw Data Signals, PDDs, and PSDs; No Upstream Probe	116
5-15: Blunt Fin Leading Edge Mean and RMS Pressures	117
5-16: Leading Edge Surface Pressures and the Fluctuating Pitot Pressure at $X/D = -10.73$, $Z/\delta_o = 0.51$	118
5-17: Cross-Correlation Between Fluctuating Surface Pressures at the Fin Leading Edge and Pitot Pressure Fluctuations at $X/D = -10.73$	119
5-18: Cross-Correlations Between Intermittent Region Fluctuating Wall Pressures and Fin Leading Edge Fluctuating Surface Pressure at $Z/D = 0.54$	120
5-19: Cross-Correlations Between Intermittent Region Fluctuating Wall Pressures and Leading Edge Fluctuating Surface Pressure at $Z/D = 0.40$	121
5-20: Cross-Correlations Between Separation Shock Dynamics and Fluctuating Pitot Pressures at $X/D = -10.73$	122
5-21: Cross-Correlations Between Separation Shock Dynamics and Fluctuating Fin Leading Edge Surface Pressures at $Z/D = 0.38$	123
5-22: Ensemble-Averaged Pressure Histories, Downstream Sweep Over Channel 1	124
5-23: Ensemble-Averaged Pressure Histories, Downstream Sweep Over Channel 4	125

5-24: Ensemble-Averaged Pressure Histories, Upstream Sweep Over Channel 6	126
5-25: Ensemble-Averaged Pressure Histories, Upstream Sweep Over Channel 4	127

NOMENCLATURE

Arabic

$a(y)$	local speed of sound
A, B	signatures of interest in ensemble pressure histories
C_f	skin friction coefficient
D	fin thickness; fin leading edge diameter
dp_e/dx	non-dimensional pressure gradient
f_s	sampling frequency
f_c	zero-crossing frequency
f_i	interface crossing frequency
G(f)	power spectral density
h	fin height
H	shape factor, δ^*/θ
K	VITA threshold level
M	Mach number
M(y)	local Mach number
P_1	static pressure upstream of shock
P_2	static pressure downstream of shock
P1, P2	peaks in normalized cross-correlation
P_{LE}	surface pressure at the fin leading edge
P_o	stagnation pressure
P_{t2}	freestream pitot pressure
$P_{t2}(Z)$	local pitot pressure
$P_w(t)$	instantaneous wall static pressure

\bar{P}_w	mean wall static pressure
$\bar{P}_{w_\infty}, P_\infty$	freestream static pressure
q_w	heat transfer rate
r	radial distance in spherical/polar reference frame
Re_∞	freestream unit Reynolds number
s	radial distance in spherical/polar reference frame
S	blunt fin interaction separation line
t	time
T_0	stagnation temperature
T_{st}	VITA window size
$u(y)$	local velocity
u_c	convection velocity
u^+	dimensionless boundary layer coordinate velocity, u/u_τ
u_τ	friction velocity
U	blunt fin interaction upstream influence line
U_∞	freestream velocity
$V_s(t)$	separation shock foot velocity time history
$X_s(t)$	separation shock foot position time history
y	height above wall or plate
y^+	normalized boundary layer coordinate, yu_τ/ν

Greek

α	sharp unswept fin angle of attack
β	angle in spherical/polar coordinates

β_{a1}	primary reattachment line angle
β_o	inviscid shock trace
β_u	upstream influence angle
β_{s1}	primary separation line angle
β_{s2}	secondary separation line angle
δ	undisturbed boundary layer thickness; height at which $u(y) = 0.99U_\infty$
δ_1	boundary layer mass flux thickness
δ^*	boundary layer displacement thickness
ϕ	angle in spherical/polar coordinates
γ	intermittency
Π	Coles wake parameter
θ	boundary layer momentum thickness
σ	standard deviation
σ_{pw}	local wall RMS pressure
σ^2	variance
τ	time delay
ζ	length unit of convenience equal to 0.115 inches; minimum machineable distance between transducers.

Subscripts

LE	quantity measured at the leading edge
n	normal
st	short-term
w	quantity measured at the tunnel wall
∞	quantity measured in the freestream

Abbreviations

CFD	computational fluid dynamics
DAS	data acquisition systems
E-A	ensemble-averaged
F-R-F	fall-rise-fall (in ensemble-averaged pressure histories)
FSO	full scale output
LE	leading edge
LVDT	linear variable displacement transducer
NASP	X-30 national aerospace plane
PDD	amplitude probability density distribution
PLS	planar laser scattering
PSD	power spectral density distribution
R-F-R	rise-fall-rise (in ensemble-averaged pressure histories)
RMS	root mean square
SSTO	single-stage-to-orbit aerospace vehicle
VCO	virtual conical origin
VITA	variable-interval time-averaging conditional sampling technique

CHAPTER 1

INTRODUCTION

1.1 Overview

Aeroacoustic loads are of critical importance to those working on current transatmospheric airbreathing vehicle designs. Turbulent boundary layers, propulsion systems, shock-shock interactions, and shock wave boundary layer interactions all generate unsteady fluctuating surface pressures and heat transfer rates whose instantaneous amplitudes at a given surface position can be several times mean values. In the high speed, high energy flight regime of vehicles such as the national aerospace plane (NASP) or other single-stage-to-orbit (SSTO) vehicle concepts, aeroacoustic loads generated by control surfaces, at wing-body junctions, and in engine inlets and nozzles will reduce the operating life of structural materials by orders of magnitude (Pozefsky et al. 1989). Flow separation in and around these areas are of particular concern as it not only adversely affects propulsion system compression and combustion processes as well as vehicle aerodynamics, but also results in increased fluctuating loads. In short, if these loads are not correctly predicted and structurally accounted for, catastrophic failures could result.

Swept shock wave turbulent boundary layer interactions in particular can result in severe stresses on the vehicle structure. Such interactions occur when a supersonic (or hypersonic) flow passes over a fin, step, compression corner, or other shock-generating body. For example, Figure 1-1 shows a swept interaction generated by a blunt fin. The inviscid bow shock generated by the fin bifurcates at its base into a λ -foot. The upstream leg of the λ -foot, the *separation shock*, extends

from the *triple point* downwards to a *shock foot* close to the surface. The separation shock, where the flow first encounters the adverse pressure gradient created by the inviscid shock, translates aperiodically in the streamwise direction across the *intermittent region*. Any point within this region is alternately exposed to the static pressure of the incoming boundary layer (relatively low values), the separated flow (relatively high values), or rises and falls in pressure associated with shock foot passages. The characteristic pressure signals generated underneath the translating separation shock and the separated flow are shown in the insets of Figure 1-1. The separated flow is organized into one or more pairs of *horseshoe vortices* which trail downstream.

A historical example illustrating the detrimental results of this type of interaction is summarized in the November, 1967 flight of a NASA X-15 hypersonic aircraft. A ramjet engine mockup attached to a fuselage-mounted pylon was carried to a speed of Mach 6. An interaction between the bow shock in front of the pylon and the turbulent boundary layer across the fuselage prematurely eroded the fuselage's protective ablative coating and buckled the titanium skin (Burcham and Nugent 1970).

Recent experimental work cited by Zorumski (1987) has confirmed that the highest aeroacoustic loads are found in turbulent separated flows induced by shock waves. Predicting these unsteady fluctuating pressure loads is challenging. Although advances in computational methods and hardware makes computational fluid dynamics (CFD) an ever-more powerful design tool and performance predictor, only the *time-averaged* flowfield characteristics of shock wave turbulent boundary layer interactions are currently reproducible with CFD models. Thus, while CFD offers a

time-saving, cost-effective alternative to wind tunnel or flight tests, investigations of the flowfield unsteadiness require experimental data.

To simulate the separation shock unsteadiness, future CFD algorithms must accurately model the physics inherent in the driving mechanisms of the shock dynamics. One identified mechanism is the passage of turbulent structures from the incoming boundary layer through the shock (Brusniak 1991, McClure 1992, Erengil 1992). A second, of particular importance in blunt fin interactions, is the recirculation of turbulent structures within the separated region downstream of the separation shock (Kleifges 1993). Quantifying the contributions of these different mechanisms to unsteady separation shock dynamics is the subject of many current research efforts (Brusniak and Dolling 1993, Erengil and Dolling 1993b).

This thesis presents the experimental techniques and results associated with a study of the relationship between turbulent boundary layer pitot pressure fluctuations and the unsteadiness of unswept sharp and blunt fin-induced shock wave turbulent boundary layer interactions. Section 1.2 briefly introduces the classification of these interactions. To make the objectives clear, Section 1.3 presents overall mean and unsteady features of sharp and blunt fin-induced interactions. The specific goals of this thesis are then provided in Section 1.4. Chapter 2 discusses important theoretical and experimental results found in the literature that are critical to the objectives of this work. Chapter 3 describes the experimental setup and procedures used, while Chapter 4 provides information on the data analysis procedures applied. Results are presented in Chapter 5. Chapter 6 summarizes the study conclusions and presents recommendations for future work on this subject.

1.2 Interaction Classification

Figure 1-2 presents the accepted classification scheme for swept shock wave boundary layer interactions. In *semi-infinite* interactions, a change in the length or height of the shock generator does not change the interaction flowfield characteristics. Semi-infinite interactions are delineated further into *dimensionless* interactions whose shock generators do not impose a geometric length scale on the interaction, and *dimensional* interactions, which are affected by some characteristic length scale of the generator, such as its height or thickness. As shown in Figure 1-2, the sharp unswept fin-induced interaction is semi-infinite and dimensionless, while the unswept blunt fin-induced interaction is semi-infinite but dimensional in D , the fin thickness. Thus the scales of the blunt fin-induced interaction flowfield are controlled to the first order by D .

1.3 General Characteristics of Swept Interactions

1.3.1 The Sharp Fin Interaction

Figure 1-3 shows the standard flowfield nomenclature and coordinate system for a sharp unswept fin-induced shock wave boundary layer interaction, hereafter referred to as a sharp fin interaction. The fin is at an angle of attack, α , with respect to the freestream. The fin leading edge generates a planar, attached shock wave whose angle, β_0 , can be determined from inviscid theory. The interaction strength is set by the Mach number normal to the inviscid shock, M_n . A rise in M_∞ at a constant α , or increasing α under constant M_∞ conditions, will increase M_n and the interaction strength.

Figure 1-3(a) shows the mean features of the interaction. The planar inviscid shock bifurcates into the characteristic λ -foot. The separation shock extends downward towards β_u , the *upstream influence* line, which is the mean upstream limit of the interaction and the line along which the mean pressure rise is first detected. It is also apparent from surface flow visualization as an initial deflection of surface streaklines from the streamwise direction. If the interaction strength is sufficient, the flow separates along a line at β_{s1} and forms a spiraling helical vortex. Above this region, the rear shock extends downward from the λ -foot into the separated flow. The flow is turned downwards by this shock and reattaches at a line at angle β_{a1} . Seldom seen in experiments is a secondary separation at β_{s2} .

The sharp fin interaction is commonly presented in the spherical/polar reference frame shown in Figure 1-3(b) due to its *quasi-conical* nature (Settles and Lu 1985, Alvi and Settles 1991). Quasi-conical symmetry simplifies the inherently three dimensional flowfield by defining its properties in only two dimensions. This is discussed in further detail in Section 2.2.1.

Surface pressure measurements made under the initial compression and separated flow regions of sharp fin interactions have indicated high mean and RMS pressure levels (Tran et al. 1985, Gibson and Dolling 1991, Schmisser and Dolling 1992). For example, at $M_\infty = 5$, the mean static wall pressure, \bar{P}_w , approximately doubles as it rises from the upstream influence line to a plateau in the separated region. \bar{P}_w then increases sharply near the fin root, finally reaching the inviscid level. The RMS pressure, σ_{p_w} , begins to increase upstream of separation from approximately $0.02 \bar{P}_w$ to $0.10 \bar{P}_w$ or more before decreasing to approximately $0.075 \bar{P}_w$ in the separated region. The RMS level increases again near β_o before

decreasing to approximately $0.05 \bar{P}_w$ near the fin root. Mean and RMS pressure peak levels increase with M_n . Physical flow phenomena associated with the distribution characteristics are outlined in Section 2.2.3.

The dominant frequency bands in power spectral density (PSD) distributions vary through the interaction. Energies inherent to incoming boundary layer turbulent fluctuations are concentrated at 40 kHz and higher, while the major contribution to the RMS in the intermittent region comes from fluctuations around 5 kHz. Once the flow does separate, dominant fluctuations lie between 10-20 kHz.

Separation shock motion drives the shift to lower fluctuation frequencies within the intermittent region. The shock displays both a lower frequency, large scale translating behavior and a higher frequency, small scale *jitter*. The demarcation between these two behaviors is not clearly defined, but the jitter motion is almost certainly due to high frequency turbulent structures (McClure 1992, Brusniak and Dolling 1993, Erengil and Dolling 1993b). Lower frequency shock motion may be due to low frequency near-wall fluctuations in the incoming boundary layer which cause an expansion and contraction of the separated flow downstream of the separation shock (Brusniak and Dolling 1993, Erengil and Dolling 1993b).

The specific motivation behind this study's first objective as stated in Section 1.4 and the corresponding first phase of the test program, Sections 3.4 and 3.5, can be summarized as follows. Schmisser and Dolling (1992) observed that the dominant wall pressure frequencies and the translating separation shock zero crossing frequency, f_c , (defined as the number of unidirectional crossings that the shock makes over a given point in the flow) were around 5 kHz within the intermittent region of a Mach 5 sharp fin interaction. Furthermore, McClure (1992) found that, for the same

boundary layer, the maximum boundary layer/freestream interface crossing frequency, f_i , was about 5.5 kHz, where f_i is the frequency at which the flow transitions between its inviscid freestream characteristics and its viscous, turbulent boundary layer behavior. In a similar Mach 5 sharp fin interaction generated using a thinner boundary layer, Gibson and Dolling (1991) found that frequencies generated by an apparent *shuddering* separation shock motion were concentrated near 8-10 kHz. Thus the question arose as to whether the separation shock frequencies might correlate with the boundary layer interface crossing frequency. By applying the same measurement and analysis techniques to the thinner boundary layer, it was hoped that a clearer understanding of the relationship between f_i , f_c , and intermittent region wall pressure fluctuations could be gained. This was the first objective of the current study.

1.3.2 The Blunt Fin Interaction

Introduced previously, Figure 1-1 shows the large scale, three dimensional blunt fin-induced interaction flowfield characteristics. The shock foot translates aperiodically between U, the upstream influence line, and S, the flow separation line. A supersonic jet extends downstream from the triple point, impacting on the fin leading edge. This is shown in greater detail in the upper center of Figure 1-1. A comprehensive description of the flowfield dynamics is provided by Brusniak and Dolling (1993).

Wall pressure measurements on the centerline show high-amplitude pressure fluctuations characteristic of an aperiodically-translating separation shock and vortical separated flow (Dolling and Bogdonoff 1982, Brusniak and Dolling 1993, Kleifges

1993). Within the intermittent region, mean pressures increase towards the separation plateau level, while RMS pressure levels reach a peak and then decrease. At Mach 5, PSDs show fluctuation frequencies associated with the separation shock motion concentrated near 2 kHz (Dolling 1993a). Within the separated region, both the mean and RMS distributions rise steeply at the fin root to maximum levels. The RMS pressure levels are a function of M_∞ .

To some extent, the aperiodic shock motion is indirectly caused by corresponding pressure fluctuations in the incoming turbulent boundary layer. While strong correlations have been seen between the high frequency turbulent boundary layer wall pressure fluctuations and the separation shock dynamics, the relationship between low frequency boundary layer pressure fluctuations and the shock motion is not as clear (Dolling 1993b). The second objective of the current study was to investigate the latter more thoroughly, using in part the following methodology.

As the separation shock translates in the streamwise direction, the triple point at the base of the inviscid bow shock shifts vertically, since the separation shock remains at a constant angle with respect to the wall (Brusniak 1993). Presumably, the supersonic jet extending from the triple point to the leading edge also translates vertically. Since the jet impact on the leading edge creates large amplitude instantaneous surface pressure fluctuations up to five times the mean surface pressure, \bar{P}_{LE} , stronger correlations might be detectable between movements of the separation shock and the leading edge surface pressures, compared to correlations between separation shock dynamics and incoming turbulent boundary layer pitot pressure fluctuations.

1.4 Summary of Objectives

The purpose of this study is to add to the current understanding of the effects of turbulent boundary layer pressure fluctuations on unsteady swept shock interaction dynamics. Specifically, the study goals are:

- (i) Determine if sharp fin interaction separation shock frequencies correlate with the incoming turbulent boundary layer/freestream interface frequency.
- (ii) Determine how blunt fin interaction dynamics, including separation shock motion and leading edge pressure fluctuations, correlate with the near-wall pressure fluctuations found in the incoming boundary layer.

To address Objective (i), fluctuating pitot measurements were made in a boundary layer generated on a flat plate under conditions identical to those of Gibson's sharp fin interaction. For Objective (ii), an experimental setup was first developed which generated a blunt fin-induced interaction. Pressure fluctuations were then simultaneously sampled from the upstream turbulent boundary layer, the intermittent region, and the fin leading edge. Care was taken to assess the effects of interference between the wall and the pitot probes used in the two experimental phases. An investigation was also made to quantify the interference between the upstream pitot probe and the blunt fin interaction dynamics.

CHAPTER 2

LITERATURE REVIEW

2.1 Introduction

Separated flows generated by interactions between shock waves and boundary layers have been actively researched for more than four decades due to their impact on a wide range of internal and external aerodynamic flows. Since most flows of practical interest are turbulent in nature and therefore lack simple analytical solutions, the majority of experimental efforts have focused on turbulent interactions. However, the complexity of the turbulent interaction, combined with lack of high speed data acquisition systems (DAS), limited early studies to the measurement of time-averaged flowfield properties. In the 1970s, CFD modeling first began to supplement the existing experimental data base of steady, mean flowfield characteristics.

Since the early 1980s, advances in computational and experimental technologies, including the development of miniature, high frequency-response transducers and DAS capable of sampling on the order of millions of data points per second, have allowed the routine measurement of fluctuating pressures, temperatures, velocities, and other quantities. New turbulence models and improved computer algorithms and equipment lend promise to eventual CFD models for unsteady turbulent flows. New experimental data on the unsteady behavior and underlying physics of the shock wave turbulent boundary layer interaction will be needed to help develop and eventually verify these models.

This study is concerned with the shock dynamics near separation in swept shock wave turbulent boundary layer interactions, and the role of incoming boundary

layer fluctuations in their behavior. To facilitate the presentation of experimental results in Chapter 5, this chapter provides a more detailed discussion of sharp and blunt fin interaction flowfield structures and nomenclature than in Chapter 1. Existing evidence for the relationship between upstream fluctuations and the aperiodic separation shock motion are also introduced since this study builds on these previous results.

Extensive reviews of past experimental efforts to define both the mean and fluctuating flowfield and surface properties associated with swept interactions have been compiled by Settles and Dolling (1986, 1990) and most recently Dolling (1993a). The reader is referred to them for a broader discussion of the topic, outside the scope of this work.

2.2 Sharp Fin Interaction Mean Characteristics

2.2.1 Quasi-Conical Symmetry

One of the most salient features of the sharp fin interaction is its quasi-conical symmetry. The traces of the inviscid shock and the surface flow features described in Chapter 1 lie along rays emanating from a common vertex, known as the virtual conical origin (VCO). The VCO is located some distance from the fin apex since the symmetry properties break down near the fin leading edge, in the *inception region*, due to the length scale imposed on the interaction by δ_0 . The inception region is located between the fin root line and a line that curves from the fin leading edge to asymptotically meet the inviscid shock at β_0 .

Quasi-conical symmetry allows the three-dimensional flowfield properties generated by the sharp fin interaction to be plotted in terms of the two conical coordinates, β and ϕ , since the radial coordinate r is "degenerate in truly conical flow" (Settles and Dolling 1990). Therefore measurements along circular arcs within the quasi-conical region at different radial distances r from the VCO can be collapsed. For example, Figure 2-1(a) shows mean surface pressures measured by Zubin and Ostapenko (1979) which collapse in this manner. In practice, the circular arcs can be replaced with lines tangent to the arcs and normal to β_0 , for small β . Figure 2-1(b) shows the collapse of density gradient data from Planar Laser Scattering (PLS) images measured by Alvi and Settles (1990, 1991) throughout the separated region of a sharp fin interaction at different radial distances from the VCO. The physical significance of this data is described in Section 2.2.3.

2.2.2 Wall Mean and RMS Pressure Distributions

Although the unsteady aspects of the sharp fin interaction are of interest in the present study, mean and RMS pressure distribution characteristics will be reviewed here and in the following section in the context of associated flowfield structures.

Figure 2-2, from Tran (1987), shows the characteristic mean pressure (\bar{P}_w) distribution and the effect of interaction strength on \bar{P}_w for a Mach 3 sharp fin interaction. The data were measured along a single line parallel to the freestream flow. \bar{P}_w distributions are typically normalized by the freestream mean wall pressure, $\bar{P}_{w\infty}$. Across the intermittent region, the mean static pressure level rises to a plateau of $1.5 \bar{P}_{w\infty}$ or more before increasing sharply near the fin root to $2 \bar{P}_{w\infty}$ or

higher. As M_n increases with the fin angle of attack, α , at constant M_∞ , plateau pressure values rise and the final mean pressure level increases.

Tran's RMS pressure (σ_{p_w}) distributions are shown in Figure 2-3. The RMS pressure distribution indicates the dispersion of the data from the mean value, so large values of σ_{p_w} identify areas of higher loading levels. RMS pressure levels, normalized by the local mean wall pressure, \bar{P}_w , grow from freestream levels of approximately $0.015 \bar{P}_w$ to a peak (or plateau for weak interactions) of $0.25-0.08 \bar{P}_w$ near the upstream influence, then decrease to a nearly constant $0.025-0.045 \bar{P}_w$ across the separated region. Ahead of β_0 , RMS levels rise slightly before decreasing to approximately $0.015 \bar{P}_w$ near the fin root.

Plotting these normalized distributions in terms of the conical coordinate β demonstrates the two-dimensional quasi-conical nature of this three-dimensional interaction. Figure 2-4(a,b) shows this result quite clearly for a Mach 5 flow (Schmisser 1992) as well as illustrating the higher mean and RMS peak pressures created by this stronger interaction.

Figure 2-5 (Lu 1993) demonstrates inception region effects on the pressure distribution as well as its conical nature. Noting that s is comparable to r , the two data sets nearest to the VCO fall below the collapsed distribution across the plateau region since they are within the inception region, where the interaction is not fully developed. In this case, $M_\infty = 3.44$, $\alpha = 14^\circ$.

2.2.3 Flowfield Structure

The physical flow phenomenon responsible for the characteristic mean and RMS pressure distributions described above are shown in Figure 2-6. Alvi and

Settles (1990, 1991) utilized both white light conical shadowgraphy and conical Planar Laser Scattering to formulate a comprehensive model of the interaction cross section taken normal to the inviscid shock. Interaction strengths ranged from $M_n = 1.22$ to 2.45. Figure 2-7 presents mean and RMS pressure distributions measured recently by Garg and Settles (1993) at Mach 3.95 allowing the correlation of interaction structures shown in Figure 2-6(c) with the distribution behavior. The salient features of the model depicted in these figures are described below.

- 1) For M_n greater than 1.22, the shock foot bifurcates into the characteristic λ -foot and flow separation appears underneath the shock foot. In their interpretation of the shadowgram, a free shear layer lifts off of the surface at the base of the separation shock, passes through and is turned downwards by the rear shock, impinging on the wall at the fin root.
- 2) Flow separation is first indicated by a rise in the mean pressure level. The peak in RMS pressure just downstream of separation in Figure 2-7 is apparently caused by the fluctuating separation shock motion.
- 3) Underneath the λ -foot, the separated shear layer surrounds a flattened, presumably helical vortex. The vortical motion is thought to be responsible for the *dip* seen between the plateau region and the final sharp rise in the mean distribution (Knight et al. 1987).
- 4) A second peak in the RMS distribution occurs near the mean level dip. It may indicate the vortex core location. It seems to move from downstream to upstream

of the inviscid shock location, β_0 , with increasing interaction strength (Dolling 1993a).

- 5) The jet impingement is probably the cause of peak pressure and heating rates found near the fin root. It generates loading levels of 160 dB or more (Dolling 1993a).
- 6) A slipline forms at the triple point and extends rearward along the top of the jet towards the floor.
- 7) With increasing shock strength the jet may increase from subsonic to supersonic velocities. This is indicated by *shocklets*, or small oblique shocks, within the jet which coalesce into a normal shock at high M_n .
- 8) A shocklet is observed in the reversed vortical flow for the highest shock strength tested, $M_n = 2.45$, indicating a local supersonic flow within the separated region.
- 9) For moderate interaction strengths, conical shadowgrams indicate possible secondary separation in the form of a bulge in the reversed flow of the separation bubble. This phenomenon is rarely seen at moderate interaction strengths and disappears altogether as the strength increases.
- 10) β_0 decreases as interaction strength increases. Thus the distance from the base of the inviscid shock to the intermittent region increases, while the jet is compressed

into a narrowing space between the inviscid shock and the fin face. This accounts for the more gradual rise in initial mean pressures and more extreme increase in final pressure levels found in stronger interactions.

This model offers excellent agreement with other time-averaged experimental results, such as the Mach 8.2, $\alpha = 15^\circ$ sharp fin interaction flowfield mean pressure contours shown in Figure 2-8, from Kussoy and Horstman (1993). However, this model provides few details of the unsteady behavior of the separation shock and the resulting separated flow and fluctuating pressure loads. These characteristics are discussed in Section 2.4.

2.2.4 CFD Results

The sharp fin-induced interaction was the first swept interaction to be solved computationally (Settles and Dolling 1990). While a comprehensive summary of the application of CFD modeling is beyond the scope of this experimental study, results from a calculation by Zang and Knight (1989) using a Baldwin-Lomax turbulence model simulating a sharp fin at Mach 3, $\alpha = 17.5^\circ$, are shown in Figure 2-9 for comparative purposes. \bar{P}_w is modeled reasonably well and flowfield structures can also be generally reproduced. Other critical aspects of the flow such as the skin friction coefficient, C_f , and heat transfer rate, q_w , are modeled less successfully. This is especially true for stronger, thus more critical, interactions.

2.3 Blunt Fin Interaction Mean Characteristics

This study is concerned with interaction characteristics along the fin centerline only. For spanwise interaction characteristics, the reader is referred to Dolling and Bogdonoff (1981), Aso et al. (1991), and Gonzalez and Dolling (1993).

Using a semi-infinite fin simplifies the analysis by reducing the number of variables affecting the interaction flowfield scales. Blunt fin-induced interactions in supersonic flows can be considered semi-infinite when h/D , the ratio of the fin height to its diameter (thickness), is greater than about 2.4. (Dolling and Bogdonoff 1982).

2.3.1 Wall Mean and RMS Pressure Distributions

Figure 2-10(a) presents the mean pressure distribution on centerline upstream of the leading edge in Mach 3 and Mach 5 interactions. The figure demonstrates that streamwise interaction length scales are on the order of D and are only weak functions of the incoming boundary layer thickness, δ_0 , and freestream Mach number, M_∞ . The distribution is qualitatively similar to that of the sharp fin interaction. An initial increase in the mean pressure to a plateau region is followed by a sharp rise near the fin root. The same distribution is seen in 2-10(b) for a Mach 2.95 flow, along with the results of a CFD calculation made by Hung and Buning (1985). The RMS distribution is also similar to that generated by the sharp fin interaction. An example is shown at the top of Figure 2-19. An important exception is the extremely high RMS generated at the fin root.

2.3.2 Leading Edge Pressures

Mean pressure measurements along the blunt fin leading edge also yield a characteristic distribution; however, their details depend on δ_0 . Figure 2-11(a-c) shows data from Dolling and Bogdonoff (1982) and others. In Figure 2-11(a), the vertical axis is the height above the wall, non-dimensionalized by the fin thickness, while the horizontal axis presents fin leading edge surface pressures, non-dimensionalized by the freestream pitot pressure, P_{t2} . The pressure distribution rises from low values at the fin root to a local maximum, then decreases to the pitot level. The local maximum is due to the impact of a fluid jet described below.

The boundary layer thickness, if large enough, may determine where the local maximum occurs. At Mach 3, it was found that if D/δ_0 is greater than about 3.8, "the shock wave structure and the jet are predominately outside the boundary layer," and data collapse as shown in Figure 2-11(b) (Dolling and Bogdonoff 1982). If D/δ_0 is small, on the order of 1 or less, the interaction features are partially or completely "submerged" in the incoming boundary layer, affecting the position and magnitude of the local maximum pressure as shown in Figure 2-11(a). The authors have shown that the correct non-dimensional pressure is $P_{t2}(Z)$, the local boundary layer pitot pressure. See Figure 2-11(c). For the current study, $D/\delta_0 \approx 1.05$.

2.3.3 Flowfield Structure

The blunt fin interaction centerline pressure distributions described above are caused by the flowfield structure pictured in simplified form in Figure 1-1. The incoming flow separates due to the pressure rise caused by the inviscid shock, creating the inviscid shock bifurcation. The upstream separation shock extends

forward from the triple point towards U while the separated flow detaches in the vicinity of S and rolls up into one or more vortices. The vortices are then turned by the flow and swept downstream. As in the sharp fin interaction, the blunt fin interaction characteristic wall pressure profile plateau and dip is the result of this vortical, separated vortices.

The separation shock/bow shock interaction creates a supersonic jet surrounded by locally subsonic flow. Classified by Edney (1968) as a Type IV interaction, the jet extends rearward from the triple point, impacting on the fin leading edge. This accounts for the peak pressures in the leading edge distribution (Figure 2-11(a-c)). The jet impact forces some of its fluid into the separated region below, possibly affecting the shock dynamics through recirculation of turbulent structures. This is described in greater detail in Section 2.4.2.

2.3.4 CFD Results

An in-depth discussion of the current merits and weaknesses of CFD results is beyond the scope of this study. Instead, representative examples of recent work are provided in comparison with experimental results. Returning to Figure 2-10(b), the computationally-generated data of Hung and Buning (1985) matches the mean wall pressure distribution quite well. Especially important is the accurate reproduction of the location and magnitudes of local pressure maxima. Figure 2-12(a) shows both experimental and computational data for a blunt fin leading edge mean pressure distribution (note the horizontal axis values are now increasing, accounting for the mirror image between Figure 2.12(a) and 2.11(a-c)). The under-prediction of the local peak in pressure is of concern, yet the overall agreement in the distribution shape

is encouraging. Similar results have been recently published by Lakshamanan and Tiwari (1993) for fins with swept leading edges.

CFD has also been used to compute the vortical flow structure. For example, Figure 2-12(b) shows particle paths on centerline. The large horseshoe vortex is clearly demarcated; a tiny root vortex thought to be responsible for the extreme RMS levels measured there is predicted as well. A correlation between the local maximum in the leading edge pressure distribution and the flow impact point is apparent. Lakshamanan and Tiwari (1993) show how the vortex scale and strength are affected by leading edge sweepback.

2.4 Interaction Unsteadiness

While the above discussion of surface pressures and characteristic flowfield structures in three-dimensional shock wave turbulent boundary interactions is of practical use to designers and engineers, it does not provide any information on the unsteady shock behavior or instantaneous peak loads generated beneath jets or shocks. Both interaction types of interest here are in fact unsteady. CFD currently has *no* capability to model interaction unsteadiness, and most of the experimental studies of fluctuating loads in three-dimensional flows have been carried out only within the last seven years (Dolling 1993a). The following sections will introduce the nomenclature and characteristics of unsteady swept interaction behavior recognized to date through experimental work. The driving mechanisms behind the unsteadiness are also briefly discussed.

2.4.1 Characteristics

To better understand the results of the initial sharp fin study of Tran et al. (1985) and Tran (1987) at Mach 3 and the more recent studies of Gibson (1991) and Schmisser (1992) at Mach 5, it is useful to examine them in conjunction with observations of interaction unsteadiness made in two-dimensional shock wave turbulent boundary layer interactions generated by unswept compression ramps (Erengil 1989, 1991, 1993a; Gramann and Dolling 1990; McClure 1992). For example, Figure 2-13(a-h) shows instantaneous wall pressure signals measured beneath the intermittent region of a Mach 5, 28° compression ramp interaction (McClure 1992). Similar signals are presented in conjunction with Figures 2-14(a-c) and 2-16(a-f) for blunt and sharp fin-induced interactions, respectively. The data are characterized by a low-frequency, high-amplitude pressure signal caused by the separation shock motion superimposed on top of high-frequency, low-amplitude pressure fluctuations inherent to the turbulent boundary layer. Conditionally sampled ensemble averages from data such as these allows the shock dynamics, including position histories, velocity histories, and sweeps and turnarounds, to be quantified as described in Chapter 4. Furthermore, upstream and downstream influences on the interaction can be identified as discussed in the following section.

Along with the RMS peak near the upstream influence identified in the RMS pressure distributions, the amplitude probability density distributions (PDDs) of the wall pressure signals have characteristic shapes within the region of separation shock motion. Figure 2-14(a-e) displays PDDs and accompanying pressure signals measured along the centerline in a Mach 3 blunt fin interaction (Dolling and Bogdonoff 1981). The PDDs become positively skewed at positions of low

intermittency. This occurs because the most probable value of the signal, the undisturbed boundary layer pressure, is lower than the mean. As γ increases, the PDDs become bimodal in nature due to a second distinct, higher pressure generated by the separated flow. This behavior is shown in Figure 2-13(c) weakly. An additional example is Figure 2-15, which displays the highly bimodal dimensional PDDs associated with the data of Figure 2-13(a-h).

Figure 2-16(a-f) presents PDDs, raw data, and power spectral density functions (PSDs) from a Mach 5 sharp fin interaction. PSDs indicate the spectral distribution of energies associated with fluctuations in the flow. In Figure 2-16(a), the incoming boundary layer spectral contributions display a maxima near 40 kHz. Although this may also be associated with the roll-off of a 50 kHz filter, it does correspond well with the large eddy frequency ($U_\infty/\delta_0 \approx 40$ kHz) of the incoming boundary layer. The principal frequency components shift to about 5 kHz through the intermittent region, Figure 2-16(b-d), and finally increase to a broadband spectra with maximum contributions around 25 kHz in the separated region, shown in Figure 2-16(f). In swept compression ramp interactions, a similar behavior is observed. Figure 2-17 displays PSDs from Erengil and Dolling (1992) at Mach 5, illustrating the asymptotic nature of the spectral energy to approximately 6 kHz with increasing interaction sweep.

Gibson (1990) made fluctuating wall pressure measurements in sharp fin interactions of identical strengths as Schmisser (1992) but in a thinner boundary layer. PSDs are shown in Figure 2-18. Freestream spectral contributions drop off sharply at 50 kHz due to filtering. The large eddy frequency for this relatively thin boundary layer is on the order of 120 kHz. Gibson concluded that the interaction was

characterized by a compression region which exhibited a shuddering motion, instead of the aforementioned intermittent characteristics. Within this compression region, the greatest fraction of fluctuating energies are located from 8-10 kHz, increasing to a broadband level near 50 kHz in the separated flow. The fact that Gibson's intermittent region spectral maxima are 70-100% higher for interactions of identical strengths generated in the same test facility by Schmisser (1992) is a primary motivation for Phase 1 of the current study.

PSDs from Gibson's work displayed no shift in peak frequencies for "any three spanwise stations positioned along a conical ray in the entire interaction region and for all shock strengths tested" and so strongly support the thought that quasi-conical symmetry is an appropriate tool for the non-dimensional collapse of data (Gibson and Dolling 1991). Recently, independent assessments of Gibson's work indicates his qualitative shuddering compression model may be the result of insufficient spatial resolution (Schmisser and Dolling 1992, Garg and Settles 1993). However, the frequency data are still intriguing, since they may indicate a dependence of the swept interaction dynamics on incoming boundary layer characteristics.

An example of blunt fin-induced interaction spectral characteristics is provided in Figure 2-19 for a Mach 5 interaction. The interaction RMS distribution is included for comparison. Although the data are measured in a cylinder-induced interaction, Brusniak (1991) has shown that the cylinder wake does not alter interaction centerline properties. The intermittent region spectra are dominated by the relatively low-frequency aperiodic shock motion centered around 2 kHz, while the separated region at the fin root, an area of extremely high σ_{pw} , shows a large fraction of the fluctuating energy is near 25 kHz.

The spectral maxima in the blunt fin interaction intermittent region are approximately equal to the shock zero crossing frequency, f_C , which indicates the number of unidirectional shock crossings over a given position. This relationship has been shown for unswept compression ramp and sharp fin-induced interactions as well (McClure 1992, Schmisser 1992). Apparently, f_C is mainly an indication of the low frequency streamwise translation of the separation shock, upon which is imposed a high frequency jitter. It is probable that the experimental resolution, which is dictated by the transducer size and minimum spacing, ζ , for the Mach 5 interactions described above is not sufficient to observe the complete high frequency shock dynamics (Kleifges 1993).

2.4.2 Driving Mechanisms

By correlating pressure signals with the separation shock dynamics, the flow physics responsible for instantaneous separation shock foot position and velocity histories can be investigated. Currently, two different phenomena are thought to directly affect the interaction dynamics. The first is the passage and entrainment of turbulent structures from the incoming boundary layer into the interaction flowfield. The second is a recirculating process by which the turbulent fluctuations and other flowfield events may perturb the interaction from the downstream direction.

Andreopoulos and Muck (1987) analyzed Mach 3 compression ramp fluctuating wall pressure signals and concluded that "the turbulence of the incoming boundary layer is largely responsible for the shock motion." This was based on similarity between the incoming flow bursting frequency and the mean separation shock period ($1/f_C$). They also found that measured shock speeds were similar to

fluctuating velocities in the incoming boundary layer. However, their data analysis was based on a single threshold method which rendered it susceptible to false event detection (Dolling 1993a). Tran (1987) subsequently performed experiments in the same facilities and concluded that there was *no correlation* between the upstream turbulent fluctuations and the intermittent pressure pulses.

Earlier parametric experimental studies performed with blunt fins in which D was held constant and δ_0 was varied, or vice versa (Dolling and Smith 1989), suggest that both the upstream and downstream flow can contribute to the interaction dynamics. In general, increasing the fin thickness with a constant boundary layer thickness or decreasing δ_0 while holding D constant increased the frequency of the shock-induced pressure fluctuations.

From ensemble-averaged pressure histories created by applying conditional sampling techniques to simultaneously sampled wall pressure measurements, Erengil and Dolling (1991,1992) suggest that pressure pulses apparently propagate upstream into the intermittent region just prior to turn-arounds in the shock direction. Expanding on these conditional sampling algorithms, McClure (1992) became "the first to show a direct correlation between pressure fluctuations in the incoming flow and separation shock motion" (Dolling 1993a). Figure 2-20(a,b) shows ensemble-averaged wall pressure signals corresponding to an upstream or downstream shock sweep. The portion of the signal labeled 'sig' in each plot indicates that a pressure rise-fall-rise correlates with downstream motions, while a pressure fall-rise-fall is associated with the upstream sweeps. The signals remain coherent as they traverse the shock (McClure 1992), lending credence to the thought that they recirculate and effect separation shock dynamics from the downstream side.

Erengil and Dolling (1993b) identify the instantaneous static pressure ratio across the shock, P_1/P_2 , as the immediate cause of the high frequency shock motion in swept and unswept compression ramps and swept blunt fins. Fluctuations in the ratio result from the propagation of turbulent structures from either the upstream boundary layer or the downstream separated flow. Figure 2-21 depicts a qualitative model of the recirculation zone offered by Kleifges (1993) to describe the results of cross-correlations between pairs of transducers in the separated region. It provides at least a gross idea of how turbulent fluctuations might impact the shock dynamics repeatedly. In contrast, low frequency shock foot motions are apparently driven by the expansion and contraction of the separated flow *bubble*. The bubble dynamics may in turn be caused by incoming turbulent structures or the separated shear layer characteristics. Experimental projects such as the current study which involve simultaneous sampling upstream flow characteristics, separation shock dynamics, and separated flow behavior should improve our understanding of these phenomena.

2.5 Summary

From the preceding review of shock wave turbulent boundary layer interaction characteristics, several points should be emphasized due to their importance and impact on this study's objectives and experimental program.

- 1) Both sharp and blunt fin interactions exhibit unsteady, high amplitude wall pressure fluctuations from the upstream influence to the fin root. Mean and RMS wall pressures throughout the interaction increase to several times their freestream values or more. The most extreme loads are located near the fin root. The

intermittent region also experiences a substantial peak in RMS pressure and an increase in mean pressure due to the aperiodic separation shock motion.

- 2) The frequencies associated with the fluctuating separation shock motion are evident from wall pressure PSDs. In sharp fin interactions, Schmisser's (1992) and McClure's (1992) results suggest that separation shock fluctuation frequencies may correlate with the incoming turbulent boundary layer/freestream interface crossing frequency band. Investigating this possible correlation is the first objective of this study.

- 3) McClure (1992) has shown that incoming boundary layer turbulent fluctuations correlate with separation shock sweeps. Furthermore, there is evidence that a low-frequency fluctuation in the boundary layer is responsible for low-frequency separation shock dynamics (Brusniak and Dolling 1993, Erenkil and Dolling 1993b). The second goal of this study is to build on these previous investigations. Unlike past experiments, the current study will use leading edge fluctuating surface pressures as well as upstream turbulent boundary layer fluctuating pitot pressures to generate correlations with the intermittent region shock-induced fluctuating wall pressures and separation-shock dynamics.

CHAPTER 3

EXPERIMENTAL PROGRAM

3.1 Introduction

Two separate experimental phases were needed to meet the research objectives of Section 1.4. Phase 1 consisted of fluctuating pitot measurements made in a flat plate turbulent boundary layer, including complete surveys and point measurements within the boundary layer/freestream interface region. The Phase 1 test setup and experimental procedures are described in Sections 3.4 and 3.5. Phase 2, described in Sections 3.6 and 3.7, included simultaneously sampled instantaneous wall pressures in the upstream boundary layer, at the leading edge of a blunt fin, and across the intermittent region of the blunt fin-induced interaction. Sections 3.2 and 3.3 provide descriptions of the wind tunnel facility and instrumentation systems respectively, which were common to both phases.

3.2 Wind Tunnel Facility

All experiments were performed at the Balcones Research Center Mach 5 blow-down wind tunnel facility operated by the Center for Aeromechanics Research at the University of Texas at Austin. Air is provided by a four-stage Worthington HB4 compressor and stored at 2550 psig in external tanks. During wind tunnel operation, flow passes through a valve which regulates the tunnel stagnation pressure, over two banks of 420 kW nichrome wire heaters that control the tunnel stagnation temperature, and into the stilling chamber. Air then expands from the chamber through a fixed-geometry nozzle to a Mach number of 4.95 in the 6-in.-

wide, 7-in.-high test section, 36 in. downstream of the nozzle throat. A straight duct normal-shock diffuser provides exhaust to the atmosphere. The stilling chamber stagnation temperature and pressure are constantly monitored throughout a tunnel run, which can last up to 60 seconds. Flow conditions are allowed to stabilize at the nominal values required for each experimental phase before data acquisition begins; however, stagnation conditions vary up to $\pm 2\%$ during a tunnel run.

3.3 Instrumentation

Both experimental phases utilized Kulite pressure transducers to measure fluctuating pressures at the tunnel wall or fluctuating pitot pressures within the boundary layer, or at the hemi-cylindrical blunt fin leading edge. Transducer specifications as quoted from Kulite Corporation catalogs are listed in Table 3-1, on the following page. Individual transducers are inserted into hollowed-out #440 brass machine screws which allow them to be mounted flush with the surface of the instrument plug or the fin leading edge.

Transducer output signals were amplified by either Dynamics Model 7525, EG & G PARC Model 113, or Measurements Group Model 2311 amplifiers and low-pass filtered by either Ithaco Model 4113 or Model 4213 electronic filters. Each amplifier's zero output and gain were set to maximize transducer response based on the expected pressure range.

Table 3-1: Kulite Transducer Specifications

Model Numbers	XCQ-062-50A, XCQ-062-15A
Pressure/Overpressure (psia)	15/45, 50/150
Outside Diameter (in.)	0.064
Sensing Mechanism	Fully active 4-arm Wheatstone bridge diffused into a 0.028 in. diameter silicon diaphragm
Frequency Response (kHz) (limited by protective cover over diaphragm)	50
Electrical Excitation (V DC)	5
Full Scale Output (mV)	100
Operating Range, Nominal/Compensated (°F)	-65 to 250/80 to 180
Thermal Zero Shift (% per 100°F)	± 2
Residual Unbalance (% FSO per 100°F)	± 0.5
Combined Nonlinearity and Hysteresis (% FSO, best fit straight line)	0.5
Repeatability (% FSO)	0.1

A computer-based data acquisition system (DAS) allowed high frequency, multiple-segment sampling and data storage. Conditioned transducer signals were digitized by two LeCroy 6810 12 bit A/D converters and transferred to a Hewlett Packard HP 9000 workstation. Up to 8 channels could be simultaneously sampled at a frequency of 500 KHz/channel. 512 records/channel (1024 data points per record) were recorded. Data could then analyzed on the HP workstation and stored on magnetic tape by a Hewlett Packard HP 7979 tape drive.

Specific calibration procedures, sampling frequencies, and filter settings are summarized in each phases' Experimental Procedure section (Sections 3.5 and 3.7).

3.4 Phase 1: Turbulent Boundary Layer Study Test Setup

An overall view of the arrangement for making fluctuating pitot pressure measurements in the flat plate boundary layer is shown in Figure 3-1. Individual components are described in detail below.

The test section used in this phase is 12 in. long with a 6 in. by 7 in. cross section and two removable side doors (5.75 in. by 6.75 in.). A slot machined in the ceiling allows pitot probe placement and movement. This test section also has tapped holes in the sidewalls to accommodate the flat plate and its dowel anchor pins.

The flat plate has been used previously to generate turbulent boundary layers and support sharp fin models (Gibson 1990). Machined from brass, it is 29.9 in. long, 6 in. wide, and 0.75 in. thick, and has a sharp leading edge tapered at 16.7°. As shown in Figure 3-1, it is mounted horizontally 2.25 in. above the tunnel floor and is held parallel to the flow by dowel pins in the tunnel walls.

Two different pitot-type probes were used, as shown in Figure 3-2. The conventional probe, Figure 3-2(a), had a rectangular tip opening measuring 0.008 in. high and 0.08 in. wide. There was about 25 in. of 0.085 in. diameter tubing between the tip and a Kulite transducer. Thus the frequency response was limited to a few hundred Hz at most. The Kulite-tipped probe, Figure 3-2(b), with a transducer mounted at the tip facing upstream, increases frequency response to about 50 kHz. However, the spatial resolution decreases due to the larger 0.064 in. outside diameter of the probe tip.

The probe drive shown Figure 3-1 was used to hold the pitot probes in place. The probe support shaft is clamped to a chassis which translates vertically on a threaded shaft. One full turn of the crank handle moves the probe 0.01 in. up or down. The exact probe height can be measured visually in increments of 0.001 in. from an SPI dial gauge mounted on the assembly, or electronically by recording the voltage output from a Schaevitz Engineering Model 3000 HPD linear variable displacement transducer (LVDT) mounted on the probe drive.

3.5 Phase 1: Experimental Procedures

3.5.1 Freestream Flow Conditions

Phase 1 freestream flow conditions, Table 3-2, were controlled to closely match those used in previous sharp fin-induced shock wave/turbulent boundary layer interactions carried out in the same test section on the flat plate described above (Gibson 1990). This ensured that the boundary layer generated in the current study was the same as that which existed in the previous experiments.

Table 3-2: Phase 1 Freestream Flow Conditions

P_0 (psia)	325 ± 5
T_0 ($^{\circ}\text{R}$)	673 ± 3
M_{∞}	4.95
U_{∞} (ft/sec)	2590
Re_{∞} (1/ft)	1.36×10^7

3.5.2 Undisturbed Boundary Layer Survey

To determine the turbulent boundary layer mean flow properties, a survey was made using the conventional pitot probe, shown in Figure 3-2(a), and the probe drive assembly, Figure 3-3. The survey was made on the plate centerline 19 in. downstream of the plate leading edge, repeating the conditions of Gibson (1990).

The pitot probe transducer was calibrated daily from 0.2 to 30 psia (0 to 4.096 V unipolar mode on the LeCroy DAS) using an external vacuum pump and 500 psig helium tank. The LVDT was calibrated from 0 to 0.5 in. (0 to 2.048 V unipolar). The exact zero probe height was found by using ohmmeter leads grounded against the probe shaft and the tunnel wall. Since the probe shaft is insulated from the probe drive, the meter shows a finite resistance when the probe just touches the plate. Once the LVDT output voltage corresponding to this zero was recorded, the probe was moved in 0.05 in. increments as shown on the dial gauge, with the corresponding LVDT voltage recorded at each point. The conditioned signal from the conventional pitot probe transducer occupied one channel on the DAS while the LVDT was sampled directly on a second channel. The sampling frequency was 100 Hz, conservatively low-pass filtered at 25 Hz to avoid aliasing. Four records, 1024 data points each, were recorded.

To avoid probe damage, the tunnel was started with the probe positioned 0.2 in. above the plate surface. Once stagnation conditions had stabilized, the probe was moved downwards until contact with the tunnel floor was established. The LVDT signal at this point indicated the probe deflection due to the oncoming flow. The probe was then slowly moved back up to a height of 0.5 in. The tunnel ran for approximately 40 seconds.

3.5.2.1 Mean Boundary Layer Properties.

Analysis by the program LEAST (Section 4.2) provided the mean boundary layer properties given in Table 3-3. Other results of this initial survey are summarized in Section 5.2.1.

Table 3-3: Flat Plate Mean Boundary Layer Properties

δ_0 (in.)	0.204	Re_θ	9.69×10^3
δ_1 (in.)	0.238	H	12.01
δ^* (in.)	0.101	Π	0.47
θ (in.)	0.0084	C_f	9.48×10^{-4}

3.5.3 Boundary Layer/Freestream Interface Characteristics.

The Kulite-tipped probe shown in Figure 3-2(b) was used to measure pitot pressure fluctuations at fixed points across the boundary layer intermittent region to quantify the boundary layer intermittency, γ , and interface crossing frequency, f_i .

Calibration of the pitot probe was accomplished daily as described in Section 3.5.2. Probe height was again measured by both the dial gauge and LVDT. The sampling frequency was 100 kHz, filtered at 25 kHz to avoid aliasing. Eight segments with 128 records per segment and 1024 data points per record, were recorded. Sampling time was just over 1.31 seconds per segment.

To conduct these measurements, the probe was set at the desired initial height, allowing for flow deflection effects. Once the tunnel flow stabilized, a trigger linked to the DAS initiated sampling. After the data segment was recorded at that position, the probe was moved 0.03 in. higher, and the data acquisition system was triggered again to sample the following segment. This procedure was repeated for all eight

segments. Offsetting the initial height by 0.015 in. and completing additional tunnel runs resulted in samples of the entire intermittent region at 0.015-in. intervals. A typical tunnel run was 40 seconds.

3.6 Phase 2: Blunt Fin-Induced Interaction Test Setup

The Phase 2 test setup is shown in Figure 3-3. A 36 in.-long test section was used to accommodate the shock generator, instrument plug, and near-wall pitot probe. Both the floor and ceiling have 0.5 in.-wide slots on centerline for probe or model support. The floor also has a 6 in. wide, 9.5 in. long rectangular plug in which the 3.4 in. diameter instrument plug and fin mounting plates are anchored. The sides of the section are hinged doors allowing easy access. Each door has two 6-inch-diameter plugs to accommodate viewing windows.

The fin model which generates the shock wave/turbulent boundary layer interaction is shown in Figure 3-4. It has two parts: a body and a removable, instrumented leading edge. The stainless steel fin body is 4 in. high, 0.75 in. wide, and 3 in. long. Its downstream hemi-cylindrical end was not used in this study. The upstream end had a 0.25 in.-wide, 3.75 in. long slot machined in it to anchor the instrumented leading edge and provide room for the transducer assemblies and wires. A 0.25 in.-diameter hole were bored horizontally from the front and vertically from the bottom of the fin, allowing passage of transducer wires from the leading edge to the DAS. The 0.75 in.-diameter hemi-cylindrical aluminum leading edge is also 4 in. high. As shown, it has two transducer holes on each end. Due to the position of the holes and the location of the centered anchor tab, turning the leading edge upside-down generates a 0.5ζ resolution for measuring wall pressure fluctuations on the

leading edge from 2ζ to 3.5ζ above the tunnel wall. The 1ζ (0.115 in.) transducer spacing is the minimum machineable separation distance.

The floor-mounted pitot probe shown in Figure 3-5 was used to record instantaneous near-wall pitot pressures. The probe had a minimal effect on the downstream interaction due to the streamlined probe shaft. At the tip of the probe arm, 1.25 in. upstream of the center of the shaft, is a Kulite transducer with an outside diameter of 0.064 in.

The floor probe could not be utilized without several other components. For this study, the brass plug in the tunnel floor centerline slot had a 0.435 in.-diameter hole bored in it to hold the probe. An aluminum probe support bolted to the bottom of the centerline plug held the cylindrical portion of the probe shaft in place, sealing the hole and holding the probe tip at the required height above the tunnel floor.

3.7 Phase 2: Experimental Procedures

3.7.1 Freestream Flow Conditions and Boundary Layer Properties

Freestream flow conditions for Phase 2 are shown in Table 3-4. The mean boundary layer properties at the tunnel wall are given in Table 3-5.

Table 3-4: Phase 2 Freestream Flow Conditions

P_0 (psia)	320 ± 5
T_0 ($^{\circ}\text{R}$)	640 ± 3
M_{∞}	4.95
U_{∞} (ft/sec)	2500
Re_{∞} (1/ft)	1.5×10^7

**Table 3-5: Tunnel Wall Mean Boundary Layer Properties
(McClure 1991)**

δ_0 (in.)	0.59	Re_θ	3.16×10^4
δ_1 (in.)	0.71	H	10.2
δ^* (in.)	0.26	Π	0.78
θ (in.)	0.026	C_f	7.74×10^{-4}

3.7.2 Simultaneous Intermittent Region and Leading Edge Pressure Measurements

Experiments were performed with seven transducers mounted upstream of the blunt fin, on the tunnel centerline, flush with the tunnel wall in a round instrument plug. An eighth transducer was mounted in the fin leading edge. These measurements were used as a baseline, establishing the physical extent of the intermittent region, where pressure fluctuations are affected by the translating separation shock, and recording characteristic fluctuations at the leading edge.

Calibration was carried out with all eight transducers mounted in the plug. The seven wall transducers were calibrated from 0.3 to 5 psia in the 0 to 4.096 V unipolar mode. The eighth transducer was calibrated from 0.3 to 30 psia in the 0 to 10.24 V unipolar mode. The calibration process for the instrument plug uses suction to generate pressures ranging from nearly 0 psia to atmospheric (approximately 14.5 psia), so the gain of the eighth transducer was adjusted at atmospheric pressure to give an output of 10.24 V (the maximum allowable by the DAS) at 30 psia. The transducer was then removed from the wall plug and installed in the fin leading edge just before tunnel operation. The linear calibration curve allows the extrapolation of pressures above the atmospheric value. Transducers were located from 22ζ to 16ζ

(at 1 ζ intervals) upstream of the leading edge. The fin leading edge transducer was moved between runs from 2 ζ to 3.5 ζ (at 0.5 ζ intervals) from the wall. Both the calibration process described above and the procedure of moving transducers after calibration have been used successfully in the past (Brusniak 1993, Erengil 1993). Sampling frequencies of 200 kHz and 500 kHz were used. All signals were filtered at 50 kHz due to the transducers' limited frequency response (Table 3-1). During a tunnel run, sampling was initiated once stagnation conditions stabilized. With 1024 points per record and 512 records sampled, data acquisition lasted either 1.05 or 2.62 seconds.

3.7.3 Probe/Wall Interference Tests

Experiments were performed to determine the height at which the pitot probe would experience interference from its own bow shock reflected from the wall. The Kulite-tipped pitot probe shown in Figure 3-2(b), the probe drive with dial gauge and LVDT, and the ohmmeter circuit described in Section 3.4 were used along with a 6 in.-diameter test section window to visually and electronically measure the vertical and streamwise probe deflection. A single transducer installed in the instrument plug was calibrated from 0.3 to 3 psia and the probe tip was positioned so that it would be centered over the transducer during tunnel operation. Results (see Section 5.1) show that the minimum practical near-wall probe height is about 0.065 in.

3.7.4 Simultaneous Near-Wall Boundary Layer, Intermittent Region, and Leading Edge Pressure Measurements

Tests were carried out as described in Section 3.7.2, except the number of transducers at the wall under the intermittent region was reduced to six. The Kulite-

tipped near-wall probe was installed on the tunnel centerline such that the probe tip was 8.05 in. ($13.6 \delta_0$) upstream of the fin leading edge. It was calibrated from 0.3 to 30 psia using the vacuum pump/helium tank apparatus. The instrument plug and leading edge transducer were calibrated as described above. Data were obtained with the probe set at either 0.2 or 0.3 in.

CHAPTER 4

ANALYSIS TECHNIQUES

4.1 Standard Statistical and Time Series Analysis

The fluctuating surface and pitot pressure signals were analyzed using basic statistical methods, standard time series analysis, and several specialized conditional sampling algorithms. For each signal, statistical values of interest included the mean, standard deviation, skewness coefficient, and flatness coefficient. The amplitude probability density distribution was also calculated. Auto correlations, cross correlations, and power spectral density distributions were obtained from time series analysis methods. The reader is referred to the comprehensive book by Bendat and Piersol (1986) for the derivation of these quantities.

Additional algorithms and conditional sampling methods used are described below.

4.2 LEAST Analysis of Mean Boundary Layer Properties

Two related codes were used to analyze measurements made in the flat plate boundary layer survey. The first, PRELEAST, generates a smooth boundary layer pitot pressure profile from a fluctuating pitot pressure survey. The second code, LEAST, uses the PRELEAST output file and an iterative method developed by Sun and Childs (1973) to generate mean velocity profiles and perform a least squares fit of the velocity data to the law-of-the-wall, law-of-the-wake.

PRELEAST first averages the data over a user-chosen number of data points, or "window", in order to generate a smooth pitot pressure profile. The user inputs

the vertical offset for the LVDT-generated height data which compensates for the combined effects of a slight downward probe deflection due to the tunnel flow and the small fixed distance from the lower surface of the probe tip to its center. The interactive code also requires the user to input single values or profiles of the static pressure, stagnation pressure, and stagnation temperature. The stagnation values are measured in the tunnel stilling chamber and are assumed to represent the test section values as well. PRELEAST assumed adiabatic conditions, creating a constant total temperature profile throughout the boundary layer.

After PRELEAST creates the pressure profile and a tabular data output file from the raw fluctuating pitot pressure data, program LEAST generates velocity profiles using the tabular data. First, it calculates a freestream Mach number, M , from the ratio of the freestream pitot pressure, P_{t2} , to the stagnation pressure, P_0 . Once the freestream static pressure, P_∞ , is found from M and P_0 , the Mach number boundary layer profile, $M(y)$, is calculated using the Rayleigh-Pitot formula. Since $M(y)$ and the constant total temperature, T_0 , define a local speed of sound, $a(y)$, the local velocity profile, $u(y)$, is found from the product $a(y)M(y)$. The code also generates the velocity profile in the boundary layer coordinates, u^+ and y^+ . Only points greater than y^+ of 100 are used in the LEAST algorithm due to interference between the probe bow shock and the wall.

LEAST performs an iterative process to fit the experimental data to the wall-wake profile. Its output summarizes the boundary layer properties including the parameters δ , δ_0 , δ_1 , δ^* , and θ ; wake strength parameter, Π ; unit Reynolds number, Re_∞ ; wall shear stress, τ_w ; skin friction coefficient, C_f ; and shear velocity, u_τ .

Table 3-3 summarizes the flat plate boundary layer parameters of interest, while Section 5.2.1 and Figure 5-2 present results of the PRELEAST/LEAST analysis.

4.3 Two Threshold Method For Separation Shock Statistics

Within the intermittent region, wall pressure signals undergo changes in amplitude caused by either turbulent fluctuations within the boundary layer *or* the passage of the separation shock in the upstream or downstream directions. An algorithm refined by Brusniak (1988) and Dolling and Brusniak (1989) converts the intermittent region signal into digital *boxcar signals*, described below, which are then used to quantify separation shock dynamics and related statistics. The code uses the mean pressure, \bar{P}_w , and the RMS pressure, σ_{p_w} , of the boundary layer component of the signal to define two thresholds:

$$T_1 = \bar{P}_w + 3\sigma_{p_w}, \quad T_2 = \bar{P}_w + 6\sigma_{p_w} \quad (4-1)$$

These thresholds have been shown to produce "physically meaningful" and repeatable calculations of the shock dynamics (Brusniak 1991).

The application of the thresholds to a raw data signal is shown in Figure 4-1. A rise time, t_r , is recorded on a corresponding boxcar signal as a 1 when the instantaneous wall pressure, $P_w(t)$, rises above T_2 . A fall time, t_f , is recorded and the boxcar signal is reset to 0 when $P_w(t)$ falls below T_1 . From these quantities the shock *zero crossing frequency*, f_c , and *intermittency*, γ , equations (4-2) and (4-3), can be calculated for each wall transducer position.

$$f_c = \frac{1}{\frac{1}{N} \sum_{i=1}^{N-1} (t_{r_{i+1}} - t_{r_i})} \quad (4-2)$$

$$\gamma = \frac{\sum_{i=1}^N (t_r - t_f)_i}{t_{\text{total}}} \quad (4-3)$$

where N is the number of shock crossings detected. Physically, f_c measures the number of unidirectional shock crossings at a given position, while γ defines the fraction of time that the shock is upstream of the transducer.

4.4 VITA Conditional Sampling Technique

The variable-interval time-averaging (VITA) technique, first developed by Blackwelder and Kaplan (1976), measures a signal's variance over a short period of time. When the short term variance, σ_{st}^2 , exceeds $K\sigma^2$, where K is a chosen threshold value, *events* are considered as occurring in the signal.

The short term variance of a fluctuating pitot pressure signal, $P(t)$, is defined as:

$$\sigma_{st}^2 = \frac{1}{T_{st}} \int_b^a P(t)^2 dt - \left(\frac{1}{T_{st}} \int_b^a P(t) dt \right)^2 \quad (4-4)$$

$T_{st} \equiv$ VITA averaging period, or "window size", $a = t + T_{st}/2$, and $b = t - T_{st}/2$

Appropriate choices of the window size, T_{st} , and threshold level, K , are critical in identifying values of σ_{st}^2 which represent typical, characteristic events. In the limit of $T_{st} = 0$ (a single point), no short term variance is present. For small values of T_{st} , the short term variance is a positive value and extremely sensitive to changes in the window size. As T_{st} approaches larger values, the short term variance asymptotes to the long-term variance, σ^2 . The best value for T_{st} maximizes the short term

variance, allowing the clearest indication of changes in the slope of the raw data signal caused by an event. McClure (1992) has shown that the optimal window size for a periodic function such as a sine wave with period T is $0.56T$. For a time varying signal with no apparent period such as $P_o(t)$, a parametric study can be performed to find the optimal T_{st} . A parametric analysis can also be used to find the ideal threshold K which identifies those events caused by the intermittent nature of the boundary layer/freestream interface. It should not allow the detection of small fluctuations in the raw data signal caused by noise. For the current boundary layer, a previous study by McClure (1992) has shown that a window size of $40 \mu s$ maximizes T_{st} while a threshold level of $K = 40$ provides the best event detection. When the threshold value $K\sigma_{st}^2$ is exceeded, a boxcar signal directly analogous to that described above is generated. It can then be statistically analyzed and the boundary layer *interface crossing frequency*, f_i , and γ can be calculated. In this case γ is defined as the fraction of time that the boundary layer is fully turbulent, while f_i is the number of times per second that the flow shifts from turbulent to inviscid pressure levels.

4.5 Separation Shock Position and Velocity Histories

The boxcar signals derived from applying the two threshold method described in Section 4.3 to simultaneous pressure signals in the intermittent region allow a piecewise continuous measurement of the shock foot position history, $X_s(t)$ (Dolling et al. 1992). This process is shown in Figure 4-2(a-d).

Figure 4-2(a) shows the transducer setup and bin labels for a multi-channel intermittent region wall pressure measurement. Nested boxcar signals calculated by the two-threshold method as applied to compression ramp data are shown in Figure

4-2(b). The rise and fall times in the nested boxcar sequence indicate the instantaneous position of the separation shock foot. Linear interpolation is then used to create the piecewise smooth function $X_s(t)$, Figure 4-2(c). A simple differentiation of $X_s(t)$, made by dividing the distance between transducers by the time it takes the shock to cross the bin, yields $V_s(t)$, figure 4-2(d).

It is assumed that the shock moves in one direction at a constant speed when traveling from one transducer to the next. If the shock changes direction, it is assumed to move to the midpoint of the bin between two transducers, turn around, and travel back at the same velocity. As long as the transducer captures a large portion of the intermittent region, the assumed shock velocities for turn-arounds and inter-bin movements are comparable to those calculated from more exact measurements of the separation shock position (Kleifges 1993). The far upstream and downstream transducers do not satisfy this velocity condition. Instead, the shock spends a disproportionate amount of time in these bins, and the velocity is far different from the assumed one. Gonzalez (1993) altered the algorithm to prevent the shock velocity from being skewed towards the assumed value due to this condition.

Once calculated, the shock position and velocity histories can be analyzed using standard statistical and time series analysis.

CHAPTER 5

RESULTS

5.1 Probe/Wall Interference Tests

The results of the probe/wall interference tests are shown in Figure 5-1. When the transducer-tipped pitot probe comes within 0.18 in. of the wall-mounted transducer, interference is apparent in the form of an increase in \bar{P}_w . As the probe draws continually closer, \bar{P}_w reaches a maximum, then begins to decrease. This is likely due to a small interaction at the wall caused by the impact of the probe tip's swept bow shock. As the probe moves lower, the area of local separation generated by the glancing shock wave passes upstream towards and over the wall transducer.

Although there is interference at the wall with the probe at $Z \approx 0.18$ in., it does not appear to affect the pitot measurements. While it is difficult to draw conclusions without similar data for comparison from a probe of smaller diameter, the pitot probe data shown in Figure 5-1 is apparently corrupted around $Z \approx 0.04$ - 0.06 in. by either the local flow separation caused by the interaction described above, or possibly the shock itself reflected from the wall below. Due to the transducer diameter of 0.064 in., measurements for both the wall and probe signals stop at $Z = 0.0325$ in., the center of the probe tip when it touches the floor.

These results provide confidence that pitot pressure data measured in this Mach 5 flow at transducer-tipped probe heights of 0.06 in. and greater are free from probe/wall interference.

5.2 Phase 1: Turbulent Boundary Layer Study

5.2.1 Boundary Layer Survey

The conventional probe shown in Figure 3-1(a) was used to measure boundary layer pitot pressures from near the wall to well into the freestream. Instantaneous probe heights measured by the LVDT were corrected by -0.0195 in., accounting for the 0.0235 in. downward deflection due to loading and the 0.004 in. half-height of the probe tip. Figure 5-2(a) shows the boundary layer pitot pressure profile provided by the PRELEAST code. Figure 5-2(b) presents the boundary layer velocity profile generated by LEAST in u^+ , y^+ coordinates. It also provides a comparison to Gibson's results, shown in the inset. The plots have lower limits of $y^+ \approx 100$ due to probe/wall interference.

5.2.2 Mean Boundary Layer Properties

The mean boundary layer properties calculated by PRELEAST/LEAST were presented in Table 3-3. Values for each of the parameters in the current study given varied by less than $\pm 1.5\%$ for repeated experiments. Table 5-1 presents the differences between the current survey results and those of Gibson (1990), which were measured under the same freestream conditions using a position on the flat plate 0.01 in. upstream of the current survey point. Note that the parameter exhibiting the greatest deviation, Π , is extremely sensitive to changes in the fit to the near-wall u^+ , y^+ profile defined by the wall-wake law, and a 15-20% change is to be expected.

Table 5-1: Differences in Flat Plate Mean Boundary Layer Properties Between Gibson (1990) and the Current Study

Parameter:	Change:	Parameter:	Change:
δ_o	+ 0.8 %	Re_∞	+ 1.1 %
δ^*	+ 2.4 %	Π	+ 15.5 %
θ	+ 1.6 %	C_f	- 8.2 %

Using the relationship of Das (1987), the wake parameter Π can be related to the non-dimensional pressure gradient by the following equation:

$$\frac{\delta^*}{\tau_w} \frac{dp_e}{dx} = -0.4 + 0.76 \Pi + 0.42 \Pi^2 \quad (5-1)$$

The wake parameter value of the current study indicates a slightly adverse pressure gradient: for $\Pi = 0.472$, $dp_e/dx \approx 0.05$.

Summarizing, Figure 5-2(b) and Table 5-1 demonstrate a close match between the current experimental results and those of Gibson (1990), who conducted additional spanwise measurements and found a nominally two-dimensional, adiabatic boundary layer. Thus, although the current study provides no spanwise measurements, the flat plate boundary layer is assumed to be two-dimensional and adiabatic in this case as well.

5.2.3 Boundary Layer/Freestream Interface Fluctuating Characteristics

Recall, as discussed in Chapters 1 and 2, that McClure (1992) found a maximum f_i of 5.5 kHz at $Z/\delta_1 \approx 0.95$ on the tunnel floor. Erenkil (1993) and Schmisser (1992) found that the shock-induced pressure fluctuation power spectra had concentrations of energy around 5-7 kHz for swept compression ramp and sharp fin interactions generated in the tunnel floor turbulent boundary layer. Shock zero crossing frequency distributions also exhibited *maximums near 5 kHz* in these interactions. It was these results which originally suggested a link between the passage of turbulent structures at the boundary layer/freestream interface and the separation shock dynamics. In addition, Gibson (1990) observed a concentration of energy around 8-10 kHz in the compression region of a shock wave turbulent boundary layer interaction generated by a sharp fin at angle-of-attack on the flat plate (Figure 2-18(c)). Therefore, a clear question exists: does the flat plate turbulent boundary layer f_i correlate with higher sharp fin interaction fluctuation power spectra already observed there? As the first objective of this thesis, the question has been answered as follows.

The transducer-tipped probe was used to measure pitot pressure fluctuations caused by the downstream flow of turbulent structures at the boundary layer/freestream interface. Data were collected at 0.015-in. intervals from $Z/\delta_1 \approx 0.59$ to 1.81, at a station 19 inches downstream of the plate leading edge. As shown in Figure 5-3, the region of intermittently turbulent flow extends from $Z/\delta_1 \approx 0.70$ to 1.40. Within the intermittent region, the interface crossing frequency increases to a

maximum of 6.5 kHz at $Z/\delta_1 = 1.05$. Intermittency and interface crossing frequency values were calculated by an algorithm which applied the VITA analysis described in Section 4.4 using the appropriate thresholds identified by McClure (1992). Figures 5-4 and 5-5 present intermittency and interface crossing frequency profiles, respectively, for the current study as well as McClure's experiments conducted in the thicker tunnel floor boundary layer.

These results show a weak correlation at best between f_i and shock-induced pressure fluctuations. While the sharp fin interaction generated in the thinner boundary layer exhibited concentrations of fluctuation energies at frequencies 50% higher than those interactions within the tunnel floor boundary layer, the flat plate boundary layer f_i is only about 18% greater. This negative result is consistent with conclusions drawn from the concurrent work of Erenkil and Dolling (1993b), which identifies the instantaneous static pressure ratio across the shock, P_1/P_2 , as the driving mechanism behind the high frequency, small-scale separation shock motions and associated wall pressure fluctuations. Large-scale, low frequency shock motion is apparently caused by the expansion and contraction of the separated flow region, which may in turn be driven by both the incoming turbulent boundary layer fluctuations as well as recirculating turbulent structures within the separated region.

The discrepancy between the intermittency profile of the current study and that of McClure (1992) may be attributed to inadequate spatial resolution. The ratio of the intermittent region thickness to the transducer tip diameter is about 2.6 for the flat plate boundary layer, while on the tunnel wall, the ratio is approximately 8. As

discussed in the conclusions of Chapter 6, this could be resolved by using a hot-wire probe, providing ratios on the order of 10^3 .

Moreover, several characteristics of the data differ between the two studies. Figure 5-6 shows samples of raw data signals, PDDs, and PSDs from tunnel floor boundary layer data sampled at 100 kHz and filtered at 40 kHz. Near 90% γ , the signal becomes sharply skewed and remains so until $\gamma \approx 10\%$. PSDs show a low frequency (200 - 500 Hz) contribution to the fluctuation energy spectra that decreases with intermittency. Within the fully turbulent boundary layer, a large concentration of the fluctuation energies are centered around 25 kHz. As the intermittency decreases, the fraction of energy at the higher frequencies increases until, at $\gamma \approx 1\%$, the greatest fraction of the spectra is located at 40 kHz or higher. The filter obviously masks contributions greater than 40 kHz.

By comparison, Figure 5-7 presents signal characteristics from the flat plate boundary layer for similar values of the intermittency. The sampling frequency is again 100 kHz. Qualitatively, the raw data are similar. Statistically, as γ increases, the skewness increases gradually while the largest fraction of the fluctuation spectra shifts from a broad peak at 8-20 kHz to a sharp peak near 25 kHz. Unfortunately, inadvertently filtering at 25 kHz destroyed spectral contributions from higher frequencies.

5.3 Phase 2: Blunt Fin-Induced Interaction

This section presents an analysis of simultaneous fluctuating pitot pressure data measured within the upstream undisturbed boundary layer, under the translating

separation shock, and along the blunt fin leading edge. Data were sampled at either 200 or 500 kHz and filtered at 50 kHz. Sections 5.3.1-4 present sample and statistical data for the pitot probe pressure signals, intermittent region wall pressure signals, intermittent region shock dynamics, and fin leading edge surface pressures. Section 5.3.5 shows results of cross-correlations between various combinations of the probe and fin leading edge pressure fluctuations, intermittent region wall pressure fluctuations, and separation shock dynamics.

5.3.1 Upstream Near-Wall Pitot Probe Signal Characteristics

Fluctuating pitot pressure measurements were made 8.05 in. ($X/D = 10.73$, $X/\delta_0 = 13.64$) upstream of the blunt fin leading edge at heights above the wall of 0.2 and 0.3 in. ($Z/\delta_0 = 0.34$ and 0.51). Figure 5-8 shows sample probe raw data signals, PDDs, and PSDs. At $Z/\delta_0 = 0.51$, the maximum fluctuation frequency concentration lies around 20 kHz. The power spectra drops off to a minimum near 1 kHz, then increases slightly at 200-300 Hz. The lower probe position, $Z/\delta_0 = 0.34$, shows a shift towards lower frequencies. The peak of concentrated energies in the spectrum is broader, of lower amplitude, and centered near 15 kHz. The low frequency component near 200 Hz has increased in amplitude.

5.3.2 Intermittent Region Wall Pressure Signal Characteristics

Figure 5-9 presents wall pressure signals measured throughout the intermittent region in the absence of the upstream pitot probe. Sample raw data, PDDs, and PSDs display the characteristics of a translating separation shock as described in Chapter 2.

The high frequency, low amplitude turbulent boundary layer pressure fluctuations have relatively low frequency, high amplitude fluctuations imposed by the separation shock motion. As γ increases to approximately 50%, the PDDs become bimodal due to the higher mean pressure associated with the separated flow downstream of the instantaneous shock position. Power spectra contributions, centered at 0.8-1 kHz, gradually decreases with increasing intermittency, while contributions to the spectra at 30-40 kHz, while minor, show a decrease from boundary layer levels followed by an increase due to the separated flow.

Figure 5-10 illustrates the upstream pitot probe effects on the intermittent region characteristics. The case shown is for the probe at $Z/\delta_0 = 0.51$ since the highest probe height is expected to generate the most interference. The intermittent region shifts approximately 1ζ (0.115 in.) upstream, increasing the overall interaction length by approximately 4%. In this study the interaction length is defined as the distance from the fin leading edge to $\gamma = 5\%$. For a given γ , PDDs and PSDs were qualitatively and quantitatively unchanged, as shown by comparing Figures 5-9 and 5-10.

The small change in the interaction length scale due to the upstream probe interference is apparent in the mean and RMS pressure distributions across the intermittent region, Figure 5-11. Data for the two near-wall probe experimental configurations are included, as well as undisturbed interaction data from the current study and a previous experiment done by Brusniak (1991) in the same facility. Each data point (exclusive of Brusniak's data from a single experiment) is an average of between four and eight tunnel runs under the same conditions. The mean pressure

distribution displays the characteristic rise associated with separation. The RMS pressure distribution increases to an expected peak in the intermittent region near the downstream limit of the separation shock movement ('S' in Figure 1-1) before decreasing under the separated flow. The probe at $Z/\delta_0 = 0.34$ does not noticeably affect the mean pressure distribution and increases RMS values only slightly. At $Z/\delta_0 = 0.51$ the higher mean and RMS pressures at a given X/D are apparent.

Intermittency and zero-crossing frequency profiles are shown in Figure 5-12. Again, the data associated with the current study are averages of the results of multiple experiments under identical conditions. The probe at $Z/\delta_0 = 0.51$ shifts the profiles upstream by about 1ζ as indicated in the pressure distributions. The maximum, $f_c = 1.2$ kHz, occurs at $\gamma = 50\%$ and correlates well with the intermittent region power spectra from Figures 5-9 and 5-10. At $Z/\delta_0 = 0.34$ the effects are less severe but still apparent. The highest probe height may decrease the maximum f_c slightly, but the sparseness of the data prevents a definitive conclusion.

5.3.3 Separation Shock Dynamic Characteristics

Figure 5-13 shows samples of shock foot velocity and position histories which result from applying the two threshold method described in Chapter 4 to the intermittent region wall pressure signals. Corresponding PSDs are included. Shock velocity fluctuations are centered around 3-5 kHz, while shock position power spectra exhibit a concentration in fluctuation frequencies at 0.5-0.6 kHz. The presence of an upstream probe generates no apparent change in the shock dynamics or their spectra.

5.3.4 Leading Edge Stagnation Pressure Signal Characteristics

As described in Chapter 2 and shown in an inset of Figure 1-1, a supersonic jet originating at the triple point impacts on the fin leading edge, creating high mean and RMS pressures. Because of separation shock unsteadiness, the impact point on the leading edge will fluctuate vertically as the shock translates in the streamwise direction.

Figure 5-14 presents raw data, PDDs, and PSDs from four positions along the fin leading edge. As expected, the sample raw signals are characterized by high amplitude, high frequency fluctuations whose maxima may reach four times the mean value. The PSDs are characterized by a concentration of energy around 15 kHz and broadband, lower-amplitude contributions from 2-5 kHz. As Z/D increases, the fraction of power near 15 kHz decreases while frequency contributions from the band below 1 kHz increase noticeably.

Figure 5-15 presents mean and RMS pressure distributions at the leading edge with and without the upstream pitot probe in place. The presence of the probe decreases the mean pressure and RMS pressure by 5-7% and 10-33%, respectively. Changes of this magnitude are not surprising since the pressure distribution along this portion of the leading edge is characterized by a steep gradient (Figure 2-11(a-c) illustrates this for the mean pressure). Thus, a small change in the streamwise interaction length caused by the presence of the probe (which leads in turn to a small shift in the jet impact point) significantly alters the mean and RMS pressures.

5.3.5 Summary of Upstream Probe Effects on Interaction Characteristics

The presence of the upstream probe at its greatest height above the wall lengthens the interaction by 4%, shifting the intermittent region 1ζ upstream. While the leading edge mean and RMS pressures reflect this through moderate decreases in undisturbed levels for a given value of Z/D from the current study, other interaction characteristics remain apparently unaltered, including intermittent region length and separation shock dynamics. These results allow the analysis to proceed to more complex relationships between fluctuating quantities from different points in the flow. The goal is to identify the characteristic pressure fluctuations, if any, that are associated with the separation shock dynamics.

5.3.6 Cross-Correlations

The following two sections present results of cross correlations between fluctuating quantities. Section 5.3.6.1 focuses on correlations between pressure fluctuations alone, while Section 5.3.6.2 presents correlations between shock dynamics (velocity and position histories) and pressure fluctuations in the incoming boundary layer or the fin leading edge. The task is to analyze the correlations between the high-amplitude surface pressure fluctuations at the leading edge and either the incoming boundary layer pitot pressure fluctuations, the intermittent region fluctuating wall pressures, or the separation shock position and velocity histories. These correlations should allow strong, clear indications of the effects of upstream

and downstream propagating pressures on the separation shock dynamics, as well as defining the timing associated with such events.

5.3.6.1 Correlations Between Pressure Fluctuations Only

Figure 5-16 presents cross-correlations between intermittent wall pressure signals at six values of γ and upstream fluctuating pitot pressures. A seventh correlation between fluctuating pressures on the fin leading edge and the pitot fluctuations is also included.

The six correlations between the intermittent region pressures and the pitot probe are qualitatively similar. In general, the peak labeled 'P1', a negative correlation coefficient at a negative time delay, τ , between the intermittent region pressures and the pitot probe, is logical. A turbulent eddy (or some other pressure fluctuation) passing over the pitot probe travels a fixed distance to an individual intermittent region wall transducer at some fraction of the freestream velocity. As the eddy encounters the separation shock, it effects the shock movement, generating fluctuations in the wall pressure signal. Since the downstream intermittent region signal is being correlated with the upstream pitot probe, the time delay τ is negative. The negative correlation coefficient indicates that increasing (decreasing) pitot pressures are associated with decreasing (increasing) wall pressures.

However, P1 does not represent the passage of a turbulent structure downstream. If it did, the convective velocity, u_c , calculated from the time delay τ associated with P1 and the separation distance between the probe and the intermittent region location should be approximately 80% of U_∞ as shown by Brusniak and

Dolling (1993). In fact, the τ associated with P1 corresponds to $u_c = 0.40 U_\infty$. This relatively slow convective velocity along with the broadness of the correlation suggests a low frequency source for P1. If the low frequency fluctuation period equals the time span for which the correlation coefficient is negative, a pressure variation occurs in the incoming boundary layer flow at a frequency of about 500 Hz.

A second feature of the six intermittent region/pitot probe correlations is indicated by 'P2'. The time delay for P2 coupled with the probe/intermittent channel separation distance corresponds to $u_c = 0.80 U_\infty$. The peak is also sharper, suggesting a higher frequency contribution. Although P2 is masked in part by the low frequency portion of the signal, these results indicate that it is the result of a downstream propagation of turbulent structures.

The seventh curve from Figure 5-16 shows a very strong positive correlation between the fin leading edge pressure fluctuations and the pitot probe. From the separation distance between the pitot probe and the fin leading edge and the t indicated at the peak, $u_c = 0.75 U_\infty$. This slight reduction in u_c below 80% U_∞ supports the observation made by Brusniak and Dolling (1993) that the turbulent eddies are decelerated by the separated shear layer downstream of the separation shock. Figure 5-17 examines the pitot probe/leading edge pressure fluctuation correlation in greater detail. As shown, the stronger correlations are generated from pressure fluctuations measured at the highest point on the leading edge and at either boundary layer probe position; they also have a slightly shorter time delay, indicating a higher value of u_c , compared to the lower leading edge position. Both time delays correspond to approximately $u_c = 0.75 U_\infty$. This indicates that, for $Z/\delta_0 = 0.34-0.51$, the position

of the probe in the boundary layer is not critical to the timing of structures through the interaction. These strong correlations are also evidence that a large fraction of the turbulent structures entering the interaction from the upstream boundary layer remain coherent as they are processed by the separation shock and the separated flow region, creating the opportunity for them to recirculate and further affect the separation shock dynamics. Of additional interest is the broad base of these otherwise narrow correlation curves. Again, this broad portion of the correlation corresponds to pressure signal fluctuations on the order of 500 Hz.

Figures 5-18 and 5-19 show correlations between intermittent region wall pressures and fin leading edge surface pressure fluctuations. The normalized correlation coefficients are negative for the same reasons as the six correlations shown in Figure 5-16: a decreasing (increasing) wall pressure corresponds to an increasing (decreasing) leading edge pressure. More specifically, if the pressure at a given point in the intermittent region is falling, the shock is moving downstream of that point. The further downstream the separation shock, the lower the jet impact point on the leading edge, bringing the most extreme pressure levels closer to the transducer there. Thus pressures rise. The curves are broad, again indicating a low frequency fluctuation; however, high frequency components are also present. For example, in Figure 5-19, at $\gamma = 100\%$, two sharp peaks are apparent. Further investigations are needed to identify their significance.

5.3.6.2 Correlations Between Pressure Fluctuations and Shock Dynamics

The two threshold conditional sampling algorithm introduced in Chapter 4 allows shock foot velocity and position histories to be calculated from wall pressure fluctuations throughout the intermittent region. This has the advantage of generating a continuous signal representing the separation shock motion. In contrast, pressure fluctuations at a single position correlated with another event only make use of a fraction of all the perturbations which occur within the intermittent region. That fraction may be very small, resulting in weak or misleading correlations.

In Figure 5-20, the shock foot position and velocity histories are correlated with pitot pressure fluctuations at $Z/\delta_0 = 0.34$ and 0.51 . Insets show the characteristic double-peaked shape of the correlations over a longer time span. The peaks in this correlation are positive and occur at a negative τ , indicating that increases (decreases) in the shock velocity and changes in the shock position follow increases (decreases) in pressure at the pitot probe. Figure 5-21 shows a similar correlation between the shock foot dynamics and the leading edge surface pressure at $Z/D = 0.38$. The correlations for a given arrangement are positive and generally of the same shape as those in Figure 5-20, but shifted in the time delay, τ . This gives one of the two peaks for each correlation a positive τ , indicating that some changes in the shock dynamics lead surface pressure fluctuations at the leading edge, while others follow them. This is possibly an indication of recirculation within the separated region. Further interpretation of these correlation shapes is beyond the scope of this study.

5.3.7 Ensemble-Averaged Pressure Histories

By choosing one channel as a trigger and combining the individual ensembles measured by each channel at the time of the trigger event, characteristic pressure signatures and their timing can be obtained. Figures 5-22, 5-23, 5-24, and 5-25 present ensemble-averaged pressure histories associated with a specific direction of shock sweep over a chosen trigger channel. All four figures are constructed using data from the same experiment. Similar results have been obtained from the other experimental configurations used in the Phase 2 tests.

These figures verify the positive/negative senses of the correlations presented in the previous two sections. As shown in Figures 5-22 and 5-23, which show ensemble pressure signatures associated with a downstream separation shock sweep over channels 1 and 4 respectively, a generally rising pressure level at the pitot probe, (a), corresponds to a falling pressure across the intermittent region, (b)-(g), and a rising pressure at the fin leading edge, (h). The opposite trends are seen in Figures 5-24 and 5-25, which show ensembles triggered by an upstream shock sweep. These rising and falling pressure levels occur at low frequencies with periods exceeding the time span of the ensembles.

These figures also indicate a high frequency characteristic signature associated with the shock sweeps. The pressure fluctuation signature of interest has been labeled 'A' in the pitot probe ensemble (a) of each of the four figures. For a downstream sweep (rising pitot pressure level), the characteristic event is a short duration peak in the pressure level, while upstream sweeps seem to be associated with a sharp, temporary decrease in the already falling pressure levels. Moreover,

pressures signatures at the leading edge display a characteristic sharp rise or fall in their already rising and falling levels, indicated in ensemble (h) of each figure, which, based on the time delay and separation distance between the pitot probe and leading edge, correspond to convective velocities of 60 - 80% U_∞ . The events are not always clearly demarcated compared to the surrounding ensemble pressure noise levels. However, for the experimental configuration shown here and four others also used in the ensemble average pressure analysis, an appropriately positive (negative) peak, depending on falling (rising) or rising (falling) pressures at the intermittent region (leading edge), larger and of higher amplitude than the surrounding rising (falling) levels, was visible. If this signature in the incoming turbulent boundary layer is in fact a higher frequency event which is then responsible for the downstream or upstream shock sweeps, it is the first such demonstration of its existence, to this author's knowledge.

Within the intermittent region ensembles, there are characteristic pressure signatures similar to those previously introduced in Figure 2-20(a,b) from McClure (1992). Figure 5-23, a downstream sweep over channel 4, $\gamma = 50\%$, shows a rising-falling-rising (R-F-R) signature in (b)-(d) which is concurrent with the separation shock when it triggers the ensemble in (e). In contrast, Figures 5-24 and 5-25 show a falling-rising-falling (F-R-F) signature which propagates downstream to trigger an upstream shock sweep over a chosen channel.

Overall, these observations are consistent with a model developed by Erengil and Dolling (1993b) which identifies low frequency shock fluctuations as correlating with low frequency pressure fluctuations within the separated flow, which in turn

may be generated by some outside influence, such as near-wall low frequency pressure fluctuations in the incoming boundary layer and separated shear layer. High frequency separation shock jitter is caused by the propagation of turbulent structures through the shock and into the separated vortical flow.

CHAPTER 6

CONCLUSIONS AND RECOMMENDATIONS

6.1 Conclusions

- 1) The turbulent boundary layer interface crossing frequency does not directly correlate with the dominant frequency bands of the spectral energy of separation shock-induced wall pressure fluctuations. While Gibson (1991) found intermittent region wall pressure fluctuation energies from a sharp fin interaction on a flat plate concentrated at frequencies 70-100% higher than those measured by Schmisser (1992) in the same interaction but in the thicker tunnel wall boundary layer, the current study has found an only 18% increase in the thinner boundary layer interface crossing frequency.

- 2) The presence of a floor-mounted, streamlined pitot probe has only a minimal effect on the characteristics of a blunt fin-induced shock wave / turbulent boundary layer interaction approximately $14 \delta_0$ downstream. The interaction length grew by 4%, shifting the intermittent region and its characteristic mean and RMS pressure distributions slightly upstream. The minimal interference observed lends confidence to the interpretation of cross-correlations between pressure fluctuations at various points within the flowfield. These correlations are characterized by both sharp, high frequency peaks associated with the propagation of turbulent structures, and broad, low frequency components. This supports the concurrent work of Brusniak and Dolling (1993). The driving mechanism behind the low frequency signal content is unknown, although it

appears to be due to near-wall boundary layer phenomena. Further investigations are needed to identify its source. There is a strong correlation between high frequency, fluctuating pitot pressures and fin leading edge fluctuating surface pressures, indicating that turbulent structures remain coherent as they pass through the separation shock and separated region. Thus, although no clear evidence was found in the current study, the turbulent structures may recirculate and affect the interaction from its downstream side.

- 3) Several salient features of ensemble-averaged (E-A) pressure histories have been identified:
 - (a) Within the intermittent region, signatures identical to those found by McClure (1992) and Brusniak (1993) correspond to specific separation shock motions. A rising-falling-rising (R-F-R) E-A pressure signature is coincident with the shock during a downstream sweep, while a falling-rising-falling (F-R-F) event corresponds to an upstream sweep.
 - (b) Ensembles from the pitot probe, intermittent region, and leading edge signals are consistent with the cross-correlation results. A gradually rising (falling) E-A pressure at the pitot probe correlates with an E-A pressure fall / downstream sweep (rise / upstream sweep) across the intermittent region and a final gradual rise (fall) at the fin leading edge. This behavior is apparently a result of the low frequency content of the pressure signals.

- (c) Although not always clearly present, the pitot probe ensembles exhibit a characteristic high frequency pulse which may be indicative of the turbulent structure responsible for the signatures and shock motion described in (a), above. The rising (falling) E-A pressure associated with the R-F-R (F-R-F) has a pressure peak (trough) whose time delay, τ and separation distance corresponds with a steep rise (fall) seen in the fin leading edge ensembles, assuming a convective velocity between 60 - 80% U_∞ . This is the first time that a high frequency ensemble-averaged pressure signature apparently responsible for the separation shock jitter has been observed in the turbulent incoming boundary layer.

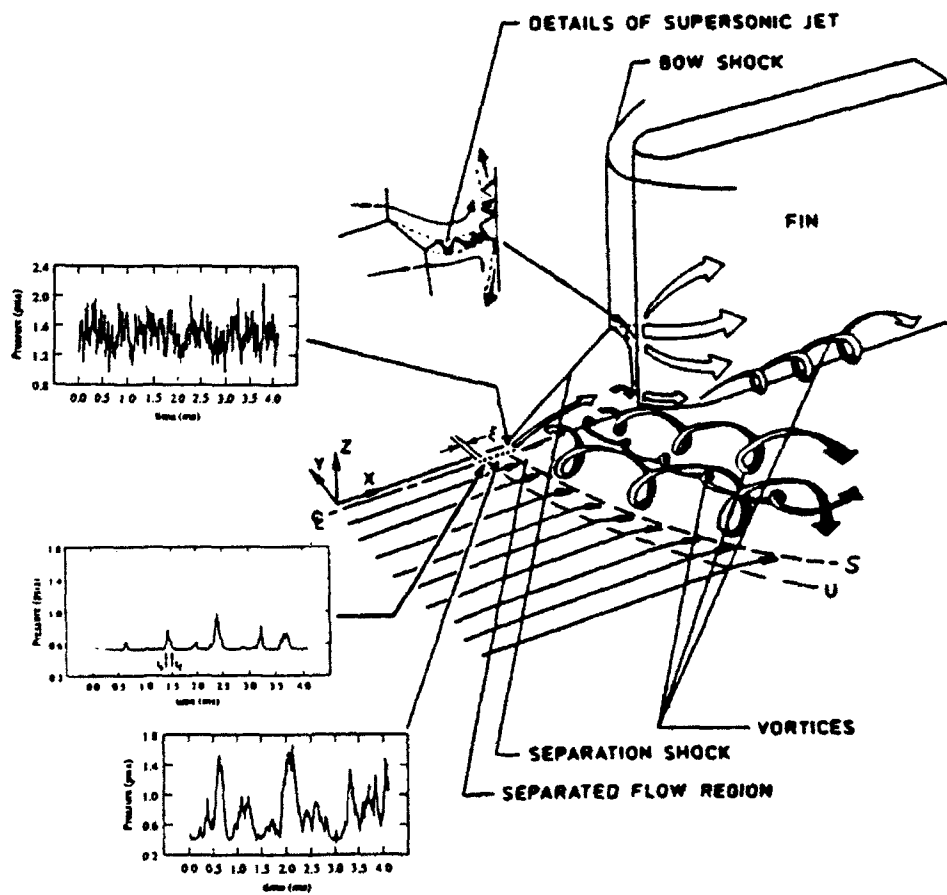
6.2 Recommendations for Future Work

Although the current study has contributed to the current understanding of the effect of incoming boundary layer pitot pressure fluctuations on the unsteadiness of fin-induced interactions, much work remains to be done before a full understanding of the flowfield physics and behavior is gained. Specifically, the following work would build upon the conclusions of this study:

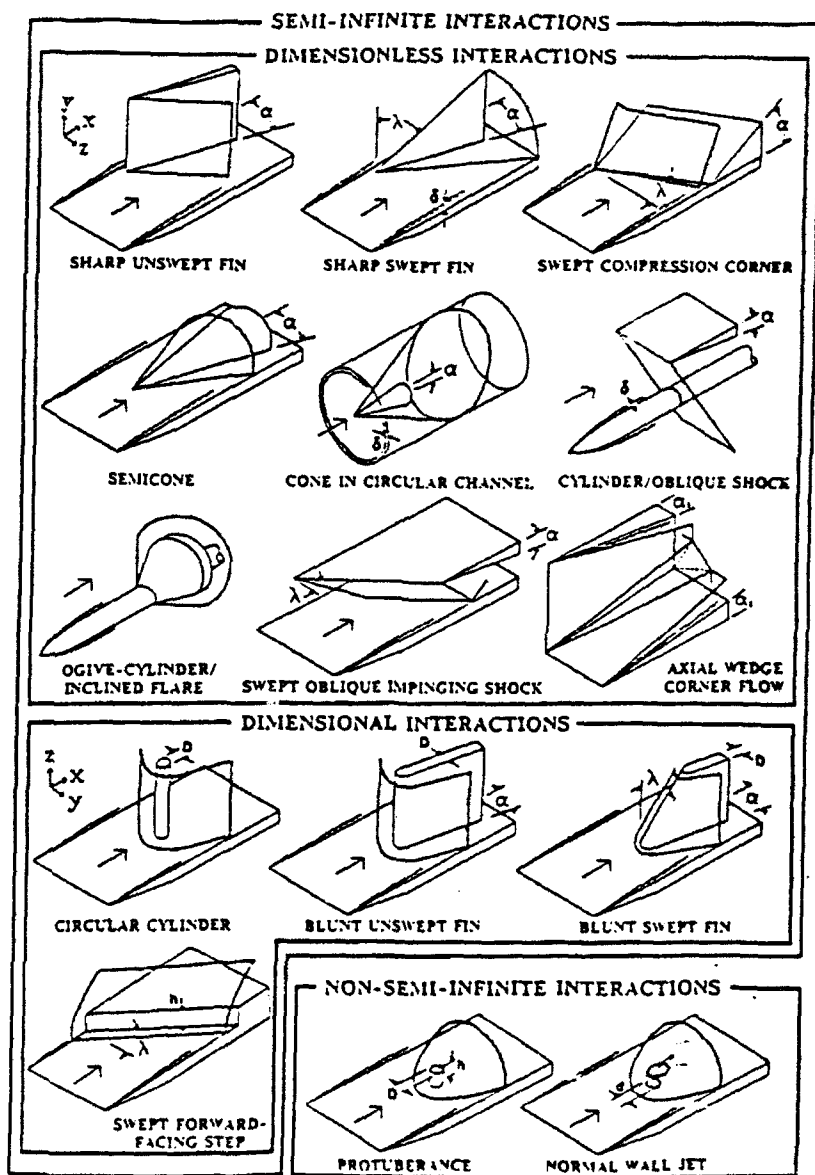
- 1) A more precise measure of the interface crossing frequency from the flat plate boundary layer could be made using a hot-wire probe. This would prevent any resolution problems from corrupting the boundary layer data.

- 2) With respect to the blunt fin interaction, fluctuating pressures could be sampled at several other pitot probe heights as well as within the intermittent region and at the fin leading edge to further investigate the source of the high and low frequency boundary layer pressure fluctuations. Of particular interest would be the confirmation of the high frequency turbulent structure signatures in the pitot probe ensembles and the low frequency pressure fluctuations near the wall. Low frequency contributions might be indicated by electronically low-pass filtering data from the current study.

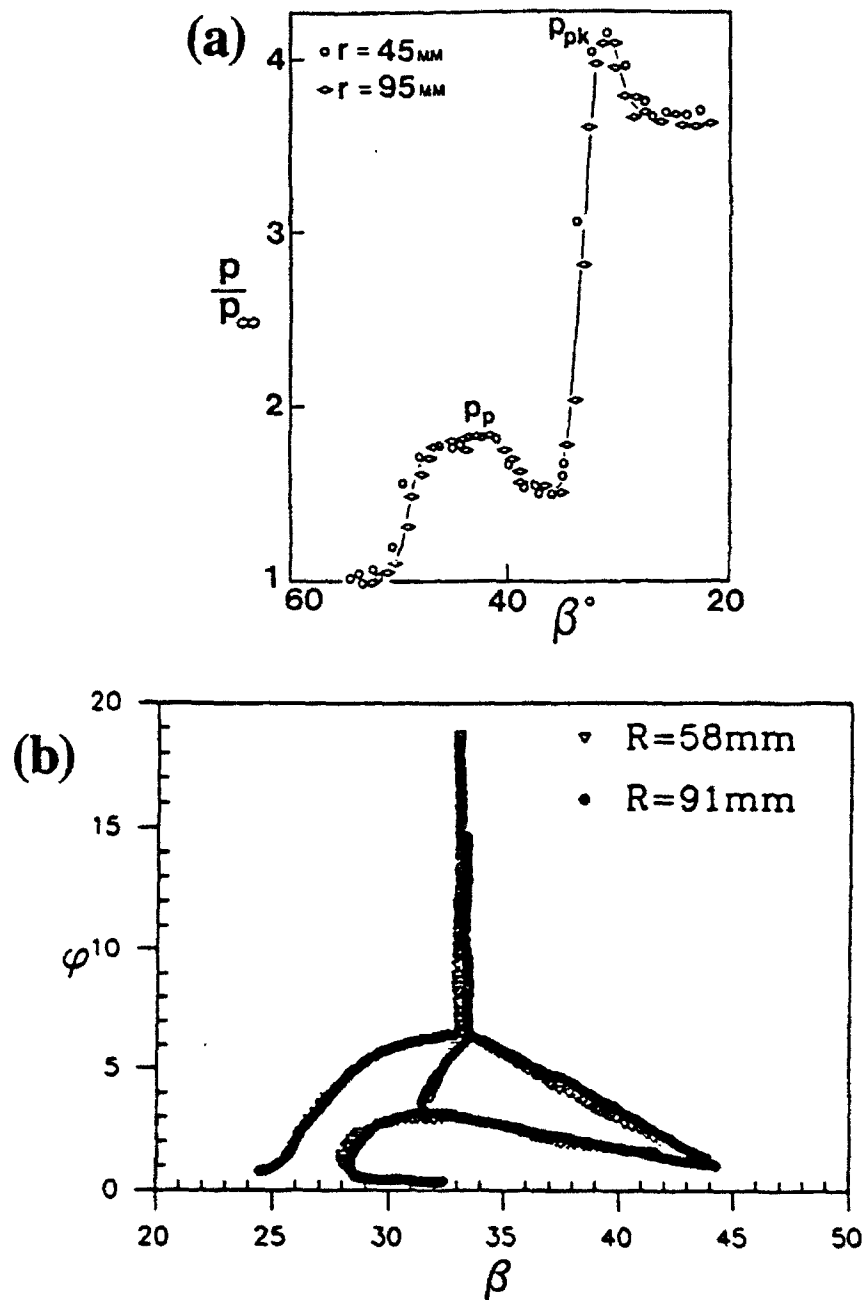
FIGURES



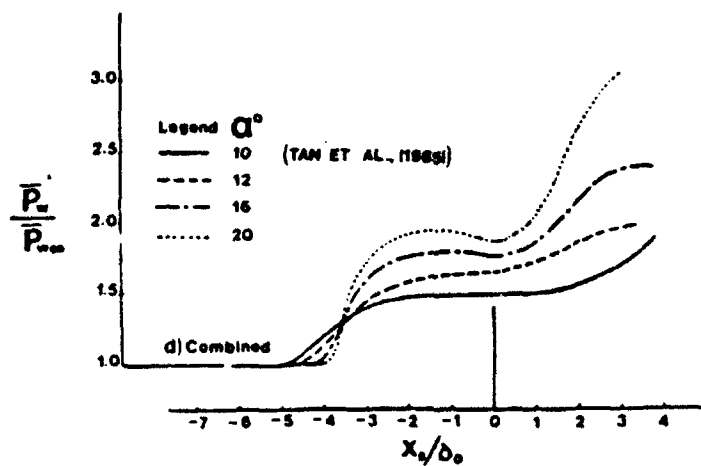
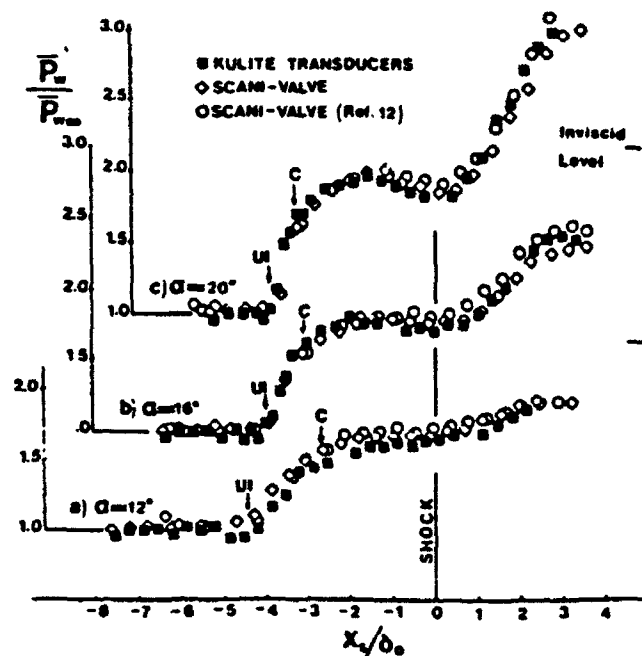
1-1: Blunt Fin Interaction Features and Nomenclature (Lakshamanan and Tiwari 1993, Brusniak 1989)



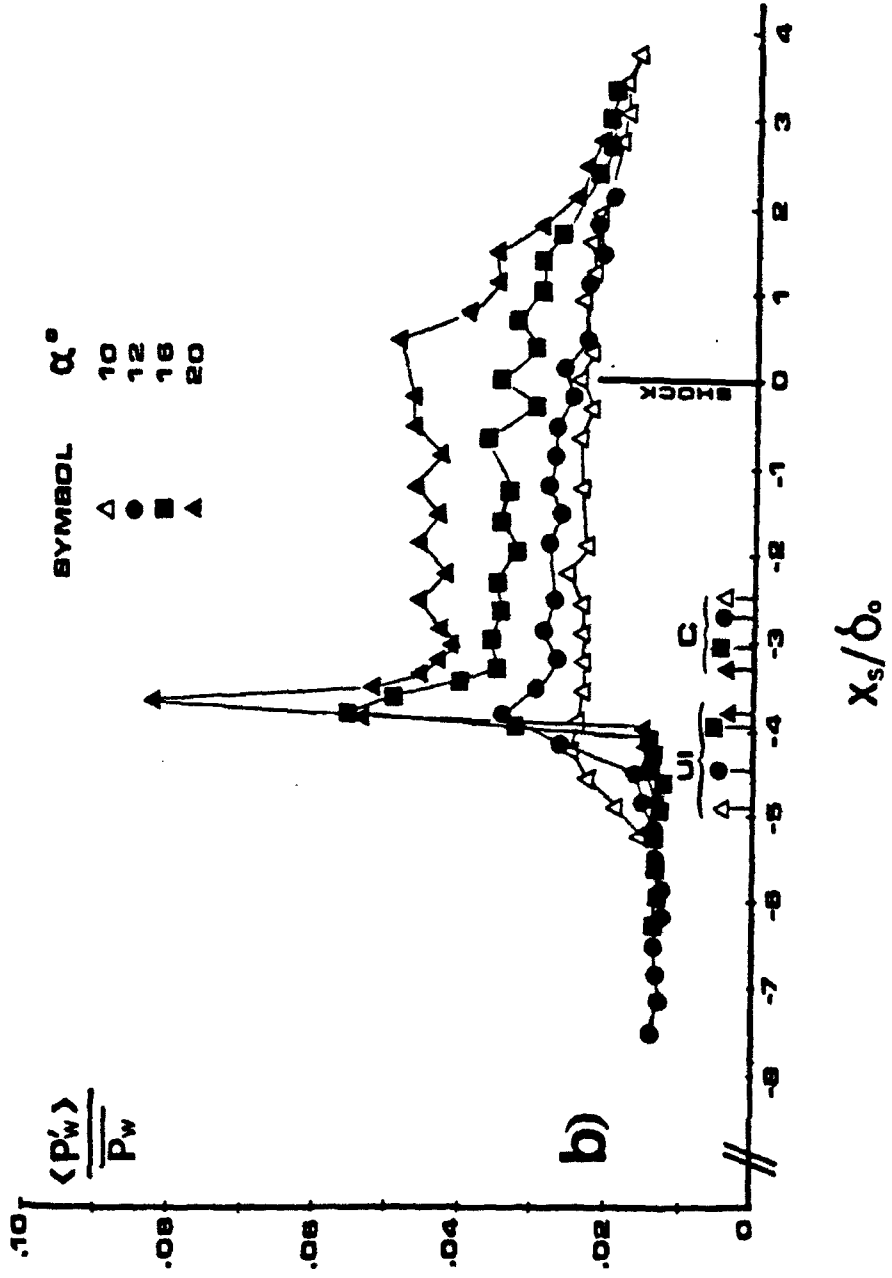
1-2: Swept Shock Wave Boundary Layer Interaction Classification (Settles and Dolling 1986)



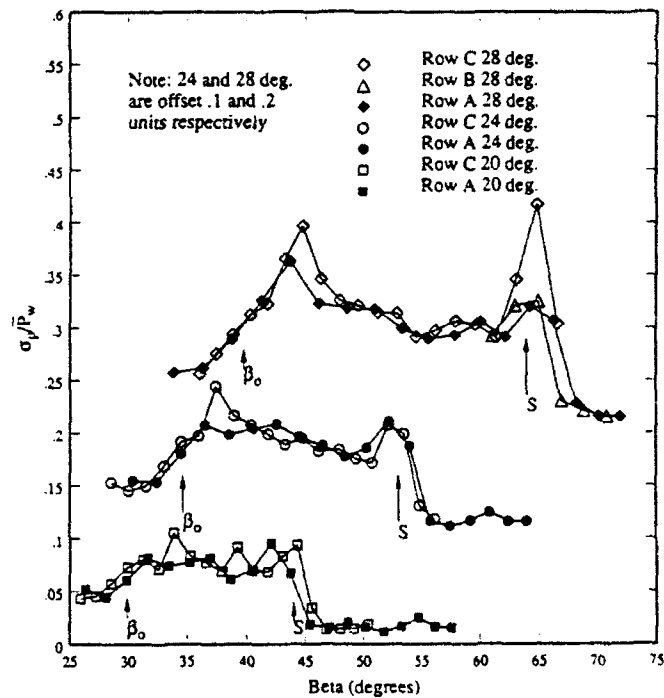
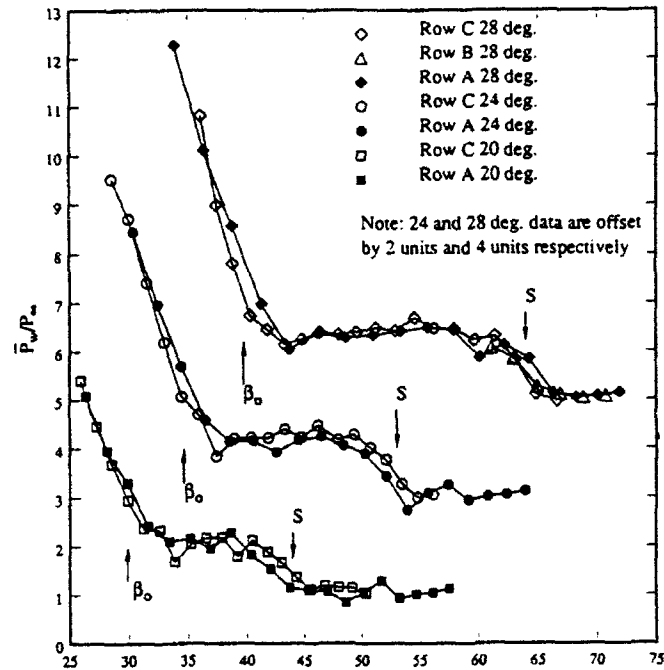
2-1: Quasi-Conical Collapse of (a) Surface Pressure Measurements (Zubin and Ostapenko 1979), and (b) PLS Images (Alvi and Settles 1990)



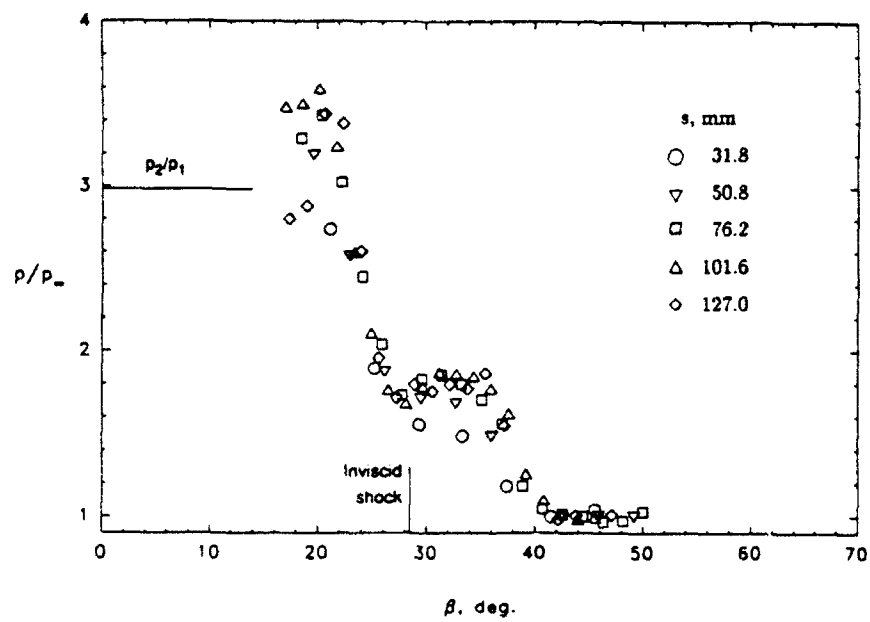
2-2: Mean Pressure Distribution, Mach 3 Sharp Fin Interaction (Tran 1987)



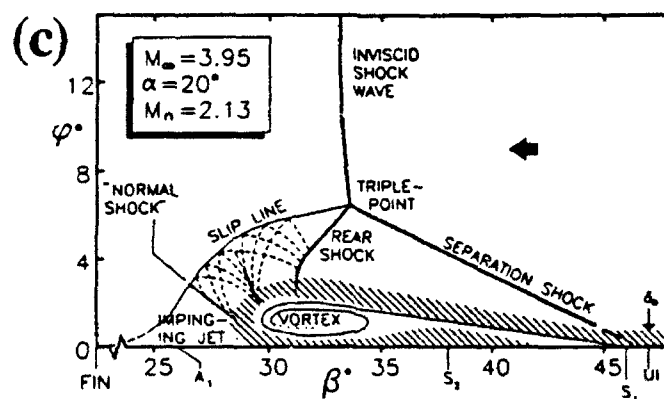
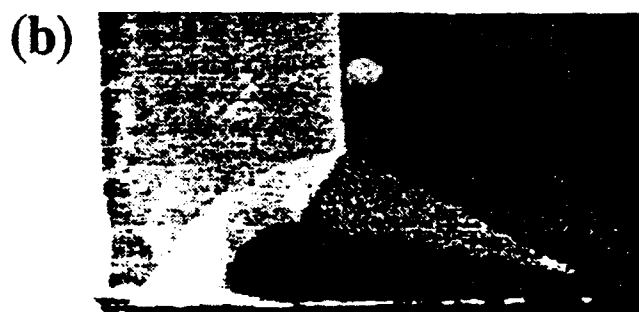
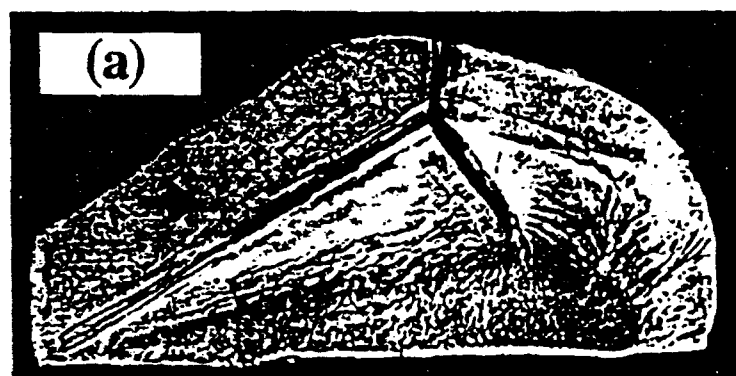
2-3: RMS Pressure Distribution, Mach 3 Sharp Fin Interaction (Tran 1987)



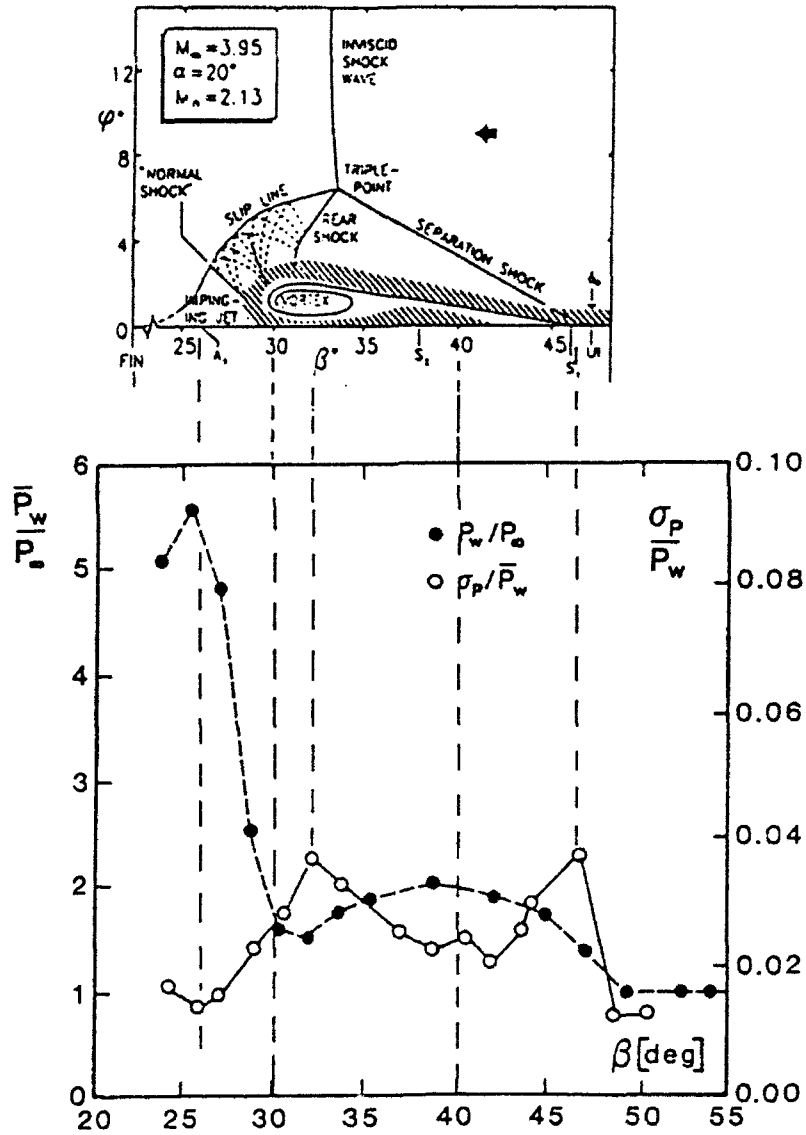
2-4: Quasi-Conical Collapse of Normalized Distributions, Mach 5 Sharp Fin Interaction (Schmisser 1992)



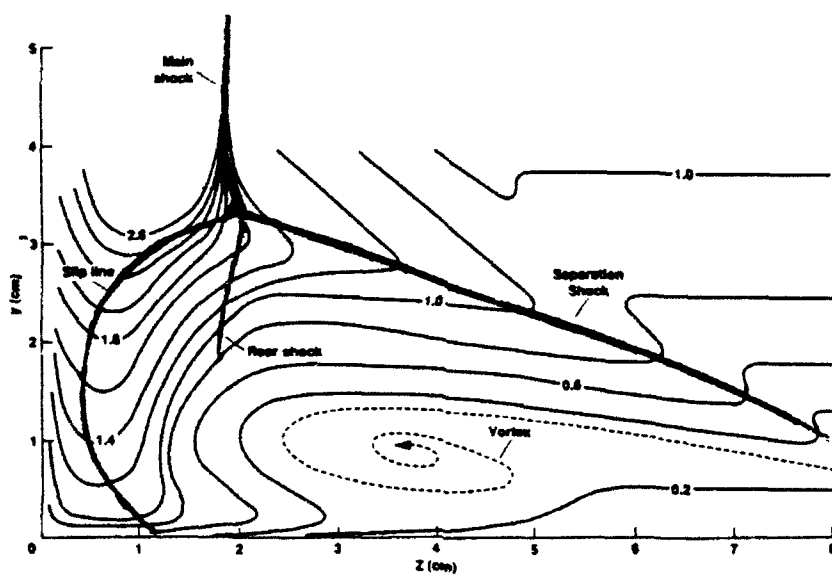
2-5: Inception Region Effects on Quasi-Conical Mean Pressure Distribution, Mach 3.44, $\alpha = 14^\circ$ (Lu 1993)



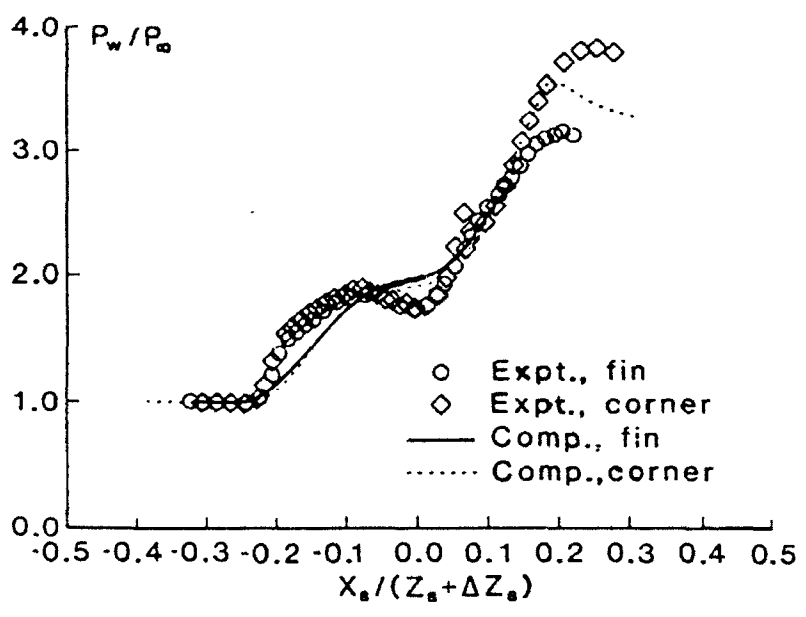
2-6: (a) Shadowgraph, (b) PLS Image, and (c) Flowfield Map, Mach 4, $\alpha = 20^\circ$ Sharp Fin Interaction (Alvi and Settles 1990, 1991)



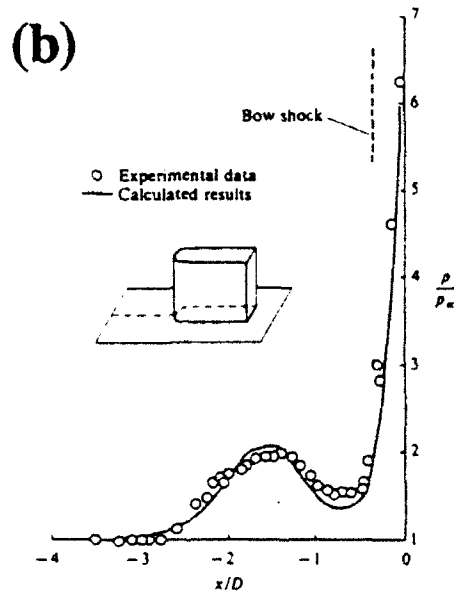
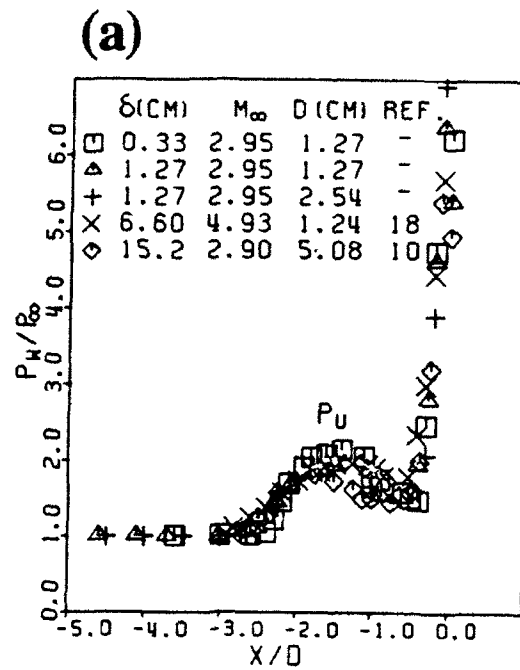
2-7: Mean and RMS Pressure Distributions with Corresponding Flowfield, Mach 4, $\alpha = 20^\circ$ Sharp Fin Interaction (Garg and Settles 1993)



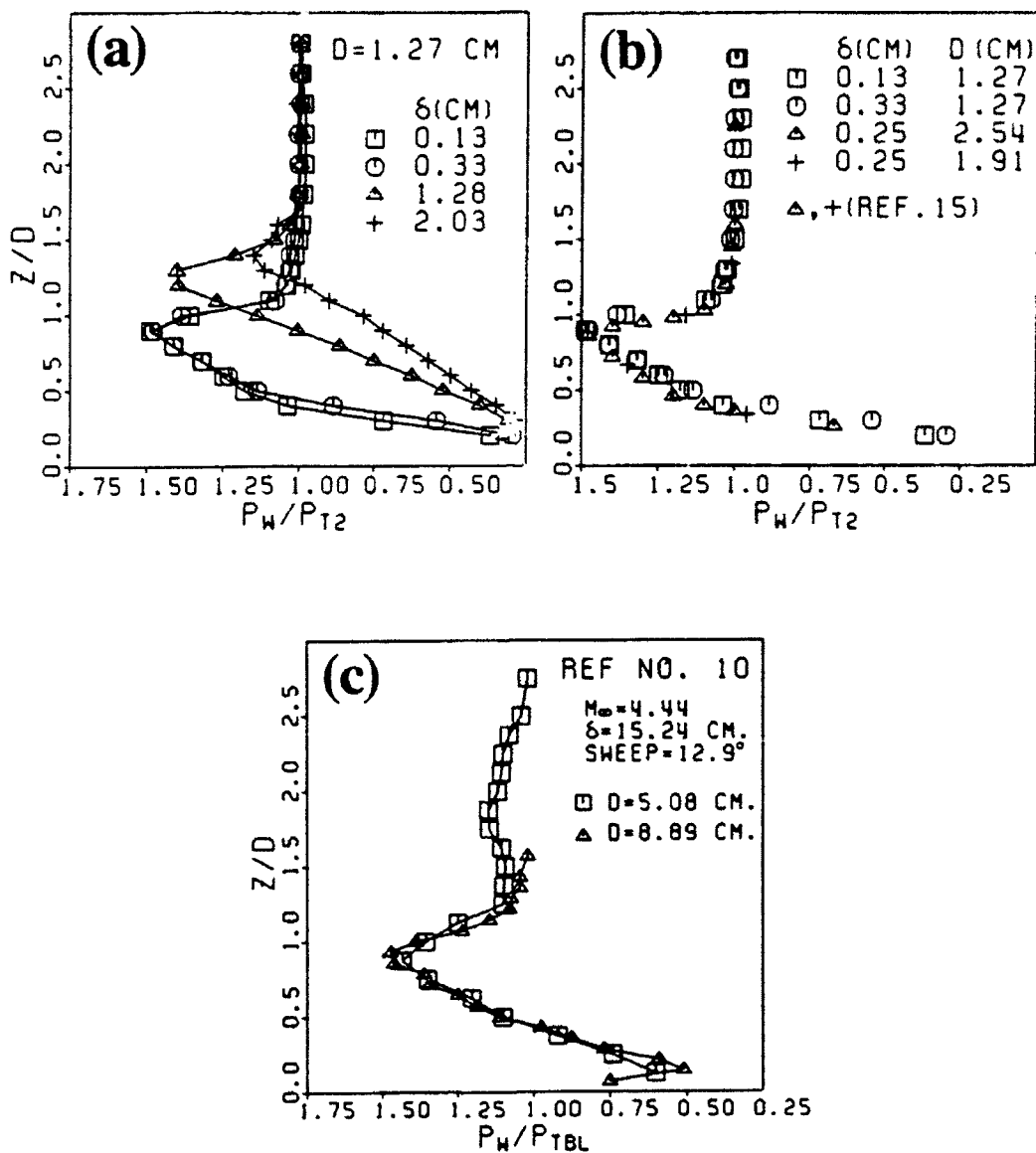
2-8: Flowfield Pressure Contours, Mach 8.2, $\alpha = 15^\circ$ Sharp Fin Interaction (Kussoy and Horstman 1993)



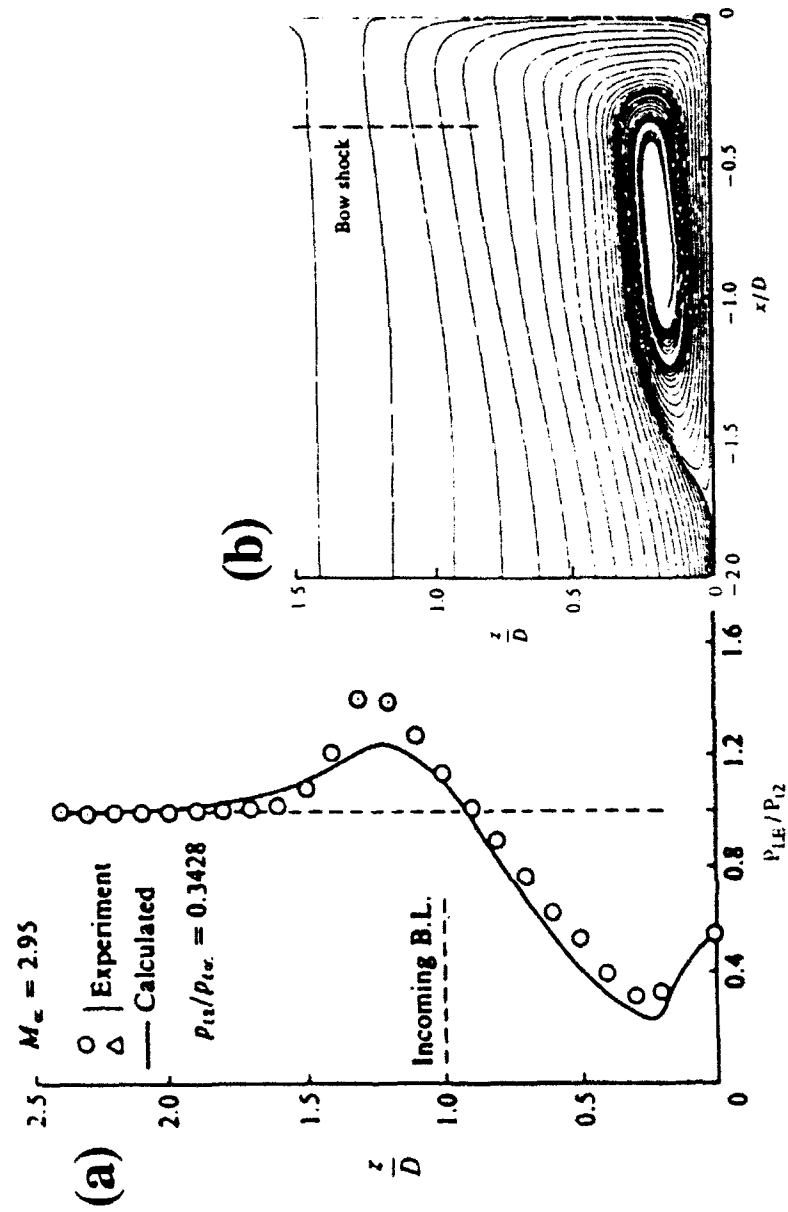
2-9: Experimental and Computed Mean Wall Pressures, Mach 3, $\alpha = 17.5^\circ$ Sharp Fin Interaction (Zang and Knight 1989)



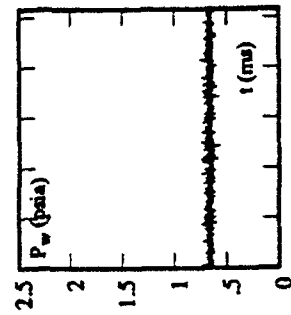
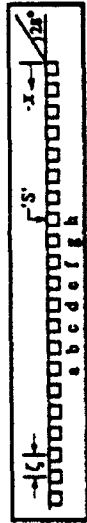
2-10: Mach 3 Blunt Fin Interaction Mean Wall Pressure Distributions, (a) Experimental (Dolling and Bogdonoff 1982) and (b) Experimental and Computational (Hung and Buning 1985)



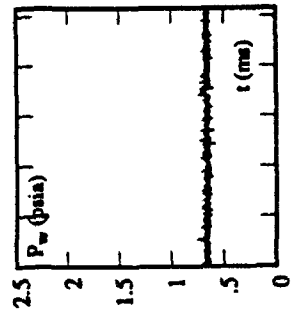
2-11: (a-c) Mach 3 Blunt Fin Interaction Leading Edge Mean Pressure Distributions (Dolling and Bogdonoff 1982)



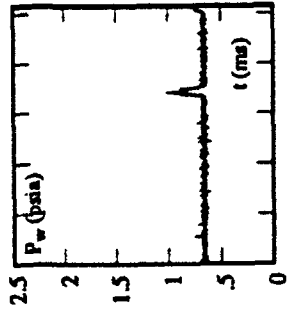
2-12: Mach 3 Blunt Fin Interaction (a) Experimental and Computational Leading Edge Mean Pressure Distributions, and (b) Particle Flow Paths on Centerline (Hung and Buning 1985)



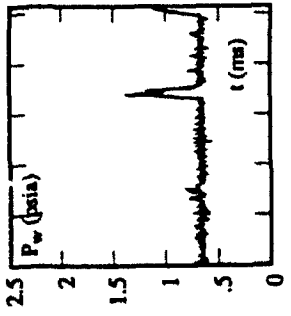
a) $X/\delta_1 = -2.51$



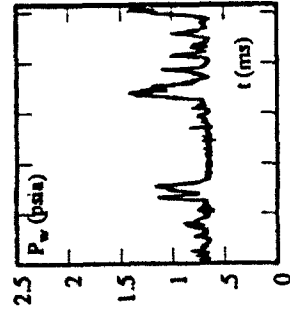
b) $X/\delta_1 = -2.35$



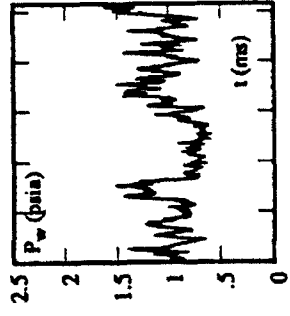
c) $X/\delta_1 = -2.19$



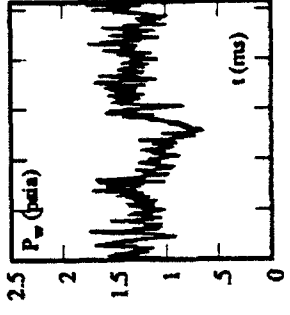
d) $X/\delta_1 = -2.02$



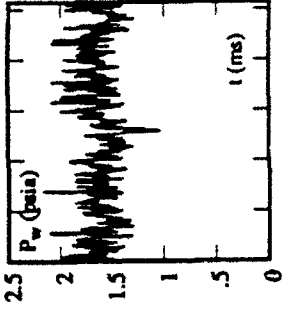
e) $X/\delta_1 = -1.86$



f) $X/\delta_1 = -1.69$

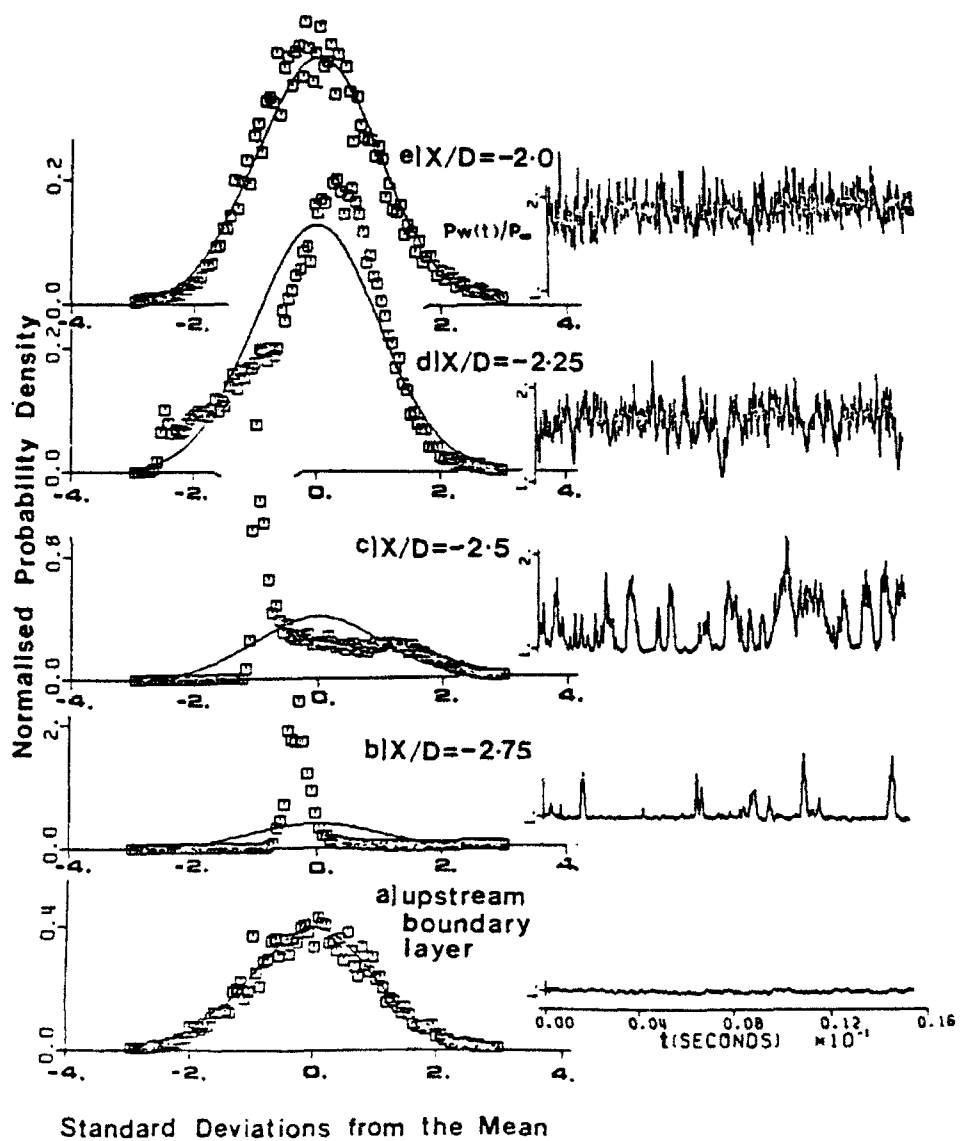


g) $X/\delta_1 = -1.53$

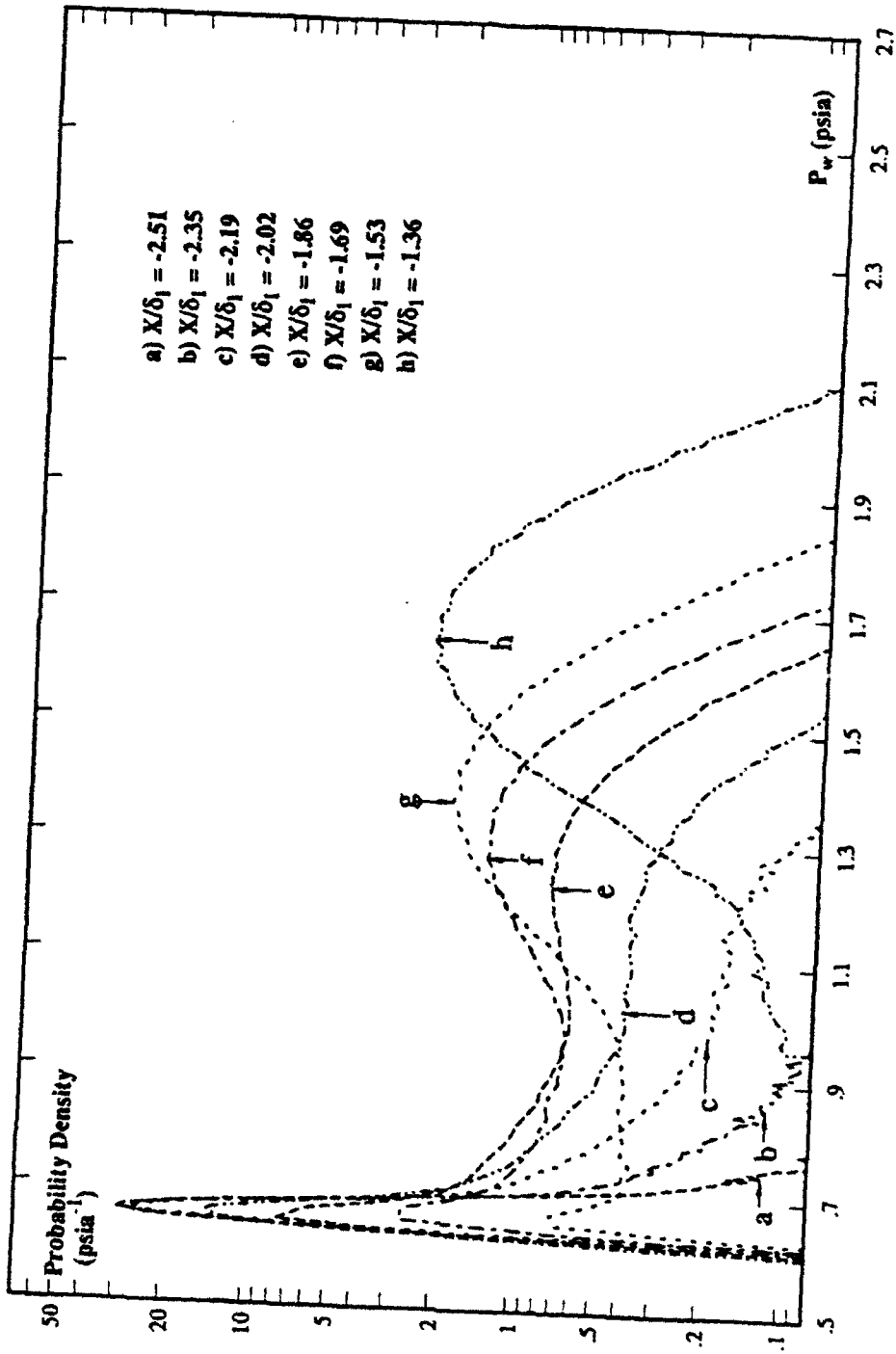


h) $X/\delta_1 = -1.36$

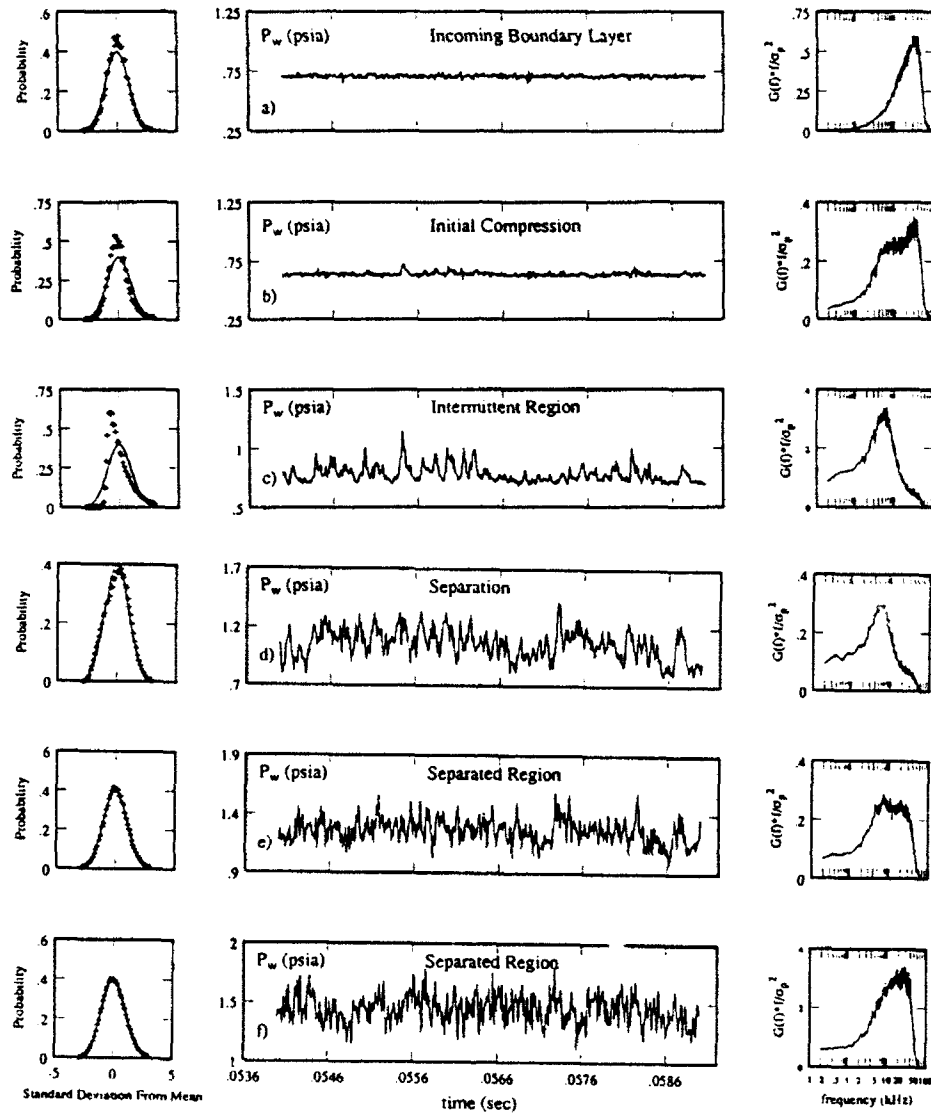
2-13: (a-h) Surface Pressure Signals Beneath the Translating Separation Shock Upstream of a Compression Corner, Mach 5, $\alpha = 17.5^\circ$ (McClure 1992)



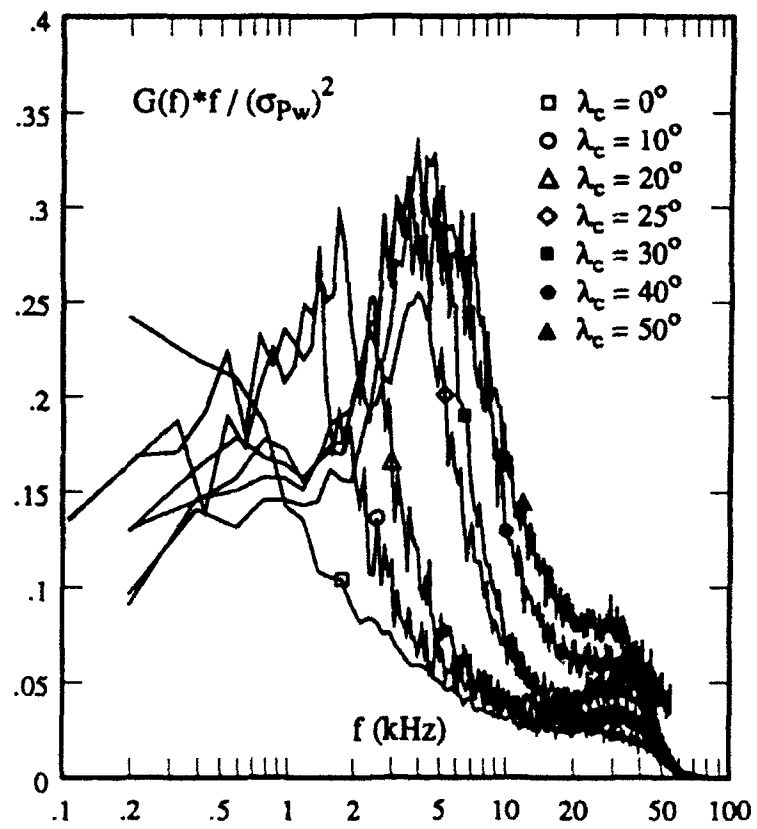
2-14: (a-e) Wall Intermittent Pressure Signals and Probability Density Distributions from a Mach 3 Blunt Fin Interaction (Dolling and Bogdonoff 1981)



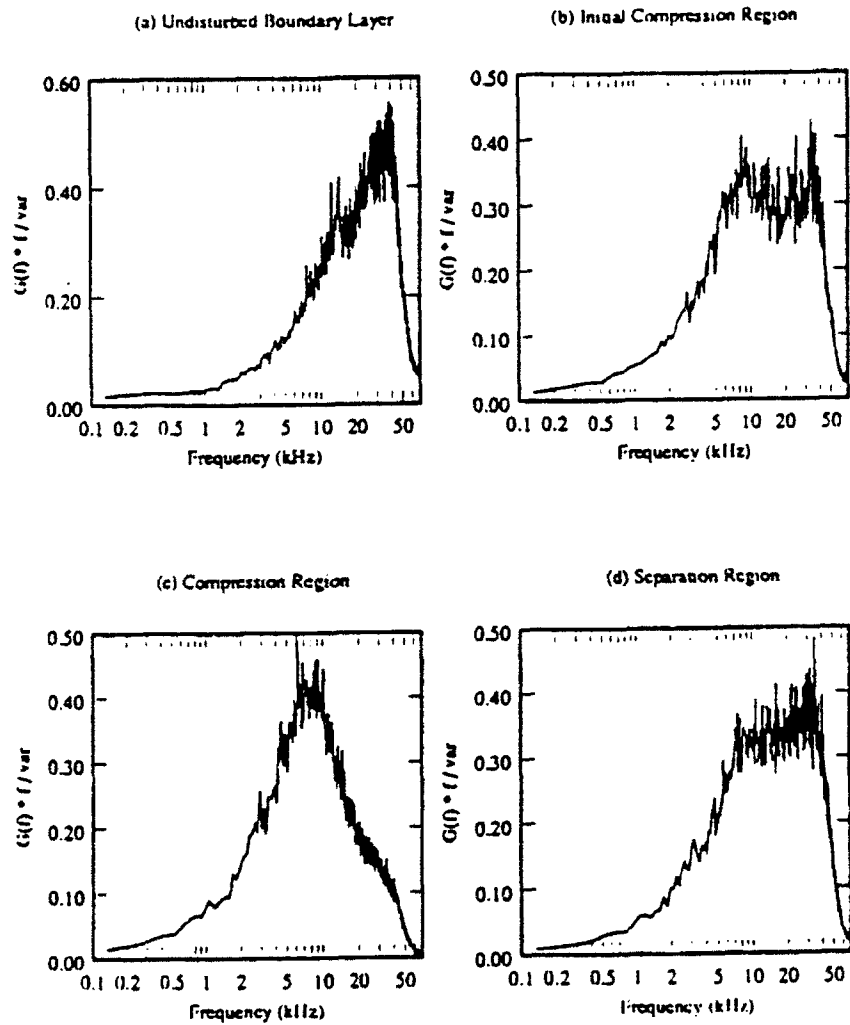
2-15: Surface Pressure Probability Density Distributions Upstream of a Compression Corner, Mach 5, $\alpha = 17.5^\circ$ (McClure 1992)



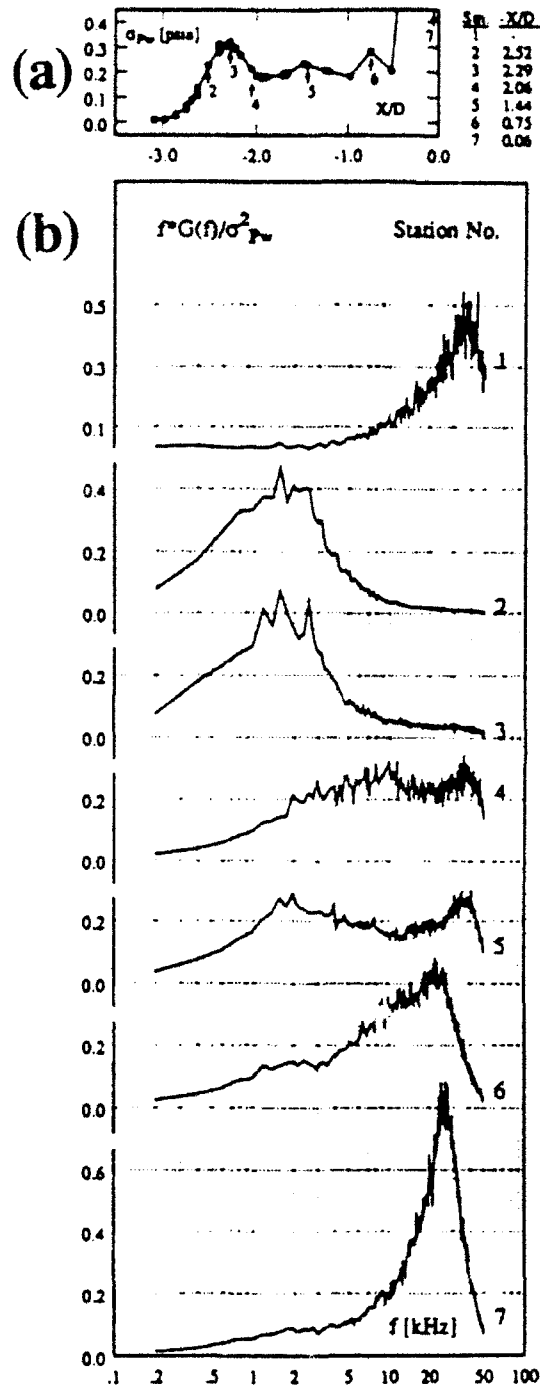
2-16: (a-f) Wall Pressure Signals, PDDs, and PSDs, Mach 5 Sharp Fin Interaction (Schmisser 1992)



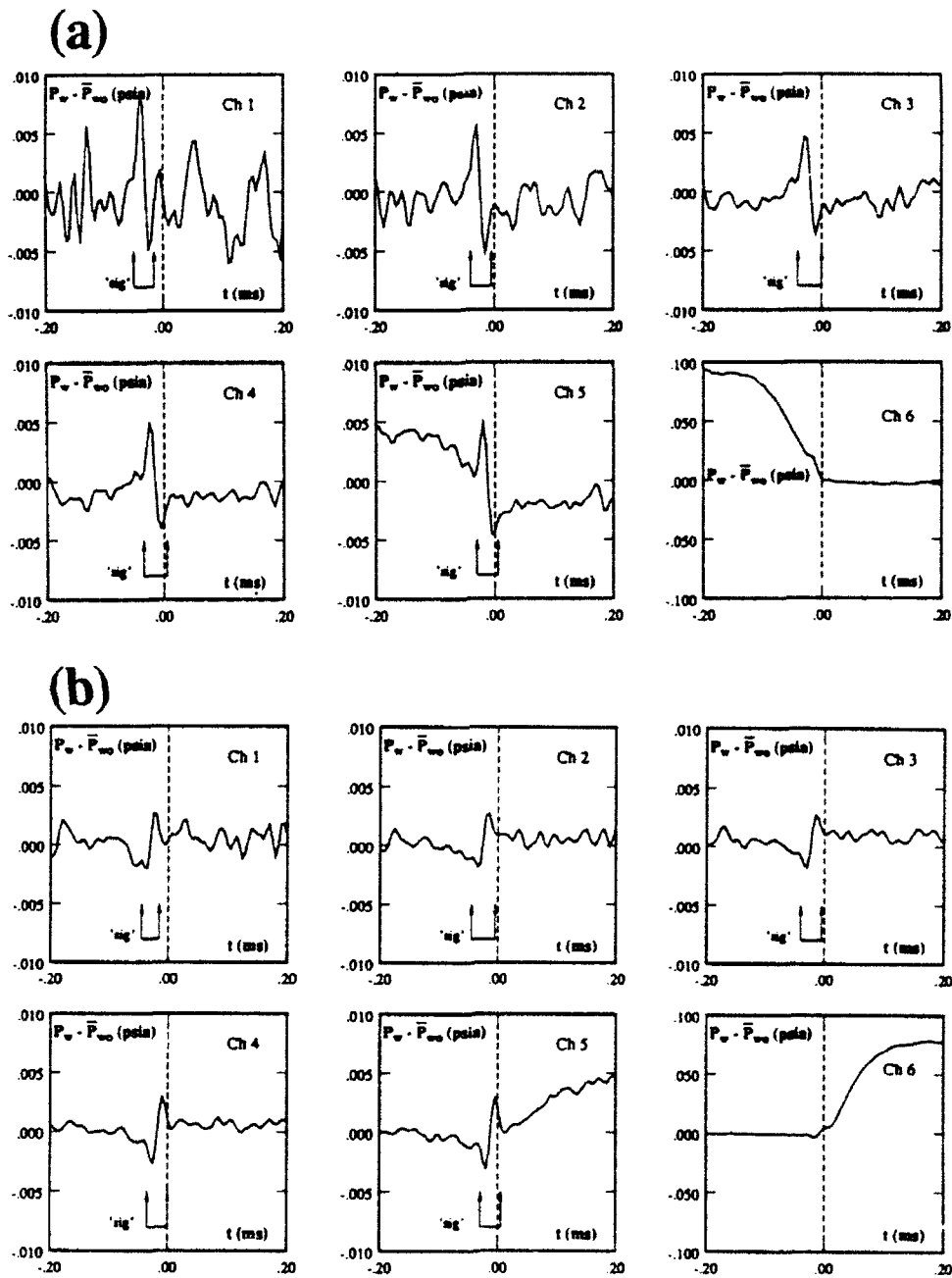
2-17: Effects of Interaction Sweep on PSDs, Mach 5 Compression Ramp Interactions (Erengil and Dolling 1993a)



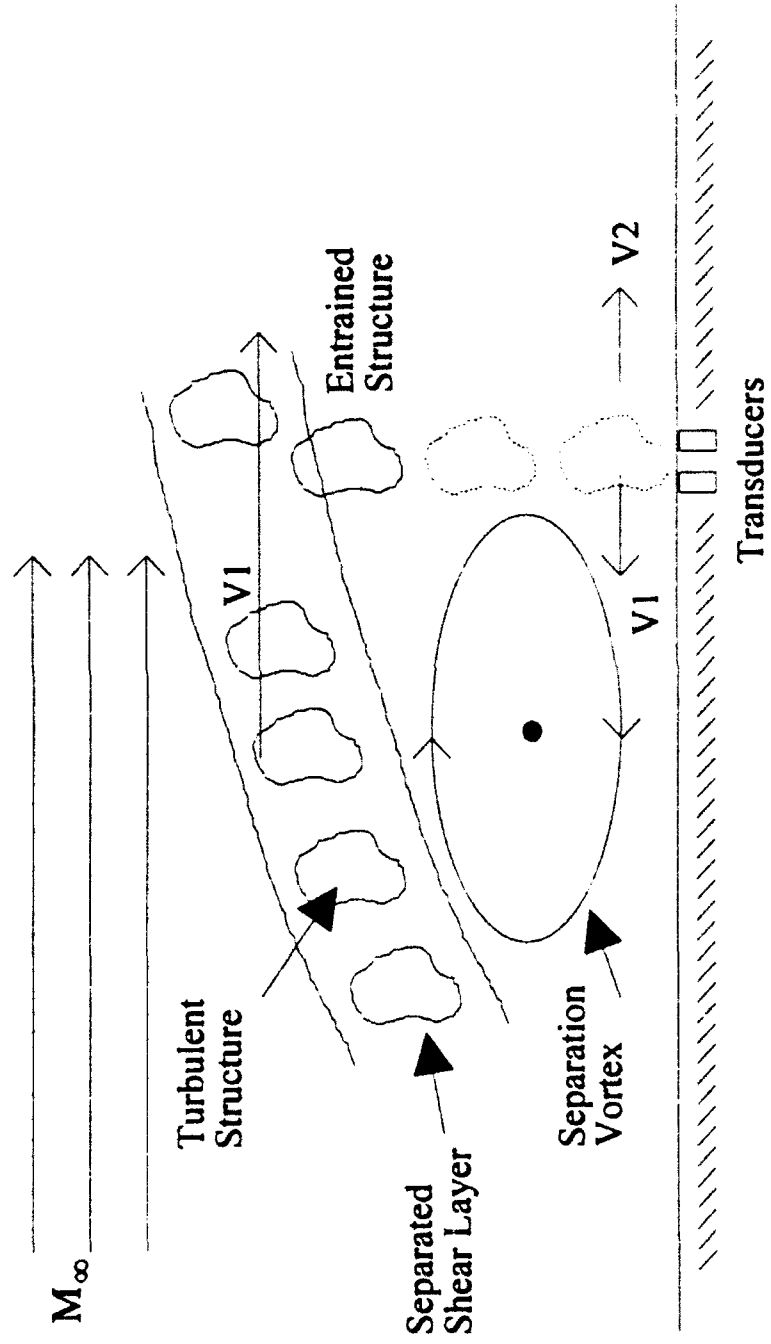
2-18: Sharp Fin Interaction PSDs, Mach 5, $\alpha = 18^\circ$ (Gibson 1990)



2-19: (a) RMS Pressure Distribution and (b) PSDs. Mach 5 Cylinder-Induced Interaction (Brusniak 1991)



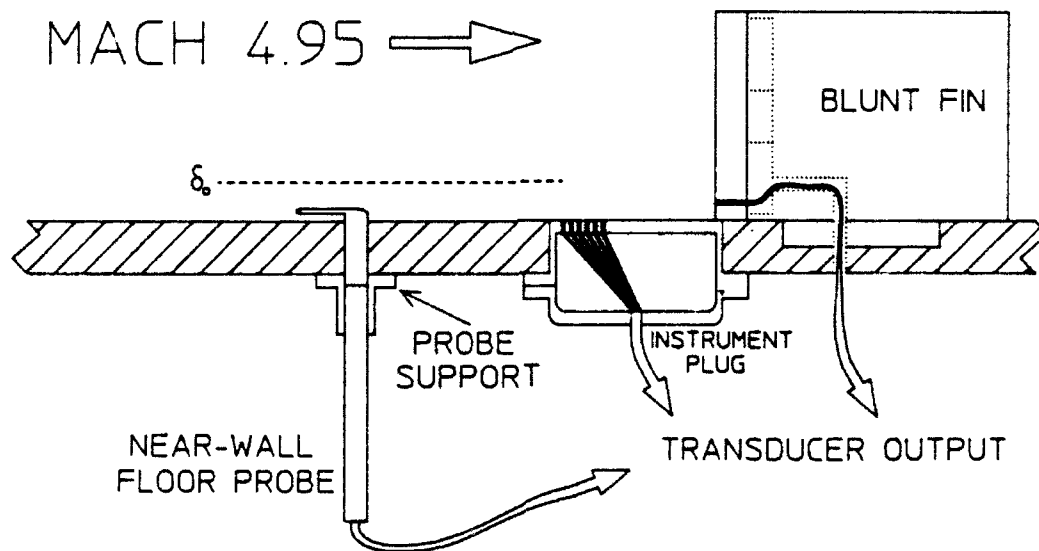
2-20: Mach 5, 28° Compression Ramp Ensemble-Averaged Wall Pressure Histories, 3-Channel (a) Downstream and (b) Upstream Sweeps (Trigger on Channel 7) (McClure 1992)



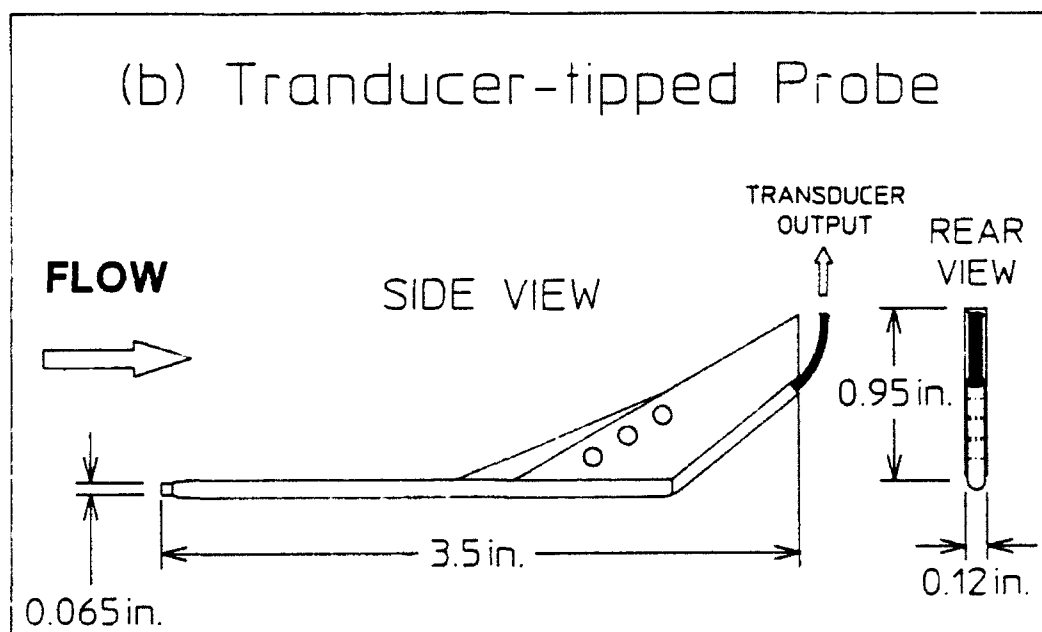
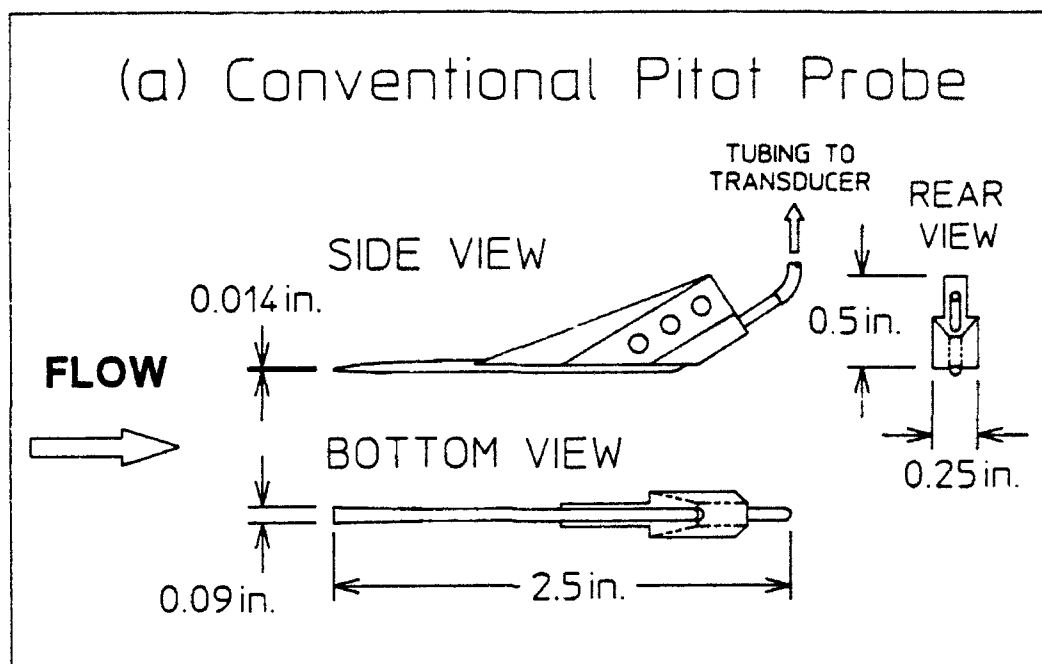
2-21: Qualitative Model of Fin-Induced Interaction Separated Region Recirculation (Kleifges 1993)

SIDE VIEW

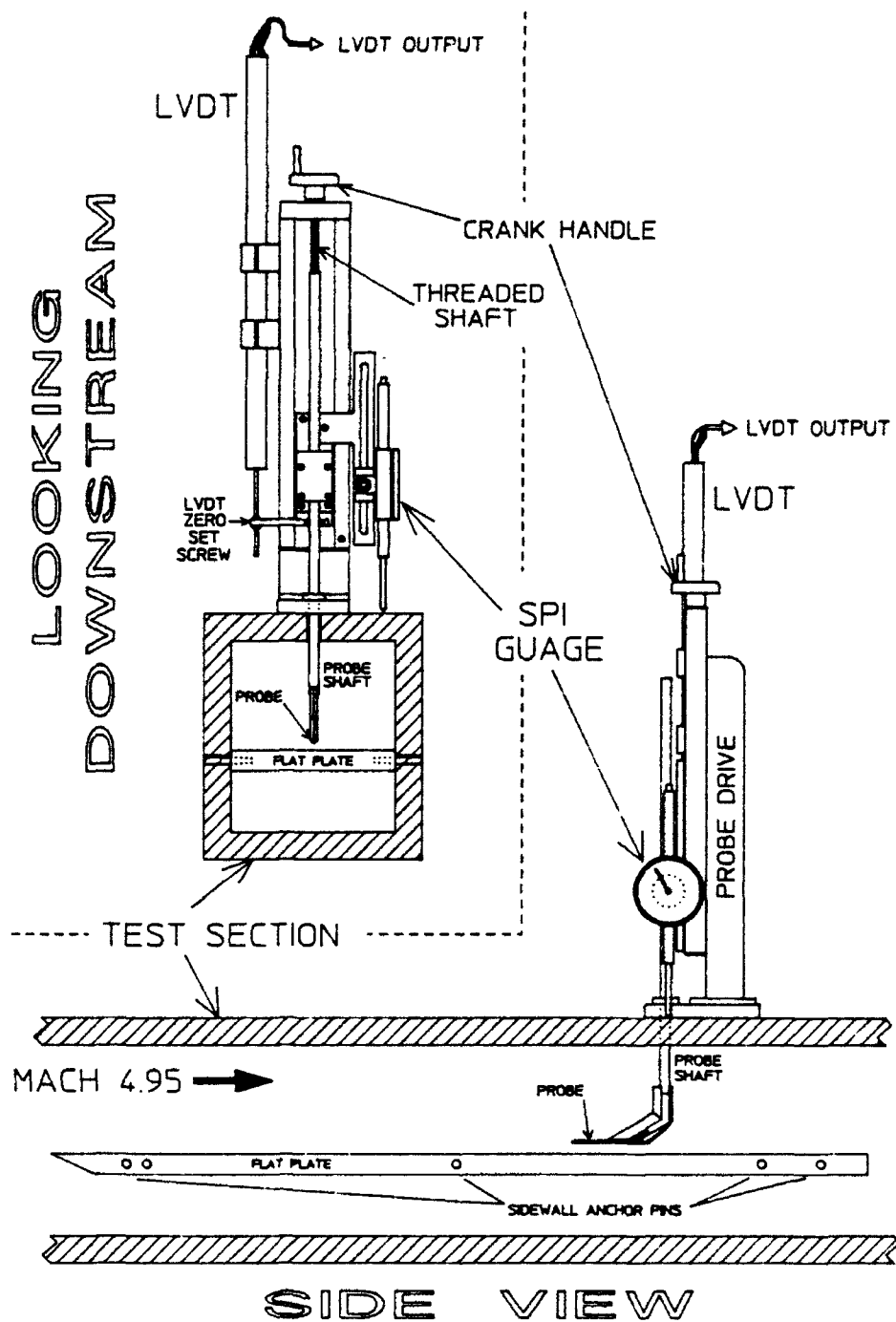
ON TUNNEL CENTERLINE



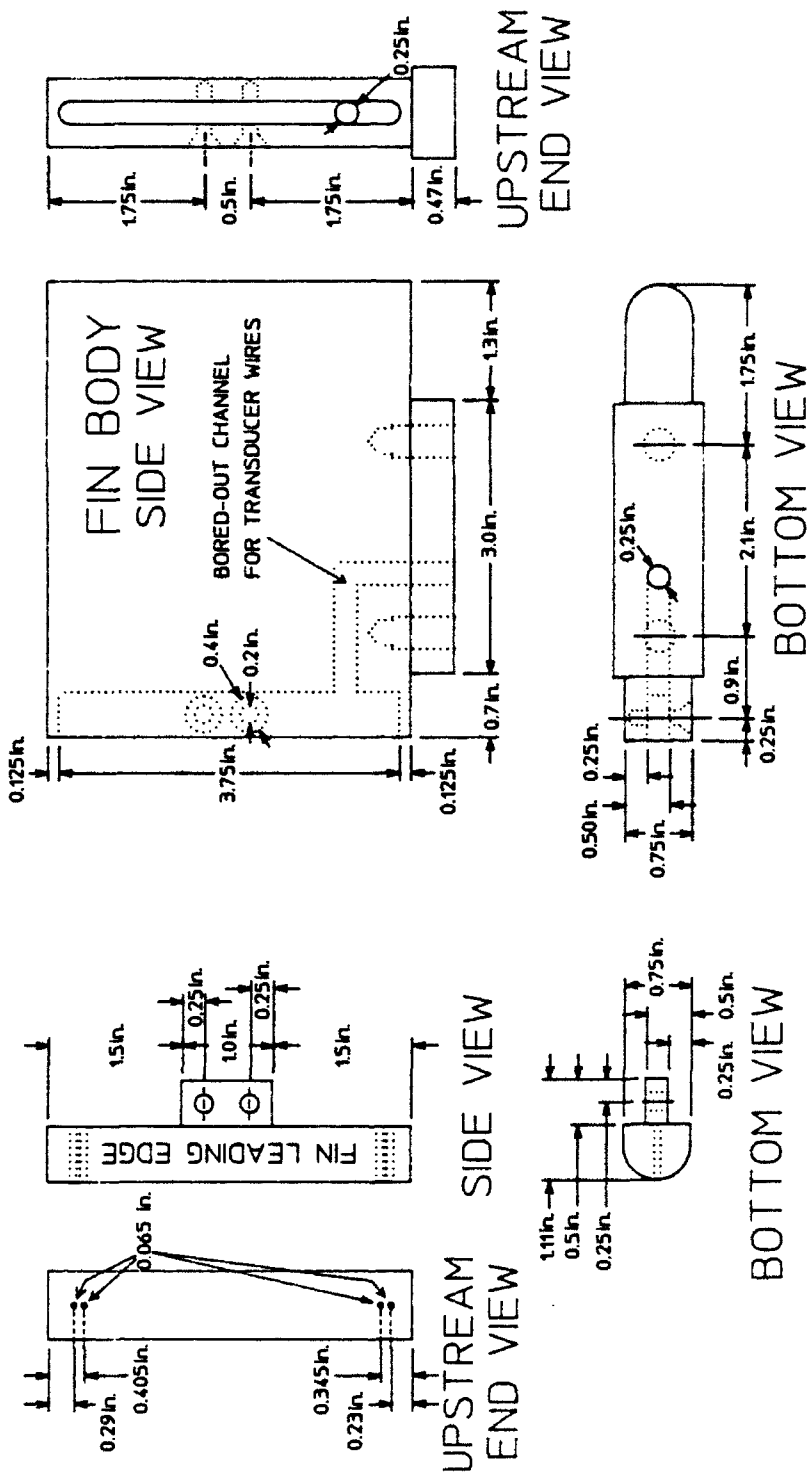
3-1: Phase 1 Test Setup



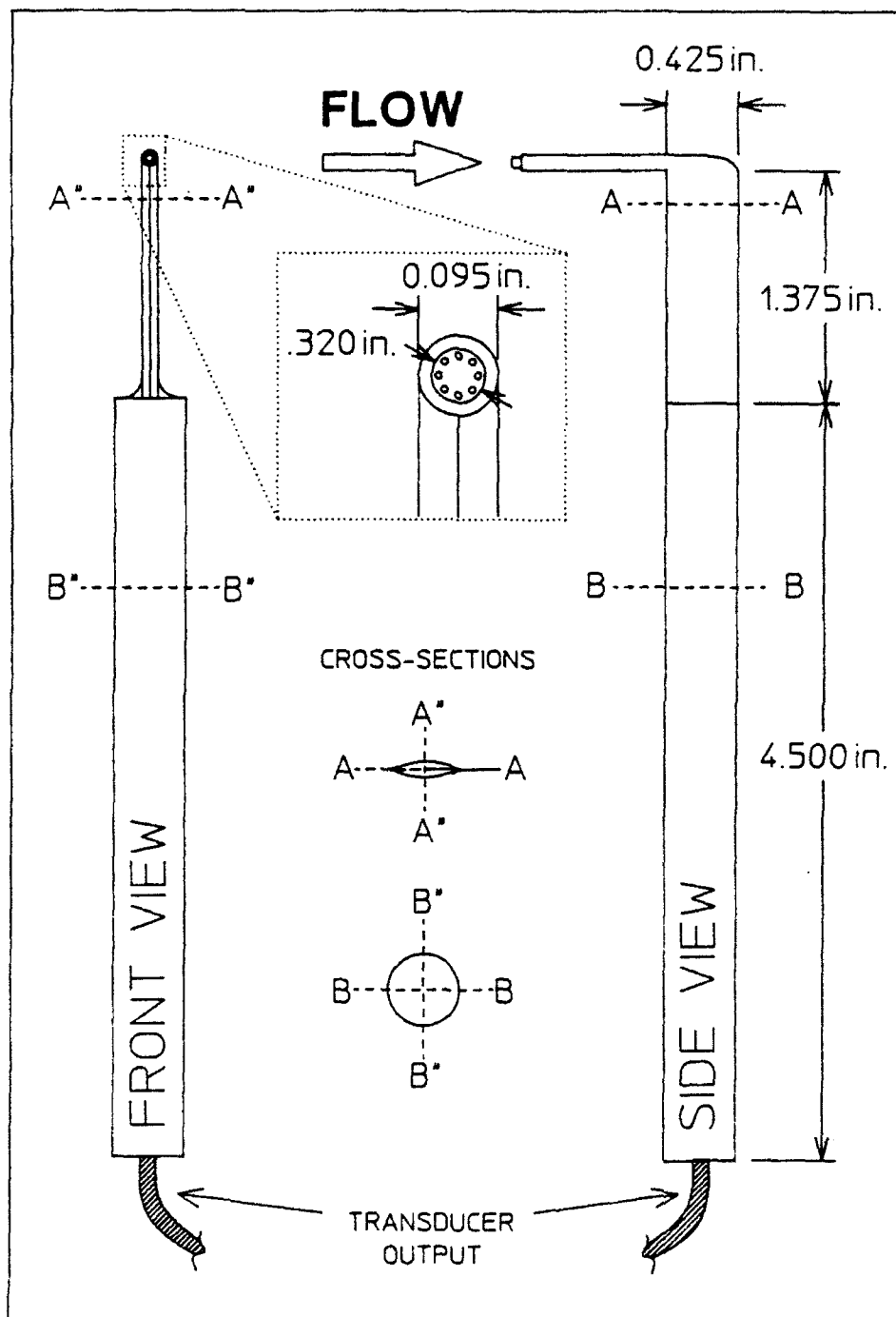
3-2: Pitot Probes



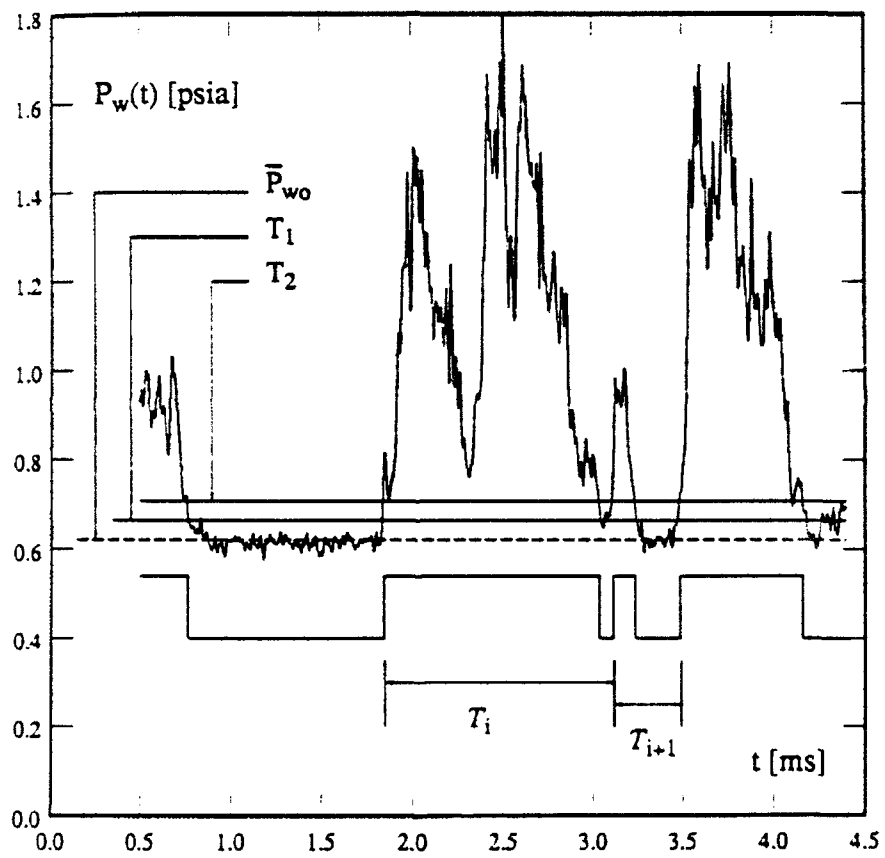
3-3: Phase 2 Test Setup



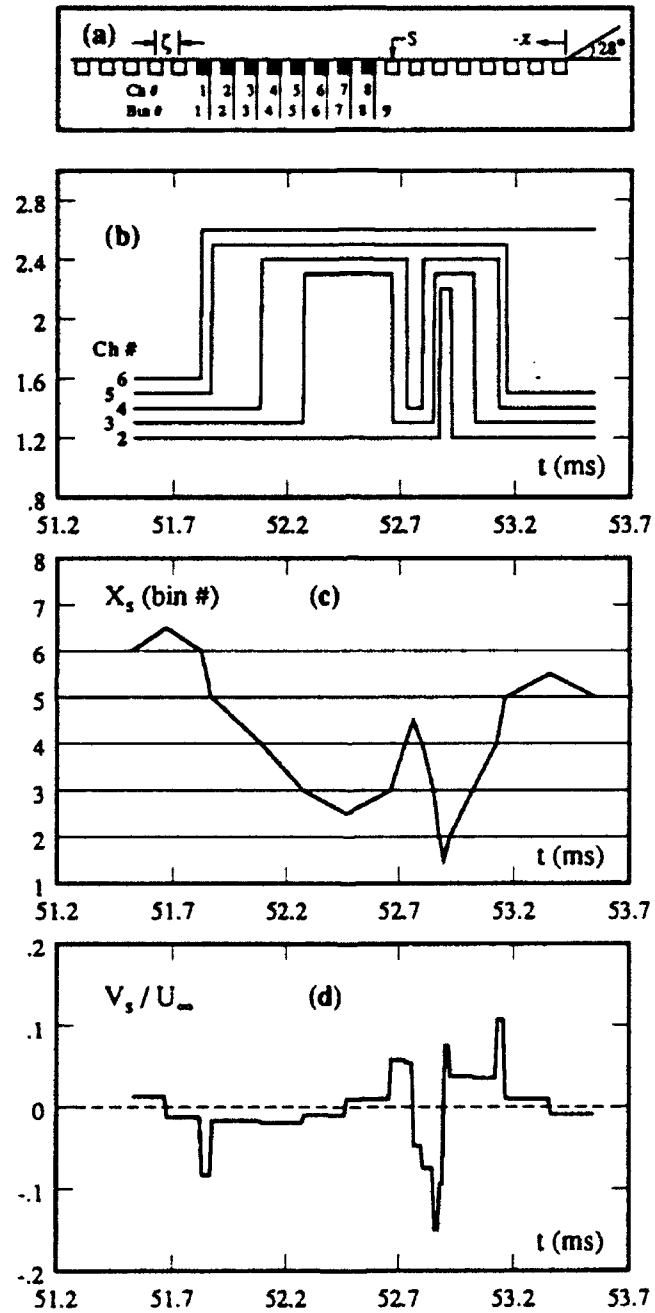
3-4: Blunt Fin Body and Instrumented Leading Edge



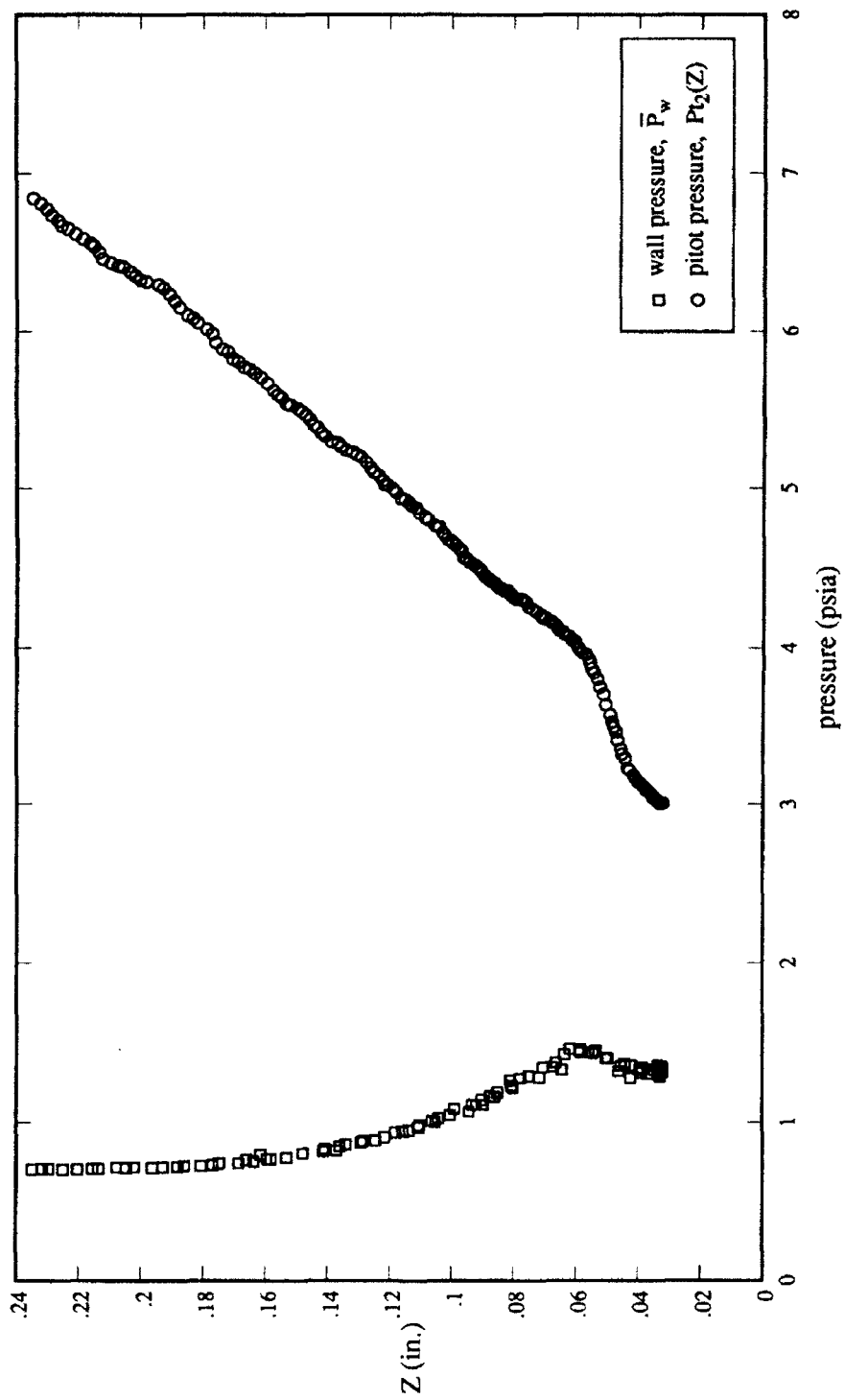
3-5: Near-Wall Boundary Layer Probe



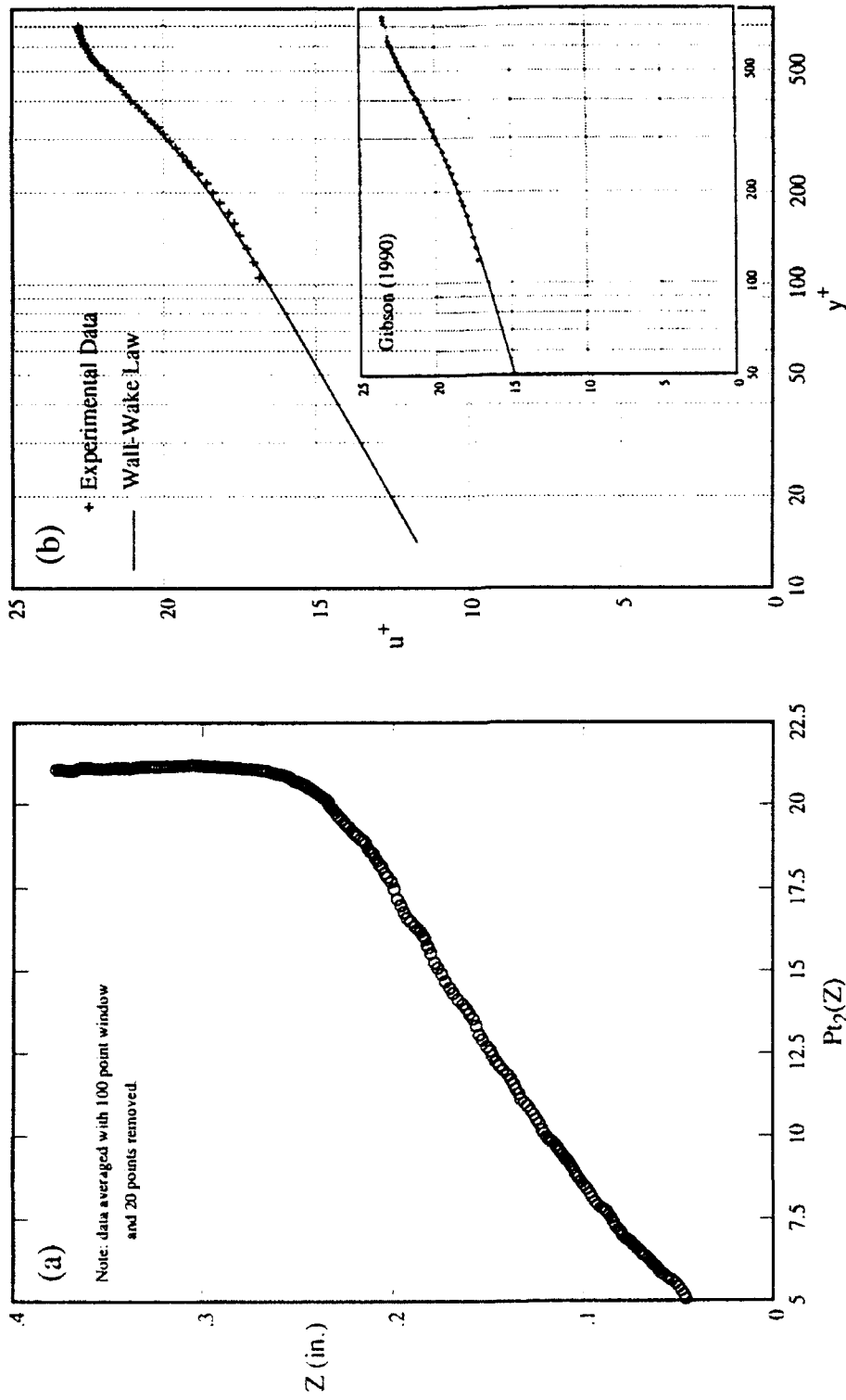
4-1: Two-Threshold Method (Erengil 1989)



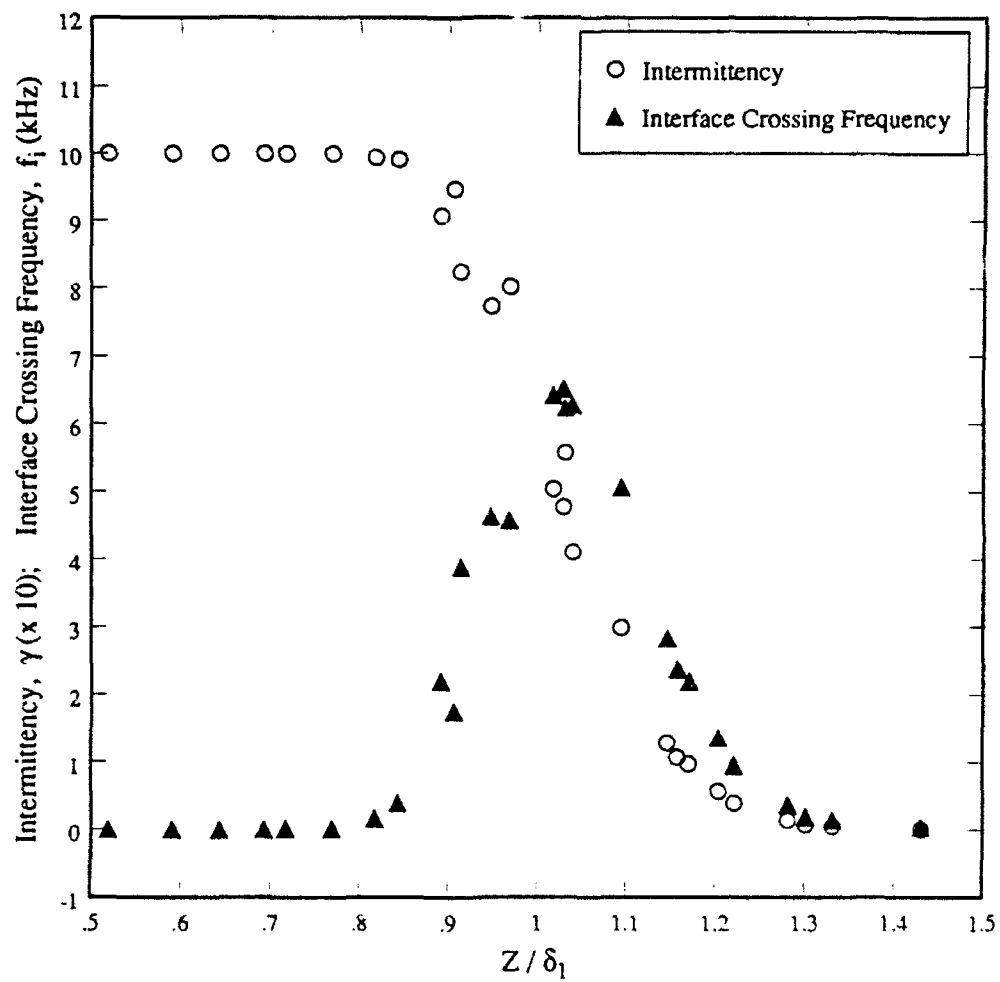
4-2: Determination of $X_s(t)$ and $V_s(t)$ from Nested Boxcar Signals (Erengil and Dolling 1993a)



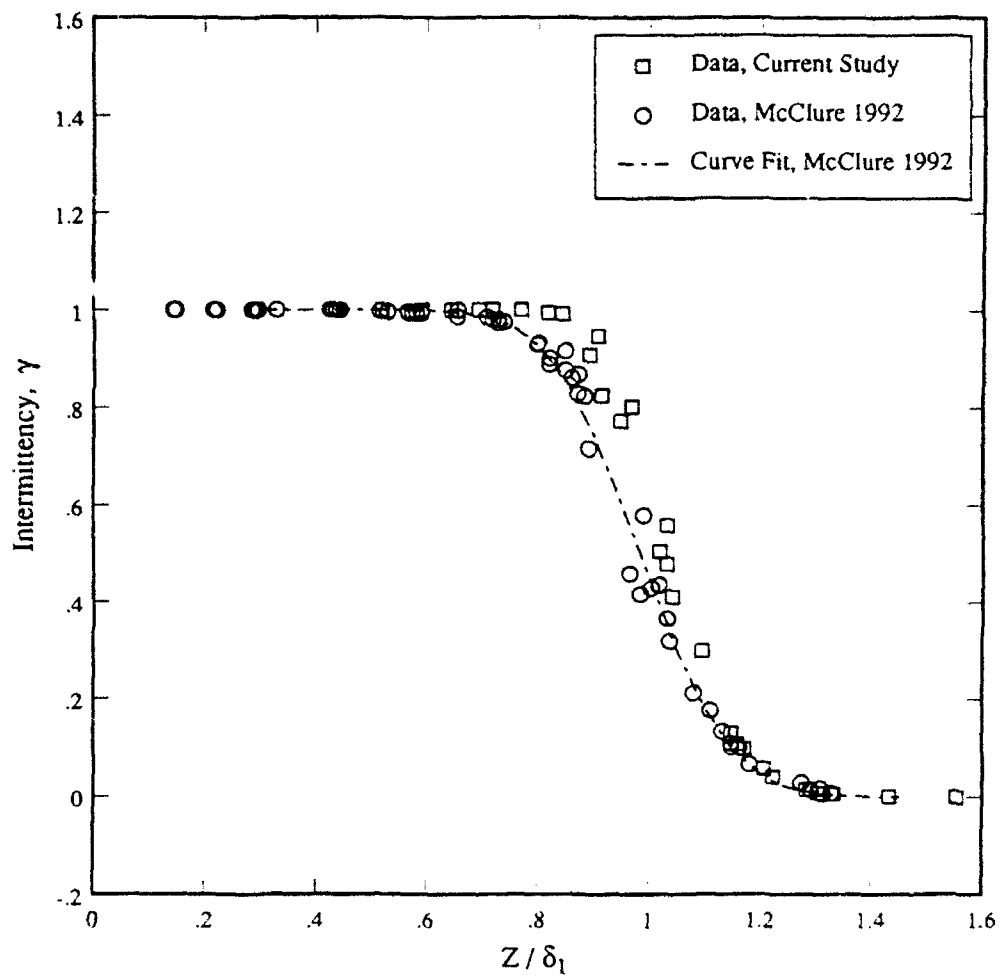
5-1: Probe Interference Effects on Wall Static Pressure and Pitot Pressure



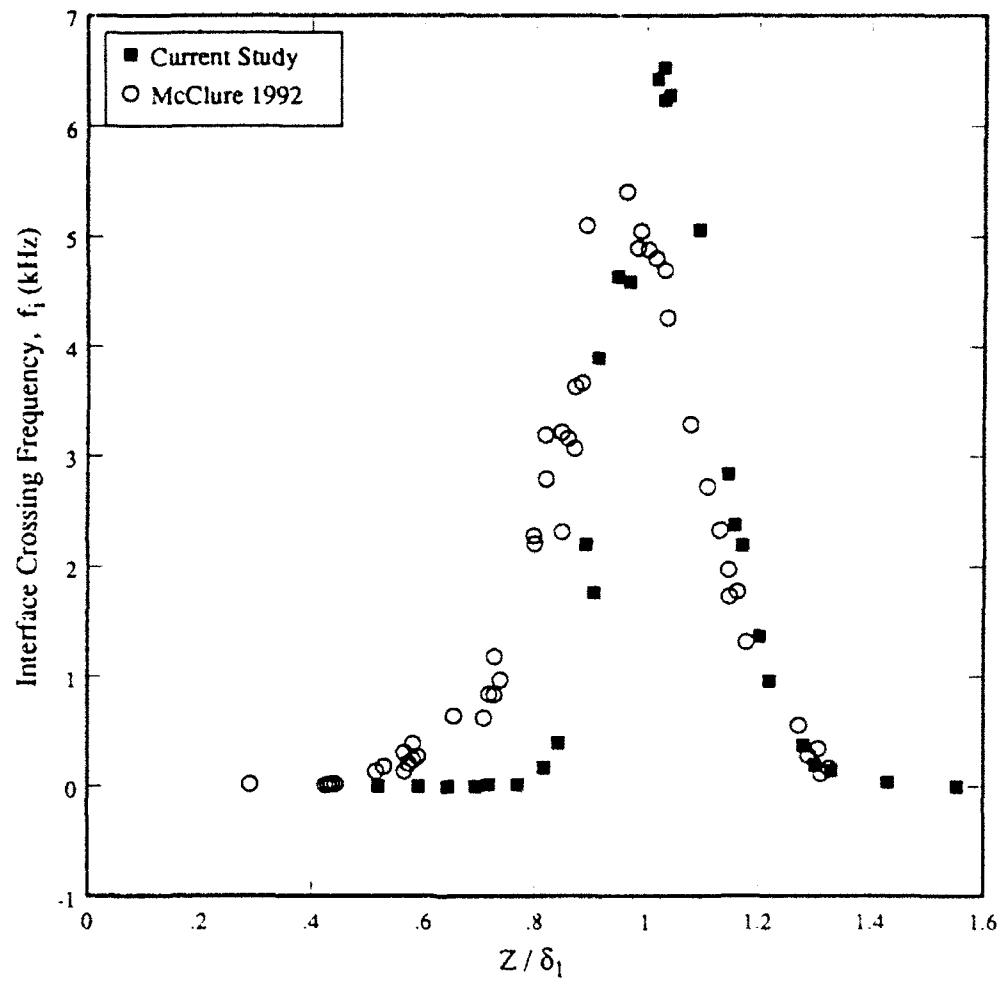
5-2: Boundary Layer (a) Pitot Pressure Profile and (b) u^+ , y^+ Velocity Profiles from the Current Study and Gibson (1990)



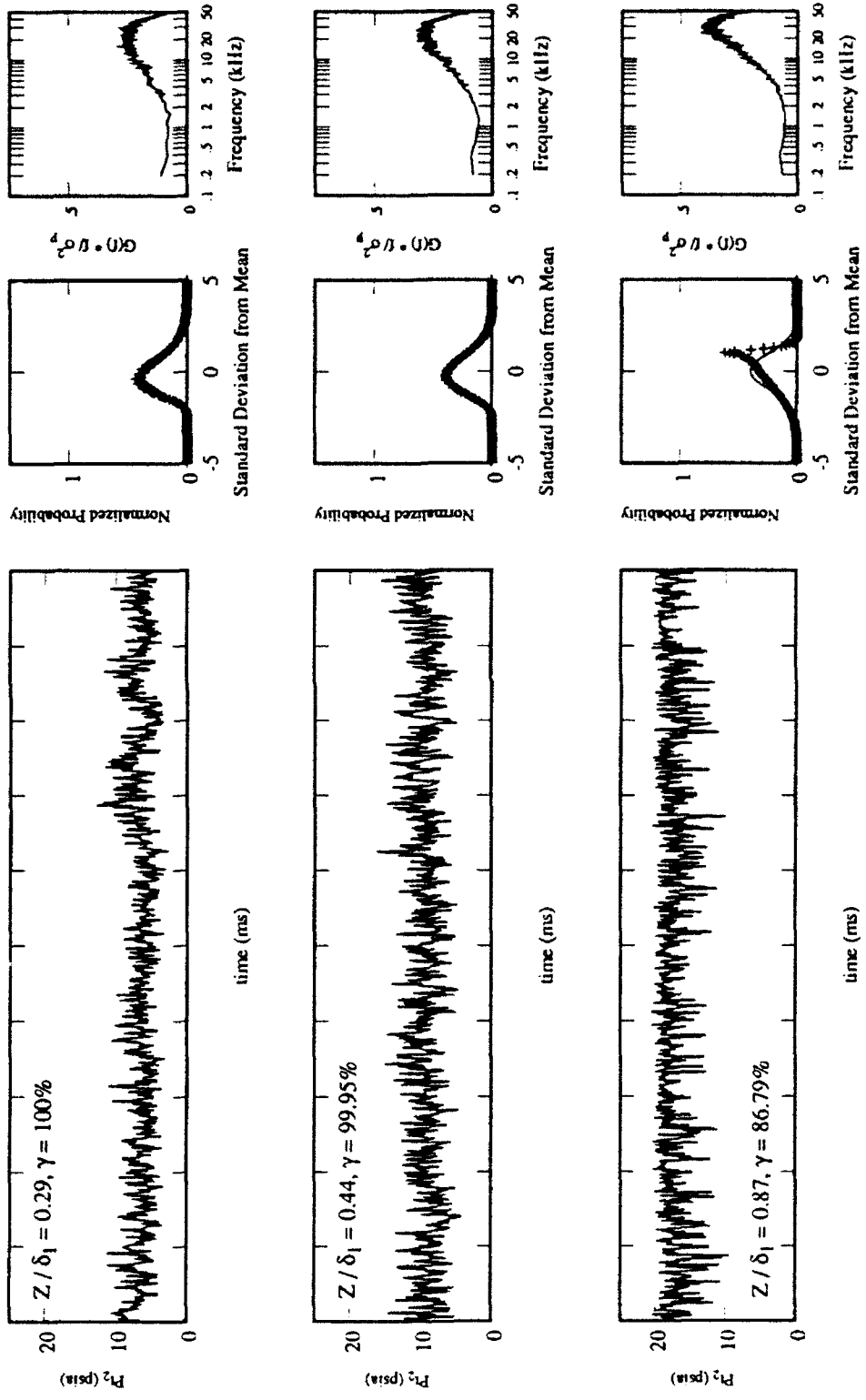
5-3: Boundary Layer / Freestream Intermittency and Interface Crossing Frequency Distributions



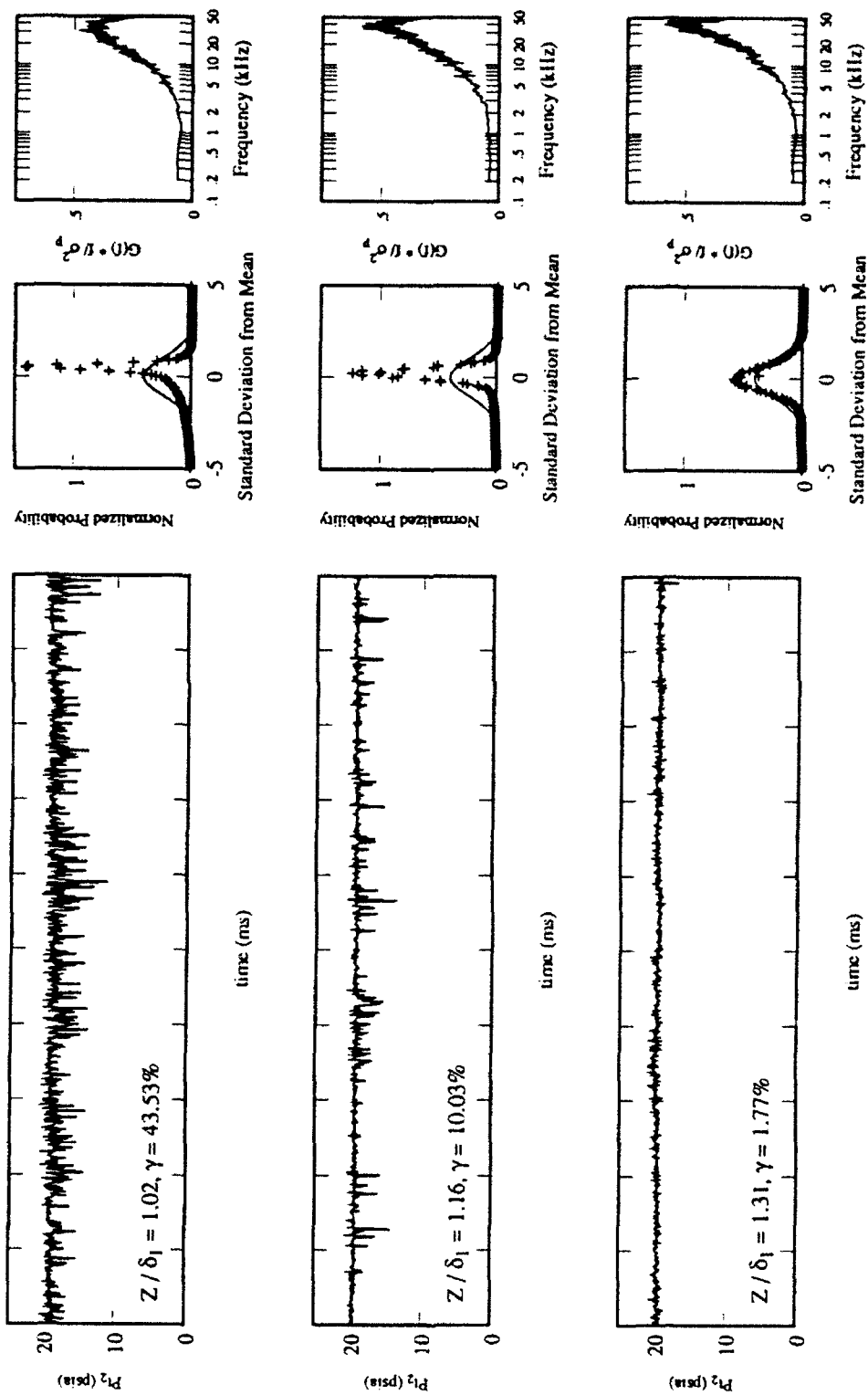
5-4: Boundary Layer / Freestream Intermittency Profile



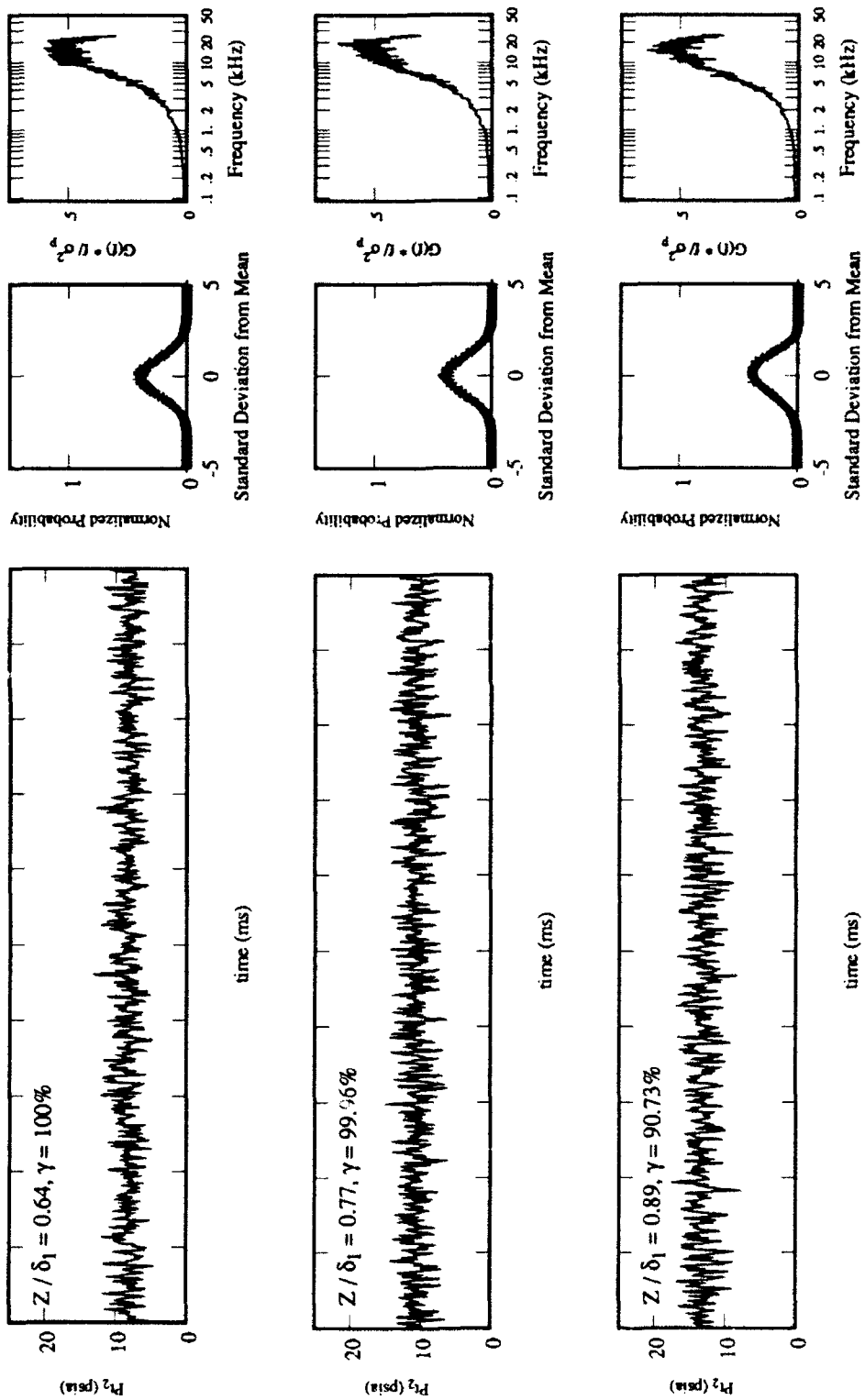
5-5: Boundary Layer / Freestream Interface Crossing Frequency Profile



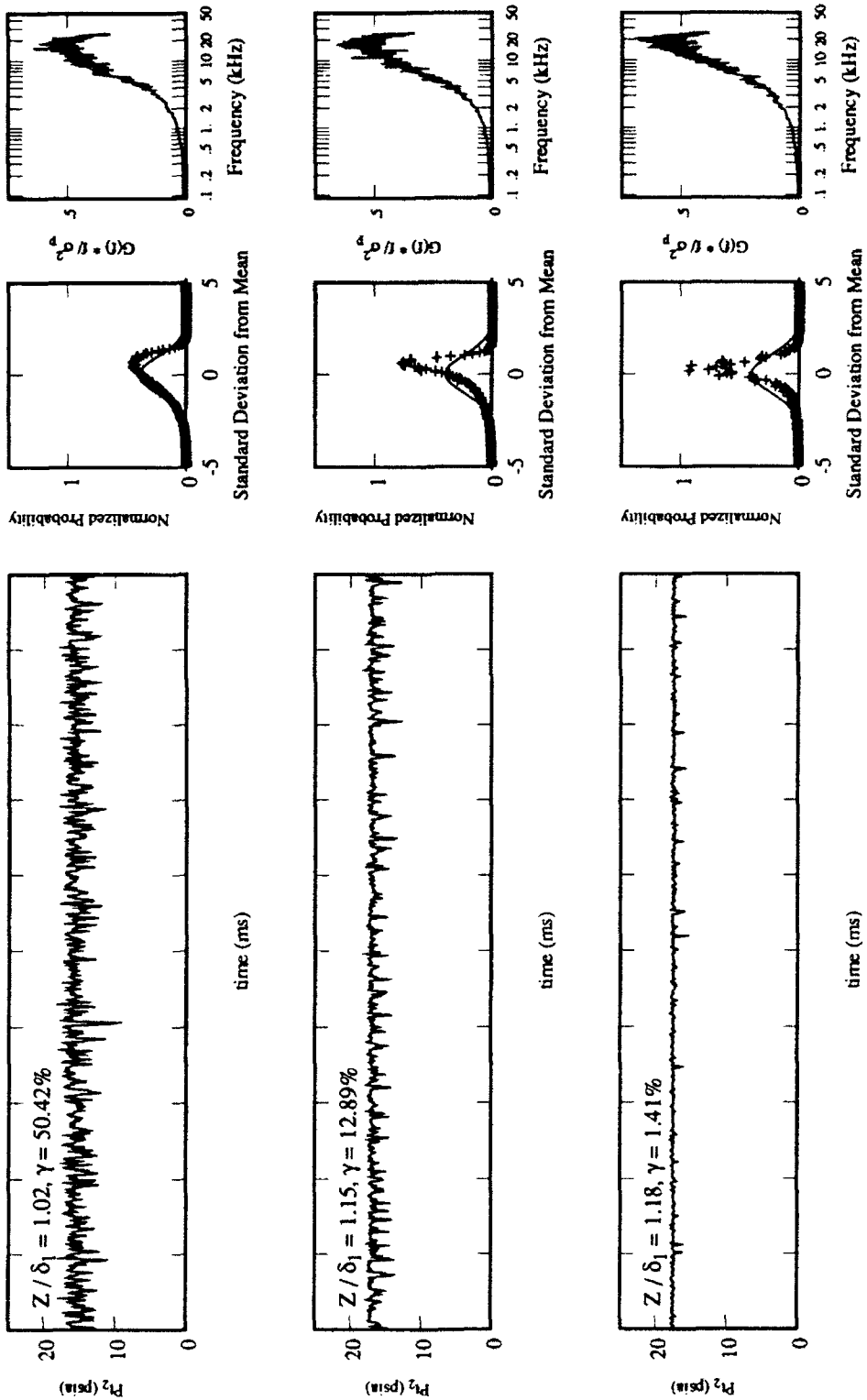
5-6: Turbulent Boundary Layer / Mach 5 Freestream Interface Region Raw Data Signals, PDDs, and PSDs (McClure 1992)



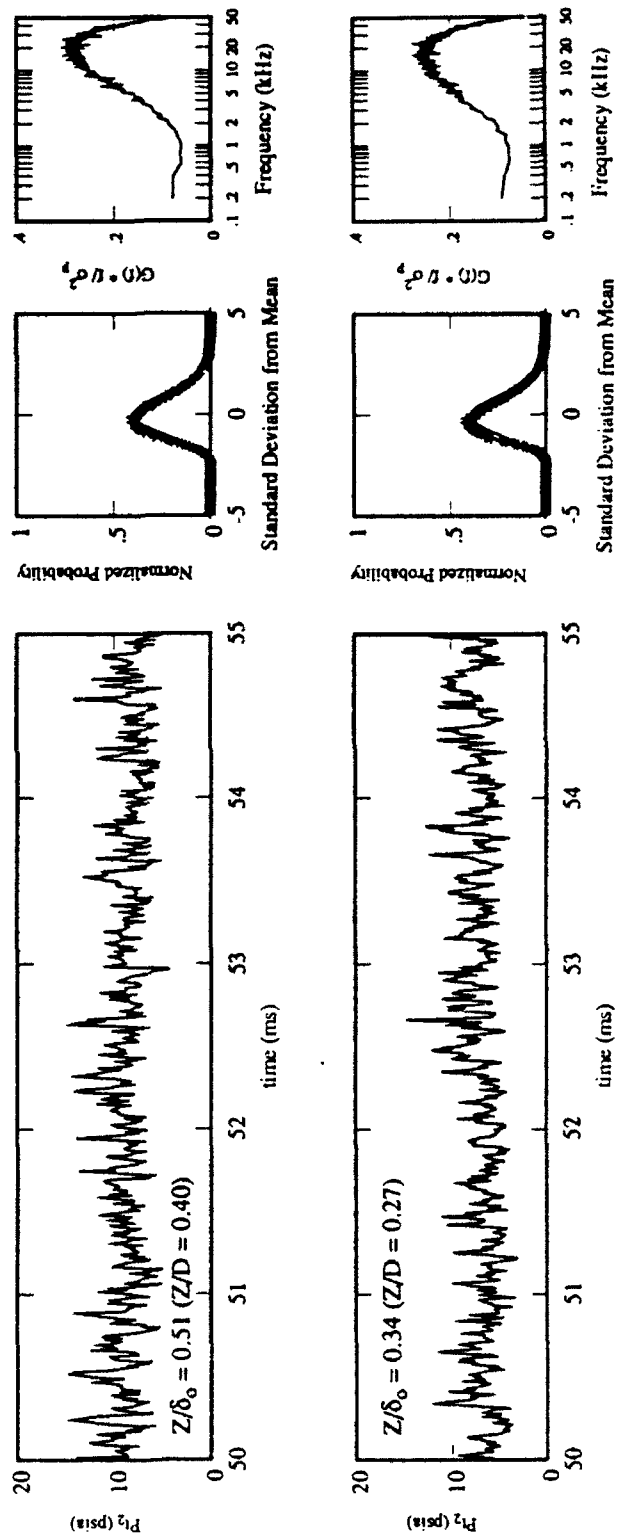
5-6 (continued): Turbulent Boundary Layer / Mach 5 Freestream Interface Region Raw Data Signals, PDDs, and PSDs
(McClure 1992)



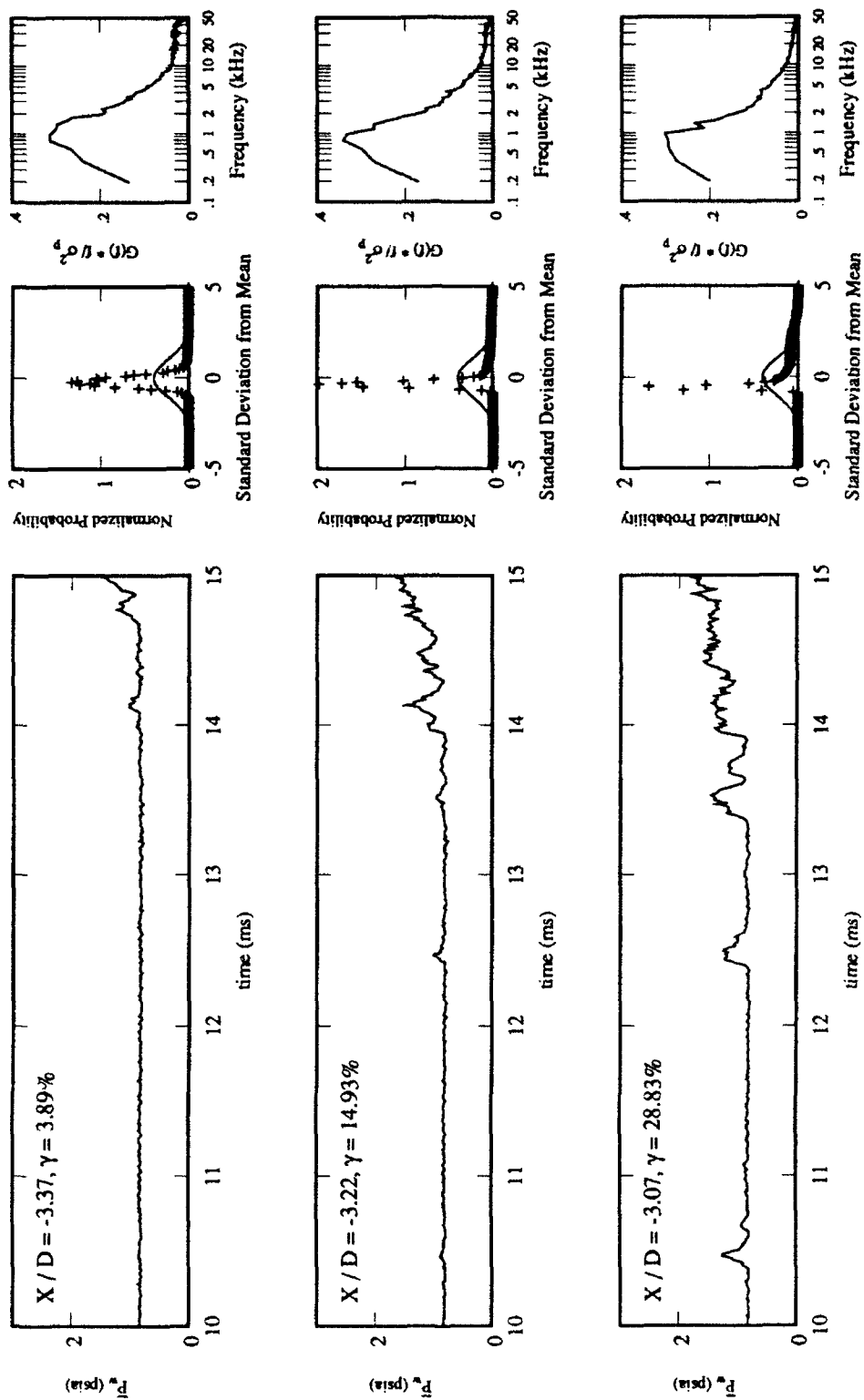
5-7: Turbulent Boundary Layer / Mach 5 Freestream Interface Region Raw Data Signals, PDDs, and PSDs



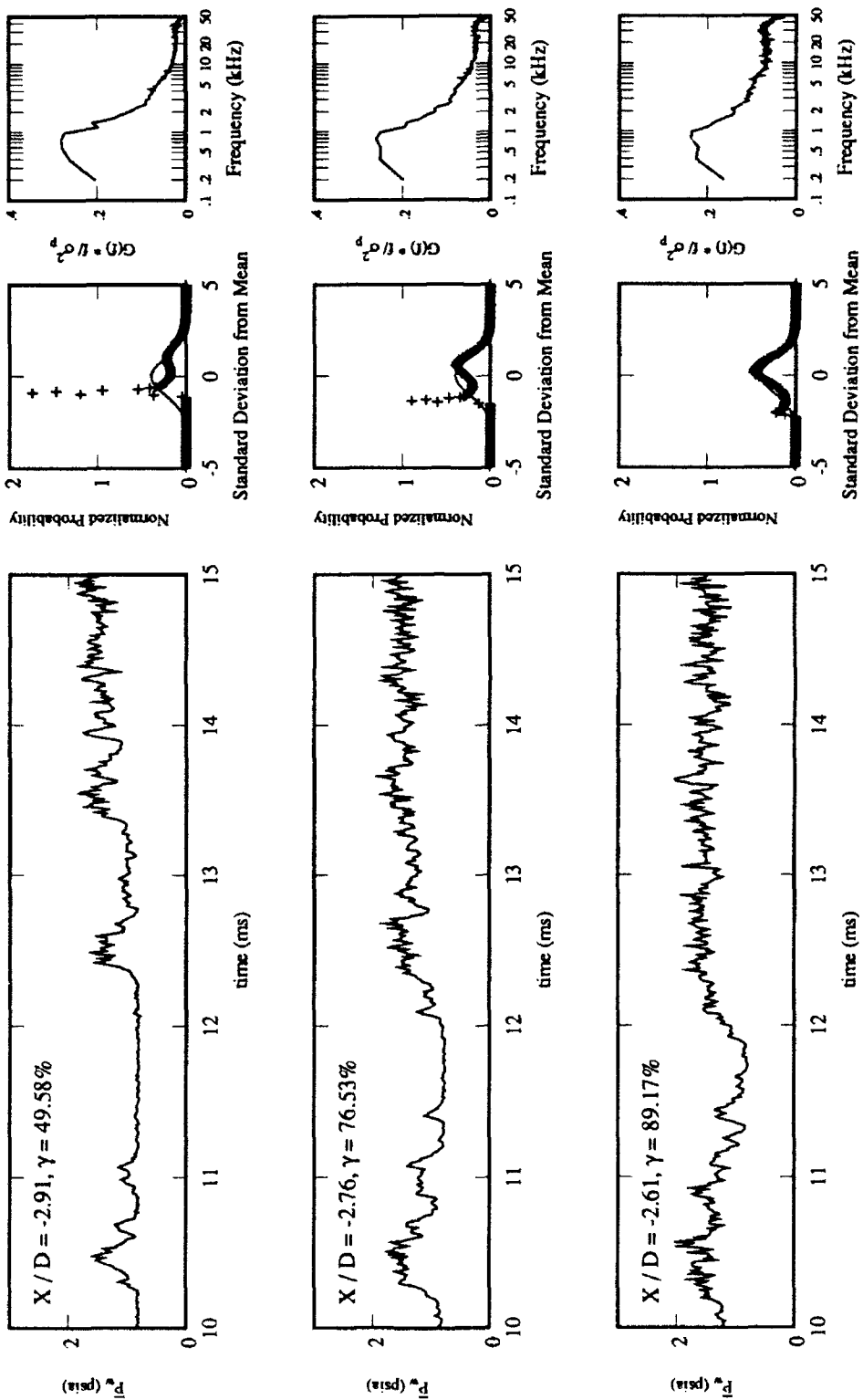
5-7 (continued): Turbulent Boundary Layer / Mach 5 Freestream Interface Region Raw Data Signals, PDDs, and PSDs



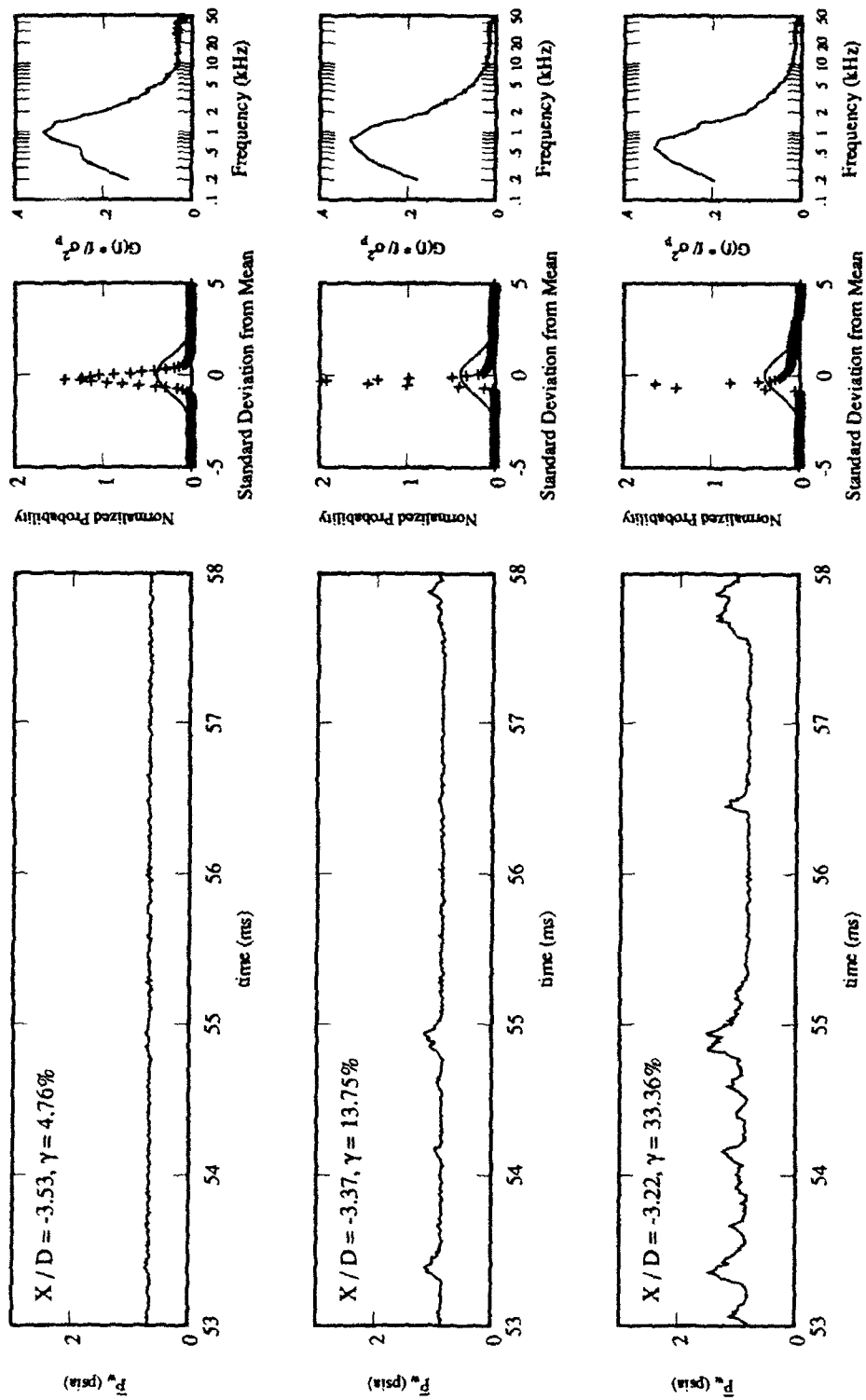
5-8: Pitot Probe Raw Data Signals, PDDs, and PSDs; $X/D = -10.73$ ($X/\delta_0 = 13.64$)



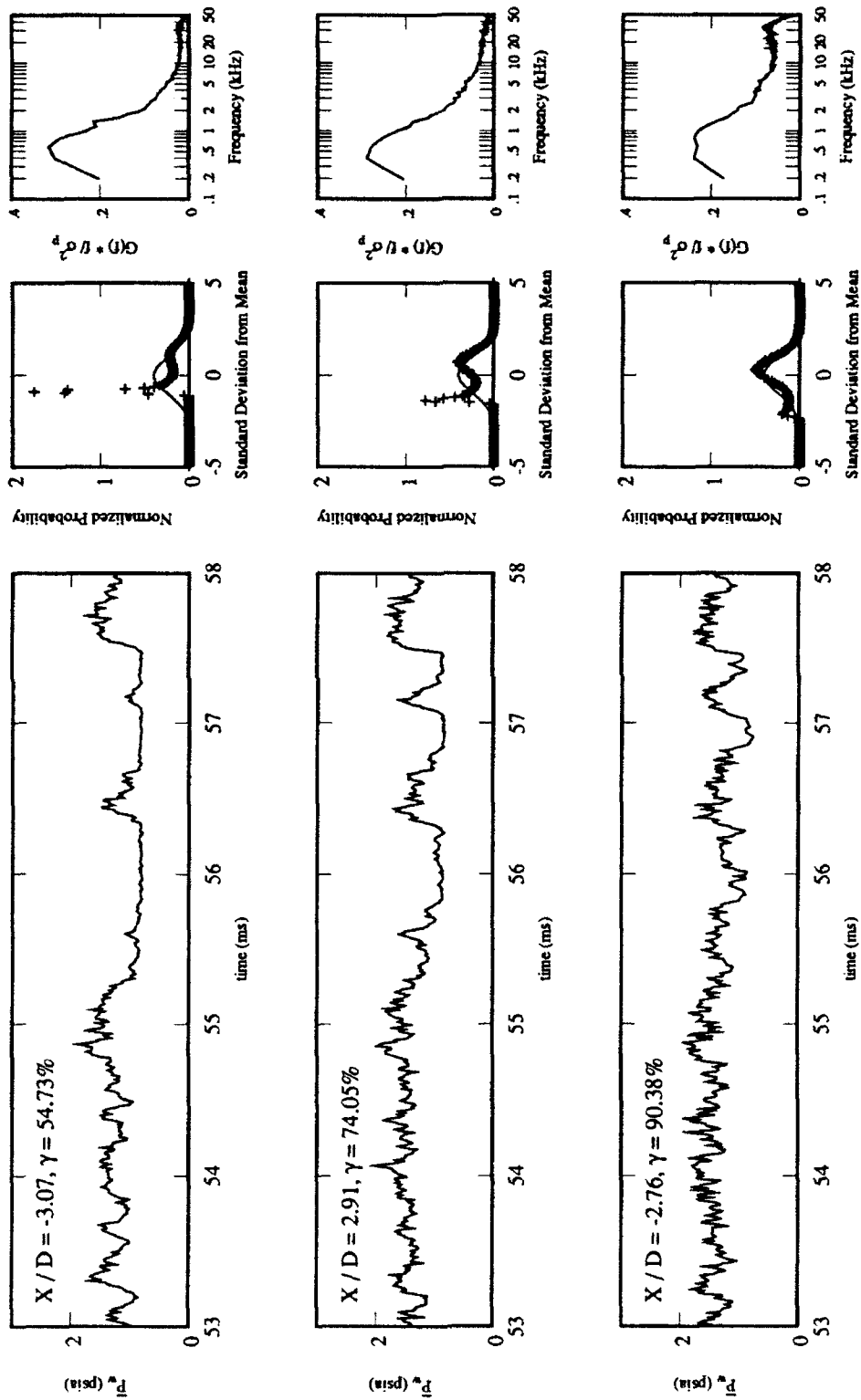
5-9: Intermittent Region Raw Data Signals, PDDs, and PSDs; No Upstream Probe



5-9 (continued): Intermittent Region Raw Data Signals, PDDs, and PSDs; No Upstream Probe

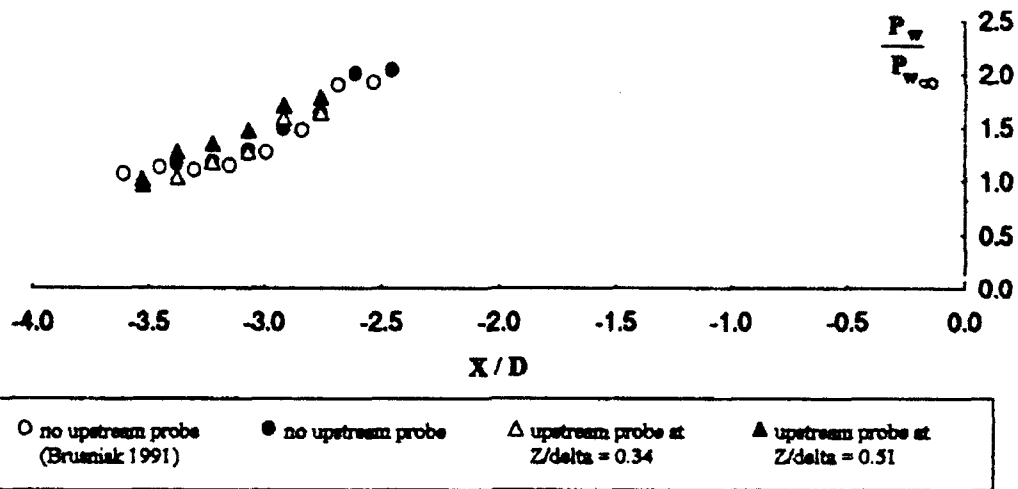


5-10: Intermittent Region Raw Data Signals, PDDs, and PSDs; Upstream Probe at $X/D = -10.73$, $Z/\delta_0 = 0.51$

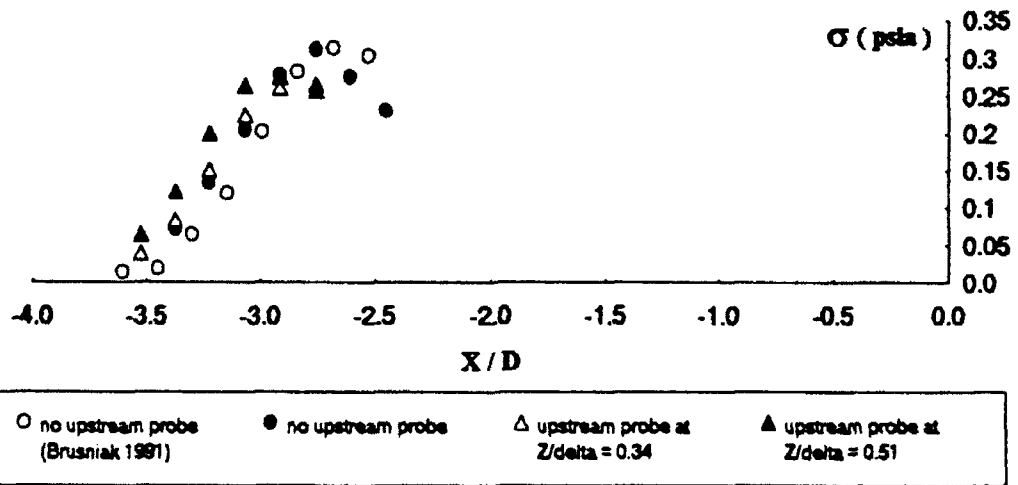


5-10 (continued): Intermittent Region Raw Data Signals, PDDs, and PSDs; Upstream Probe at $X/D = 10.73, Z/\delta_0 = 0.51$

Mean Pressure Distribution

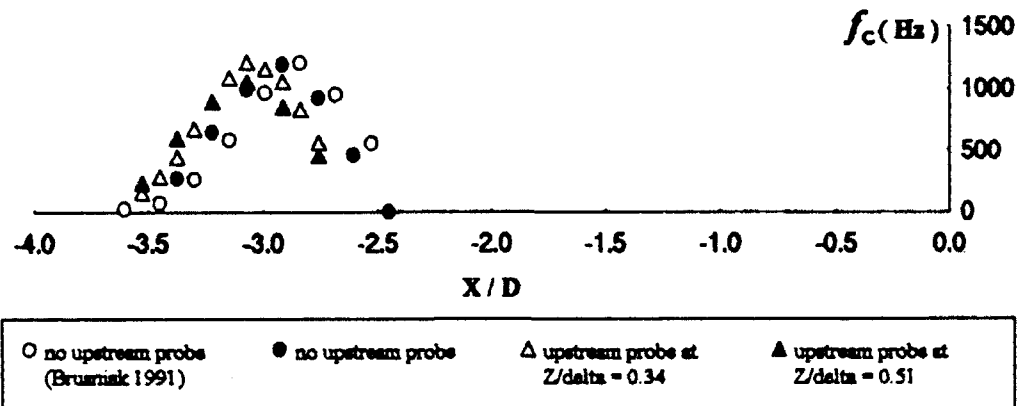


RMS Pressure Distribution

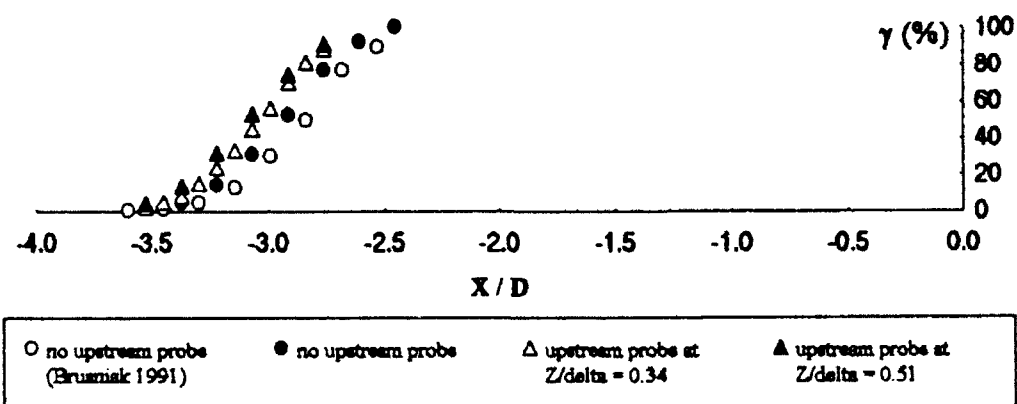


5-11: Blunt Fin Interaction Intermittent Region Pressure Distributions

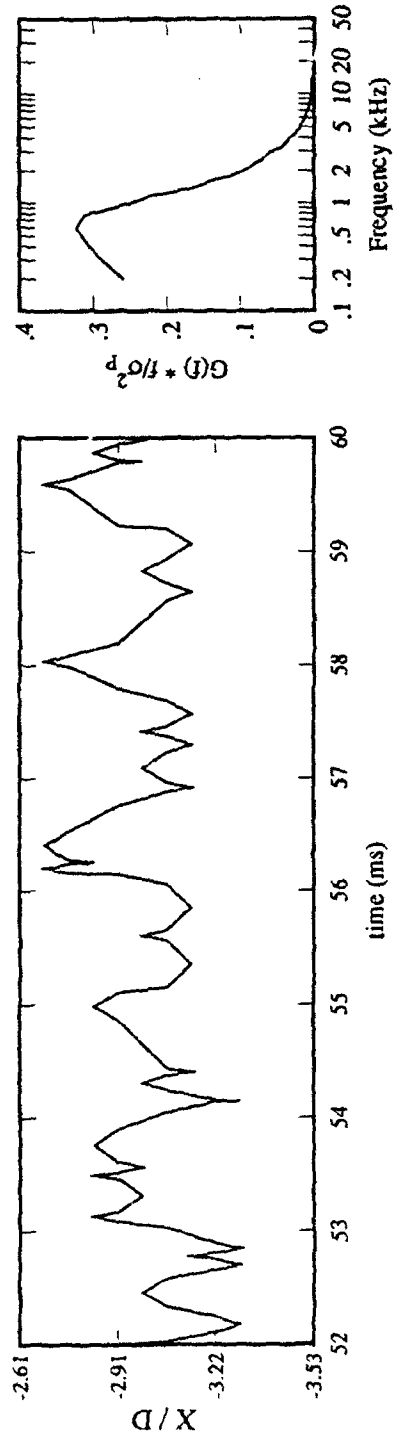
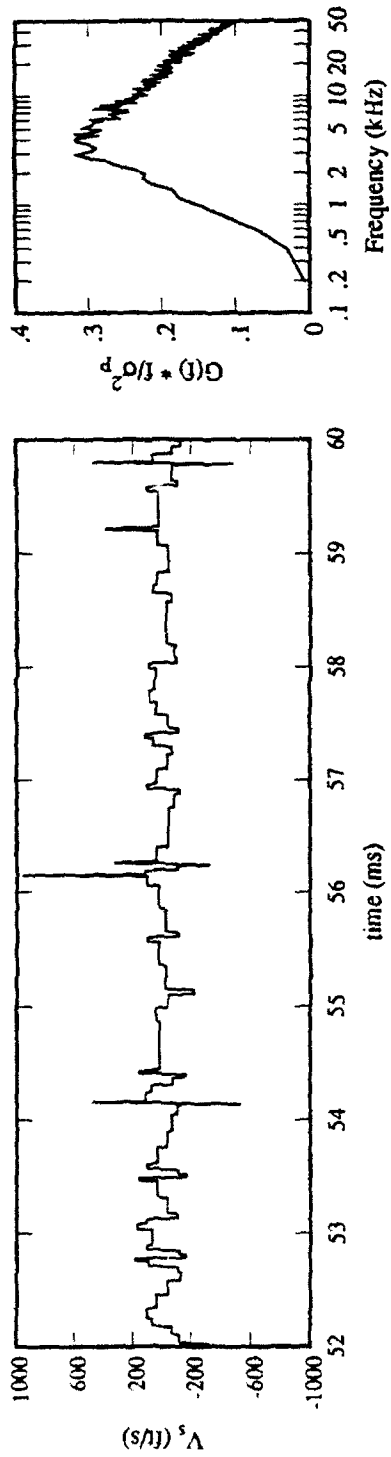
Blunt Fin-Induced Interaction Zero Crossing Frequencies



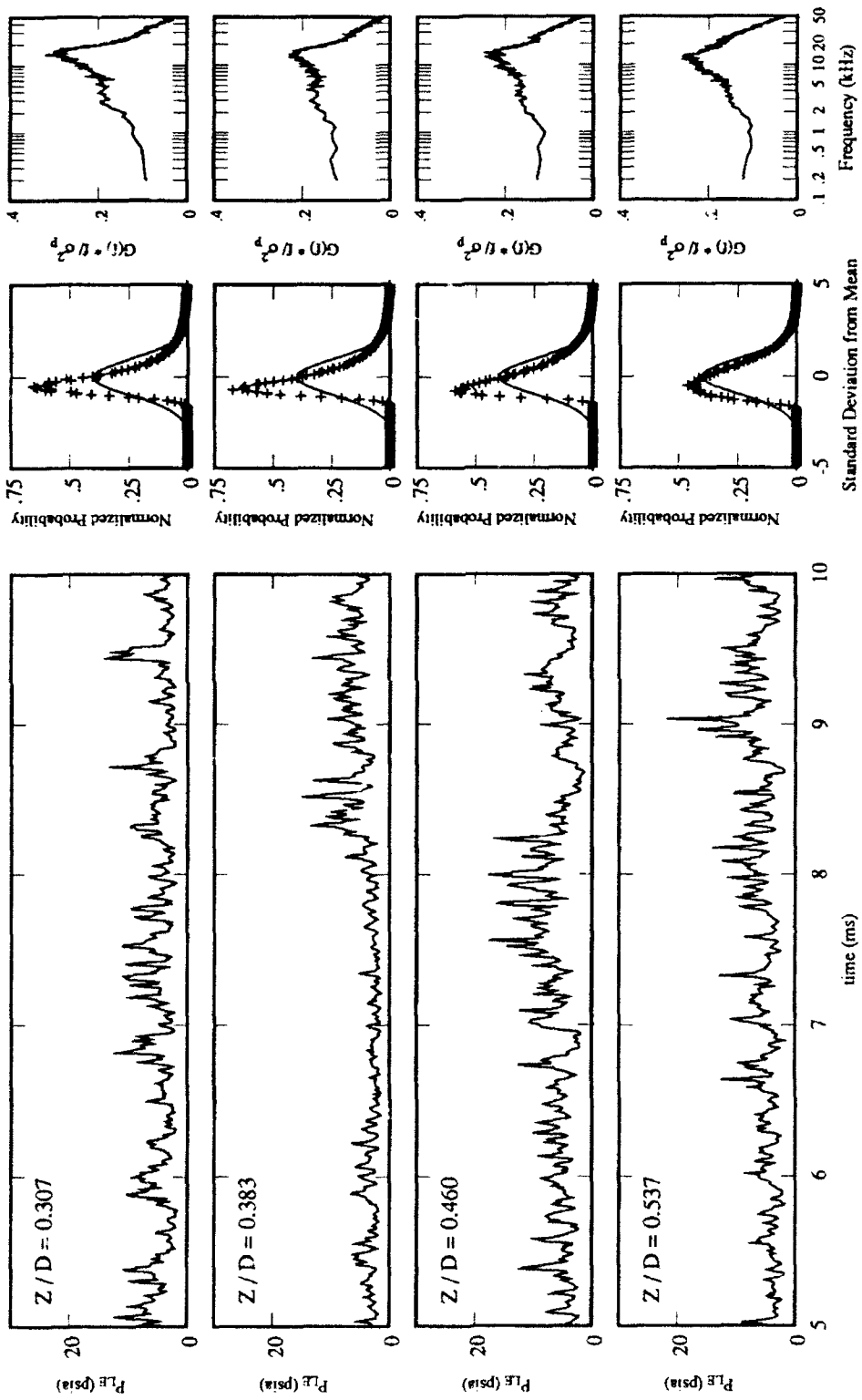
Blunt Fin-Induced Interaction Intermittencies



5-12: Blunt Fin Interaction Intermittency and Zero Crossing Frequency Profiles

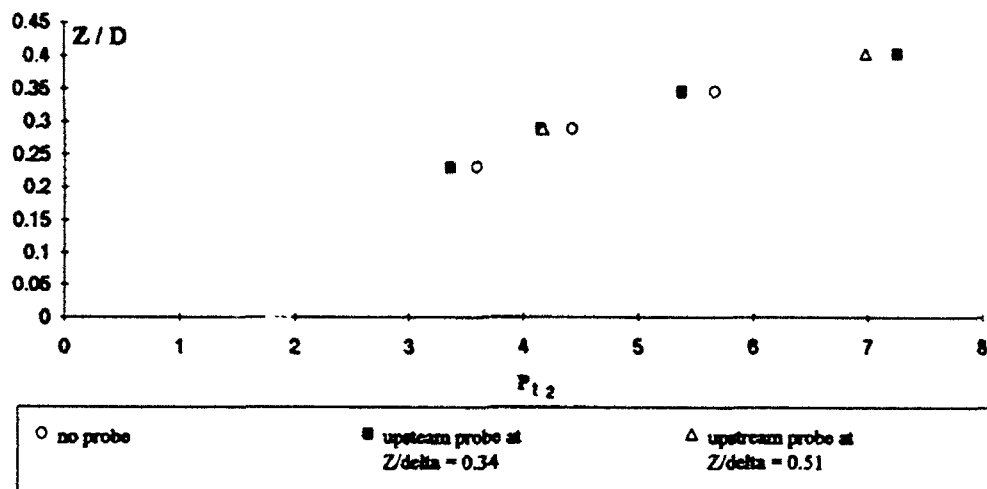


5-13: Characteristic Separation Shock Position and Velocity Histories and PSDs

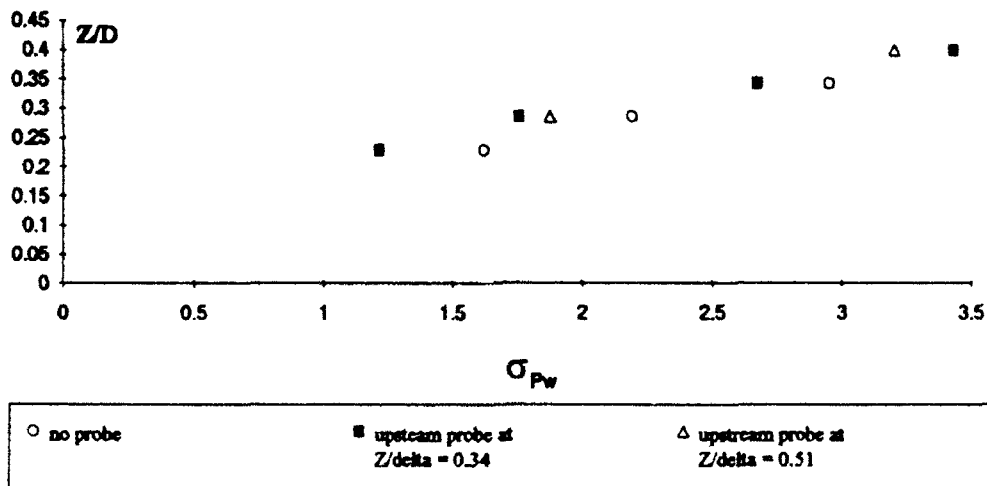


5-14: Leading Edge Surface Pressures - Raw Data Signals, PDDs, and PSDs; No Upstream Probe

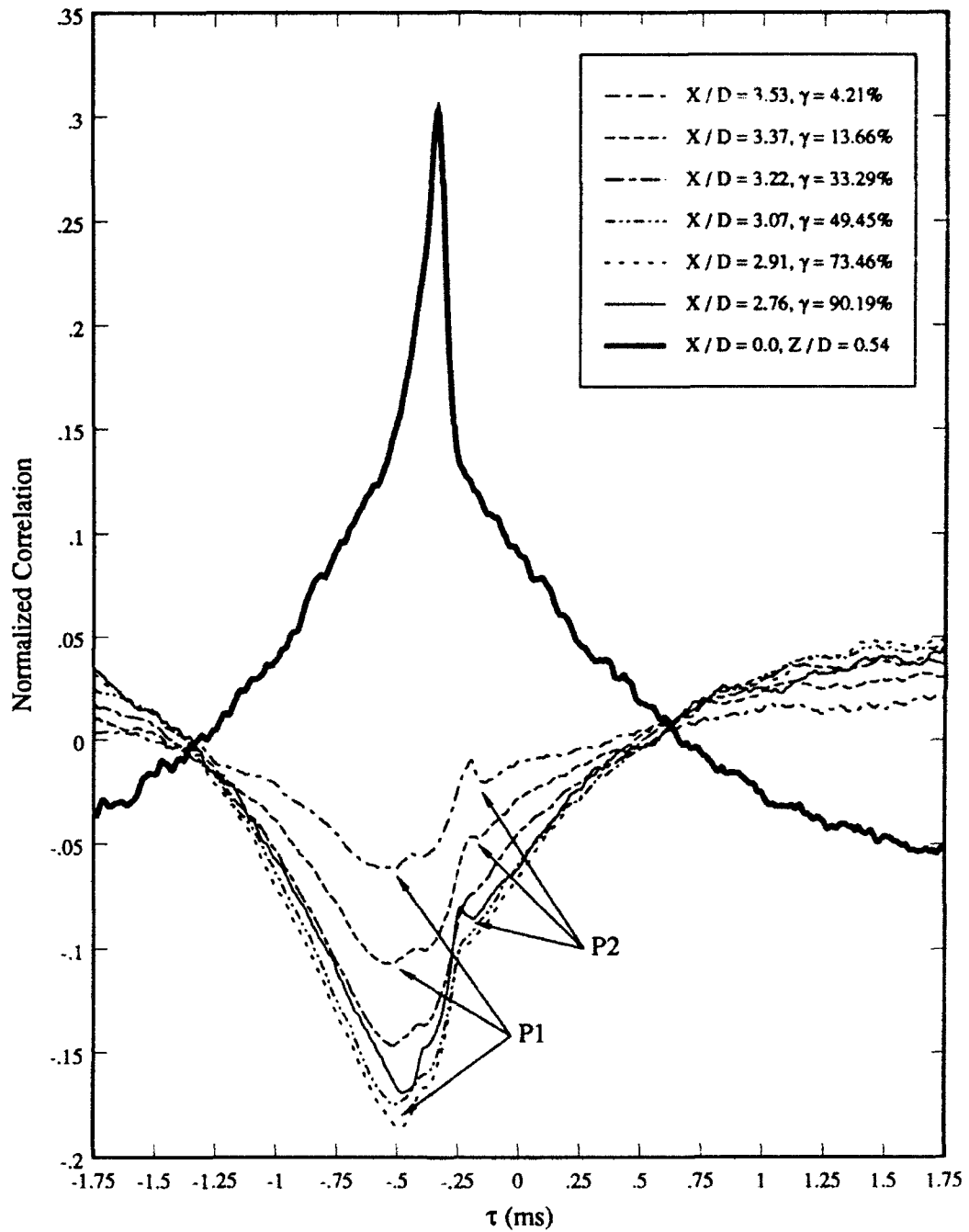
Mean Pressure Distribution



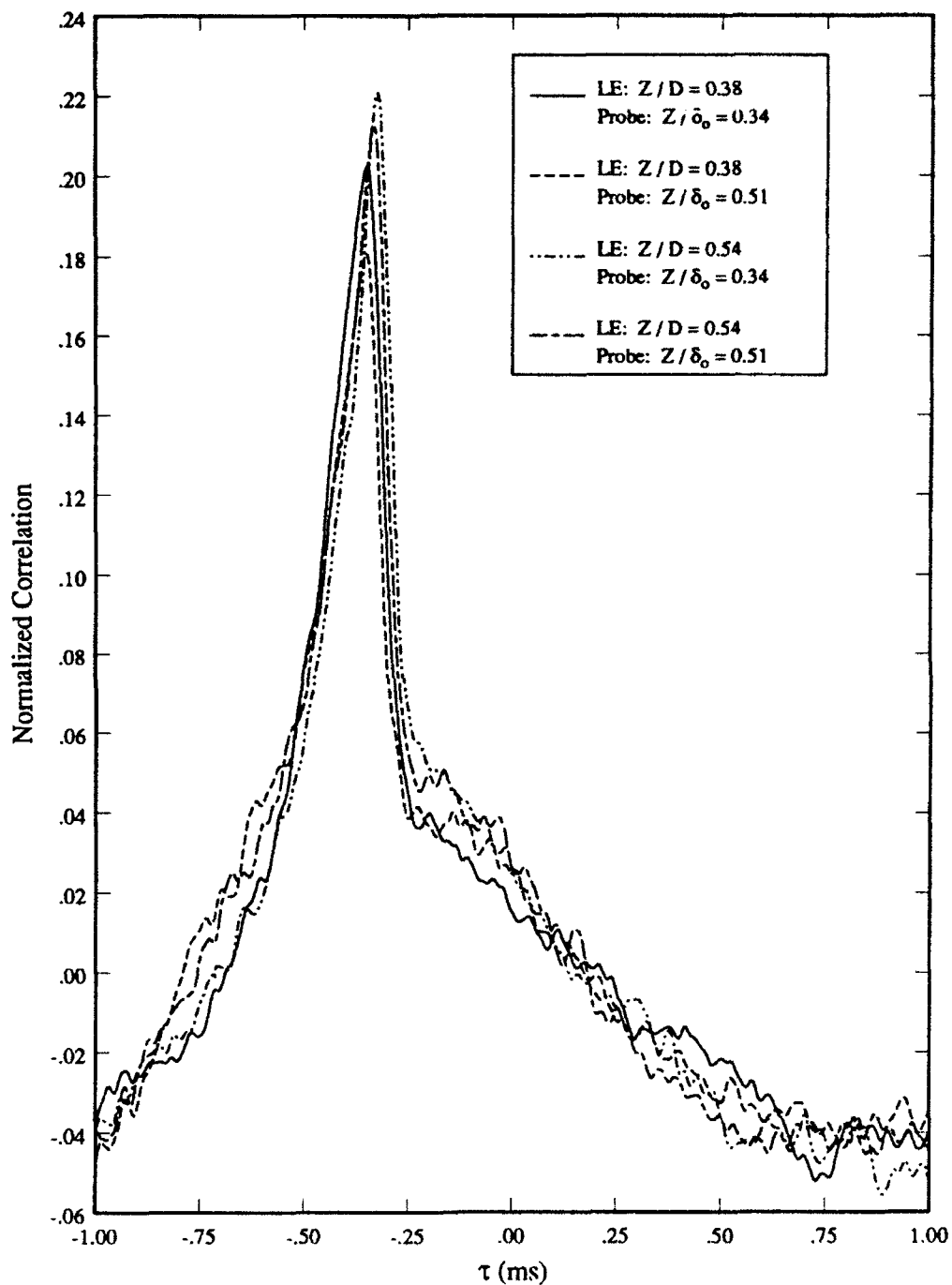
RMS Pressure Distribution



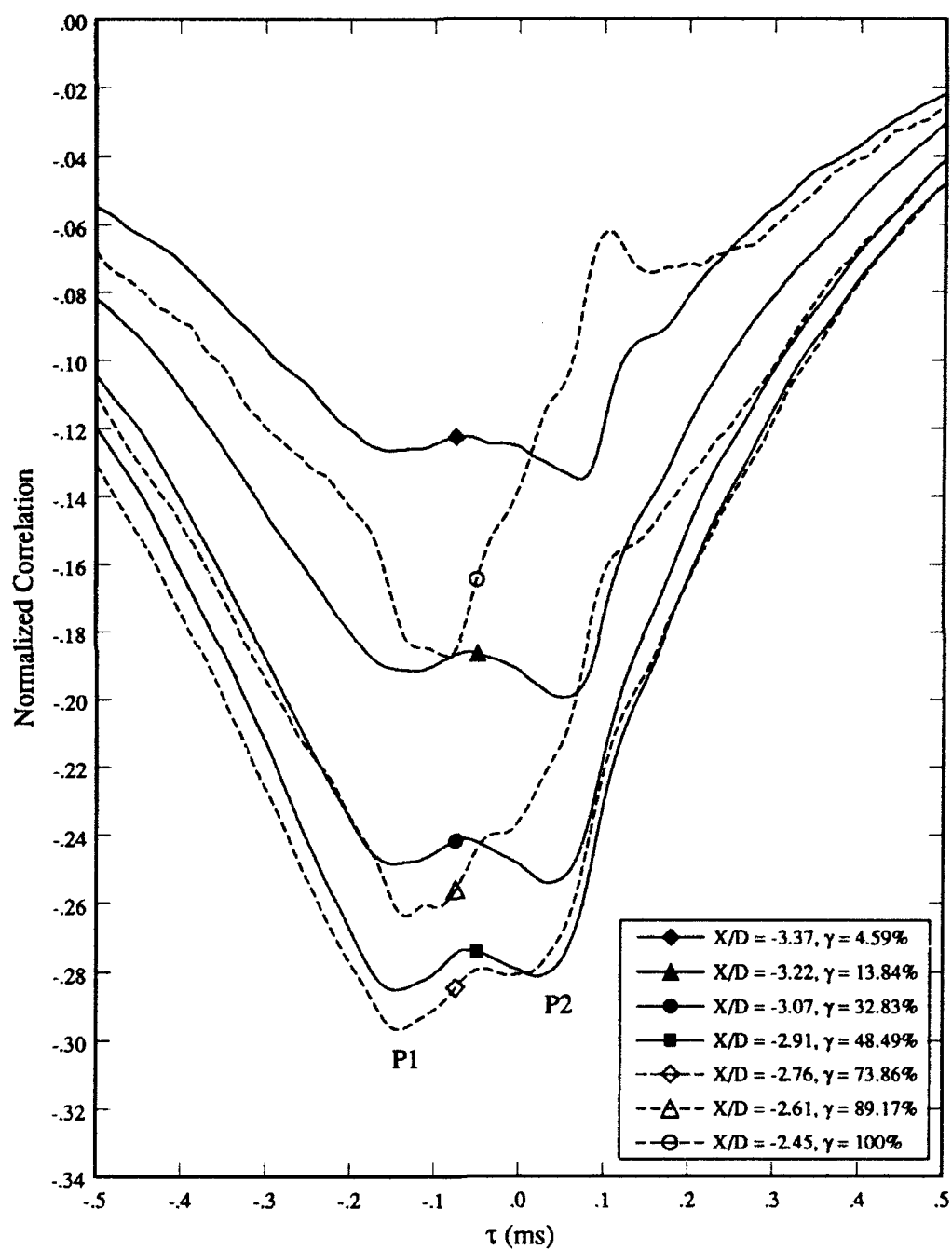
5-15: Blunt Fin Leading Edge Mean and RMS Pressures



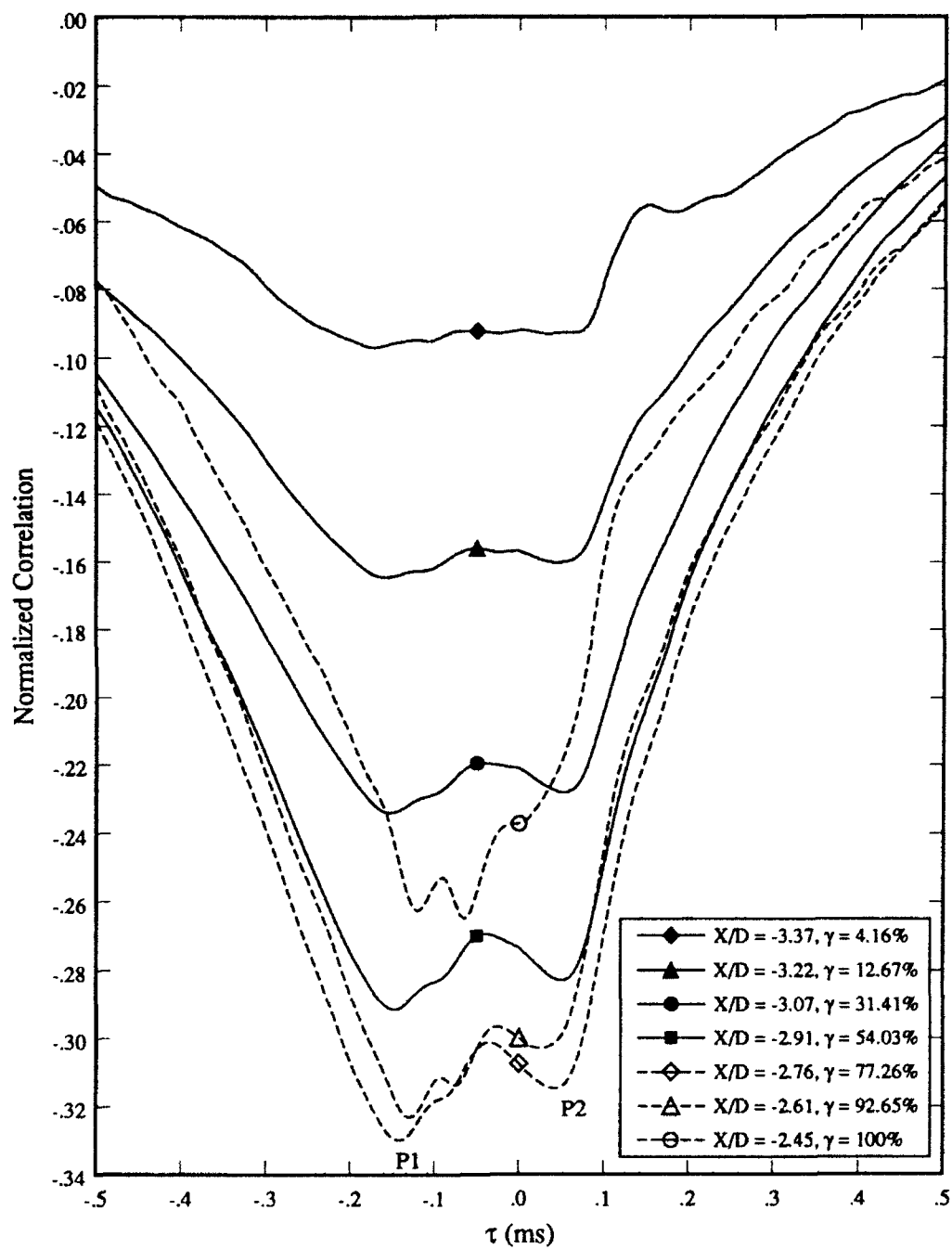
5-16: Cross-Correlations Between Fluctuating Intermittent Region / Fin Leading Edge Surface Pressures and the Fluctuating Pitot Pressure at $X/D = -10.73$, $Z/\delta_o = 0.51$



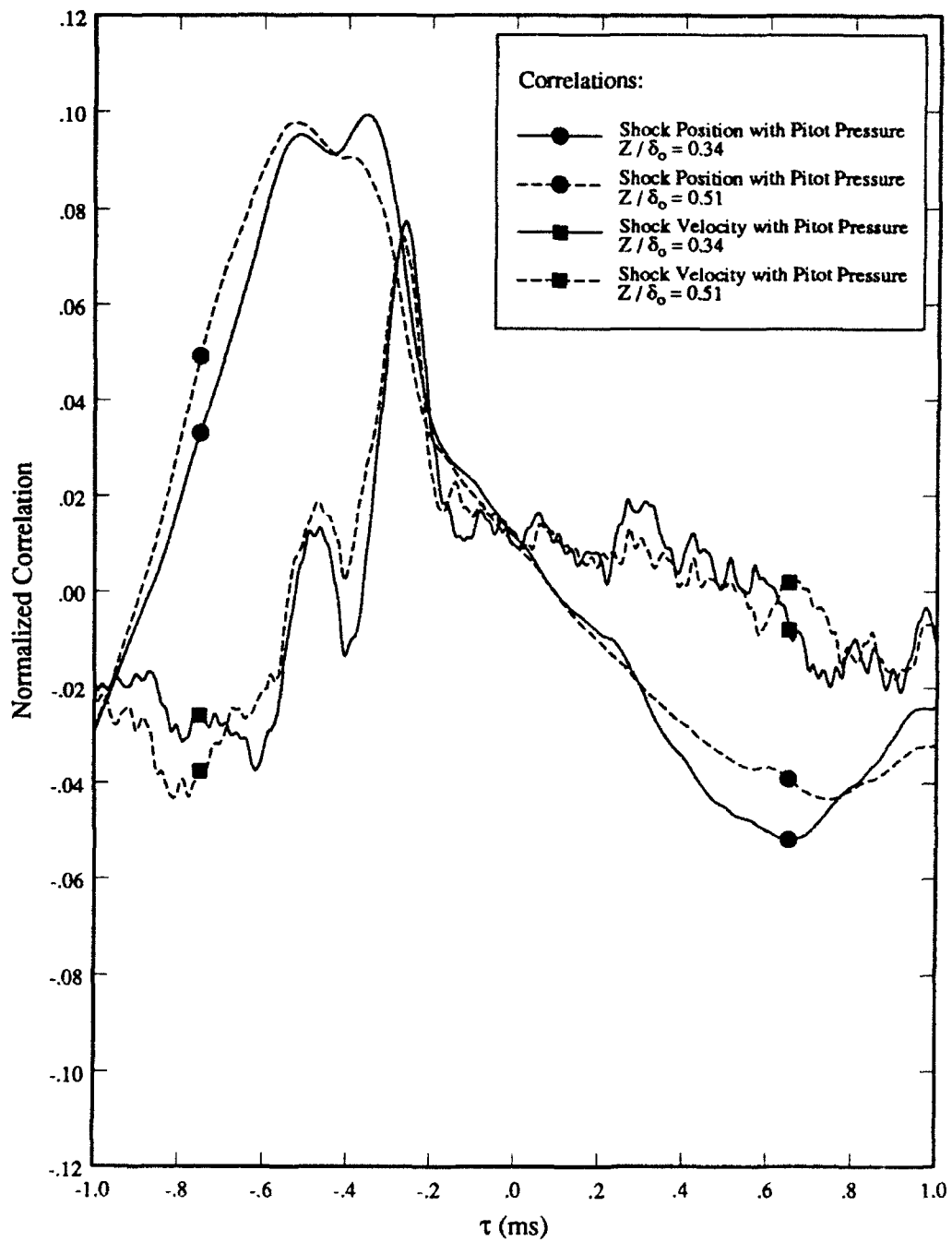
5-17: Cross-Correlation Between Fluctuating Surface Pressures at the Fin Leading Edge and Pitot Pressure Fluctuations at $X/D = -10.73$



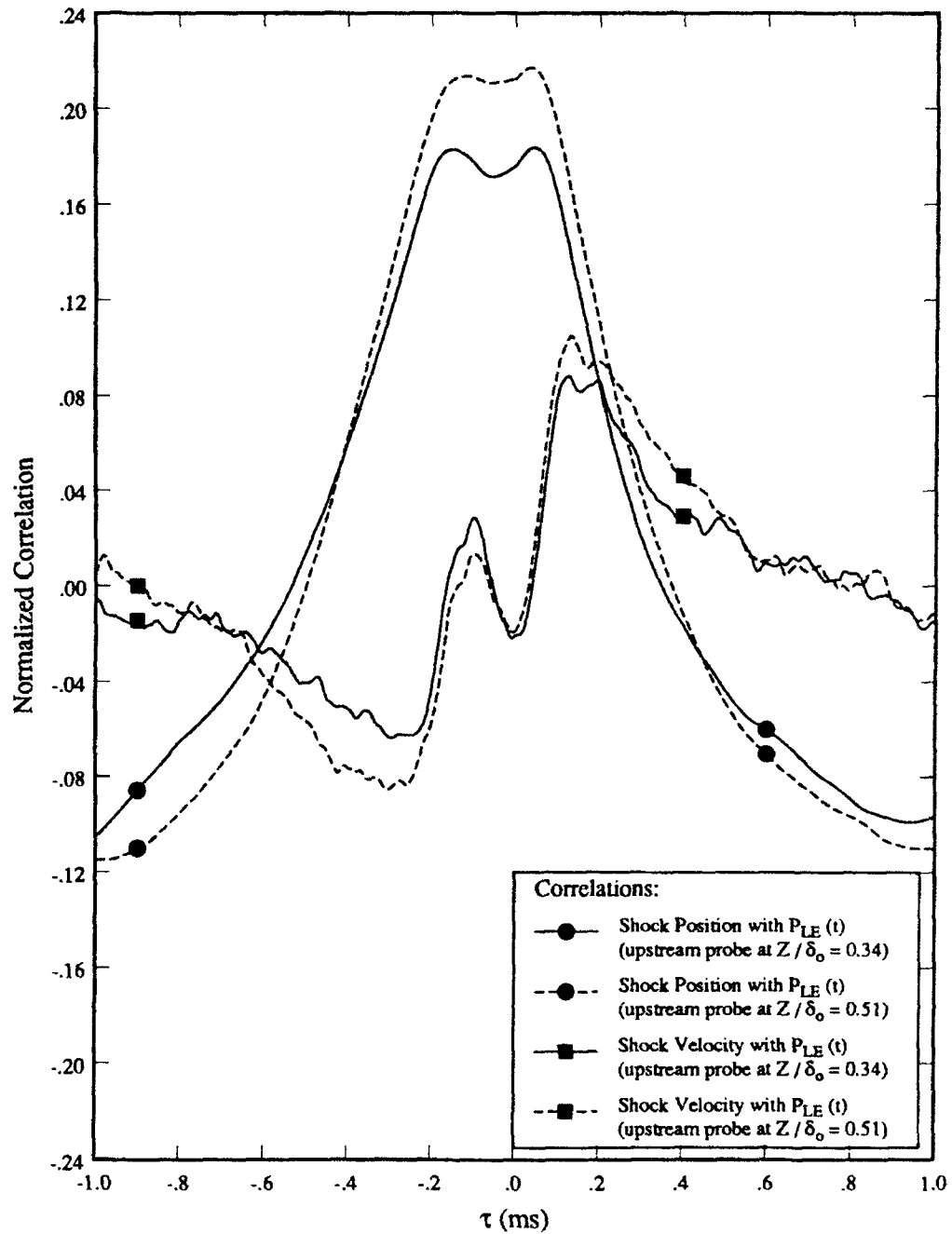
5-18: Cross-Correlations Between Intermittent Region Fluctuating Wall Pressures and Leading Edge Fluctuating Surface Pressure at $Z/D = 0.54$



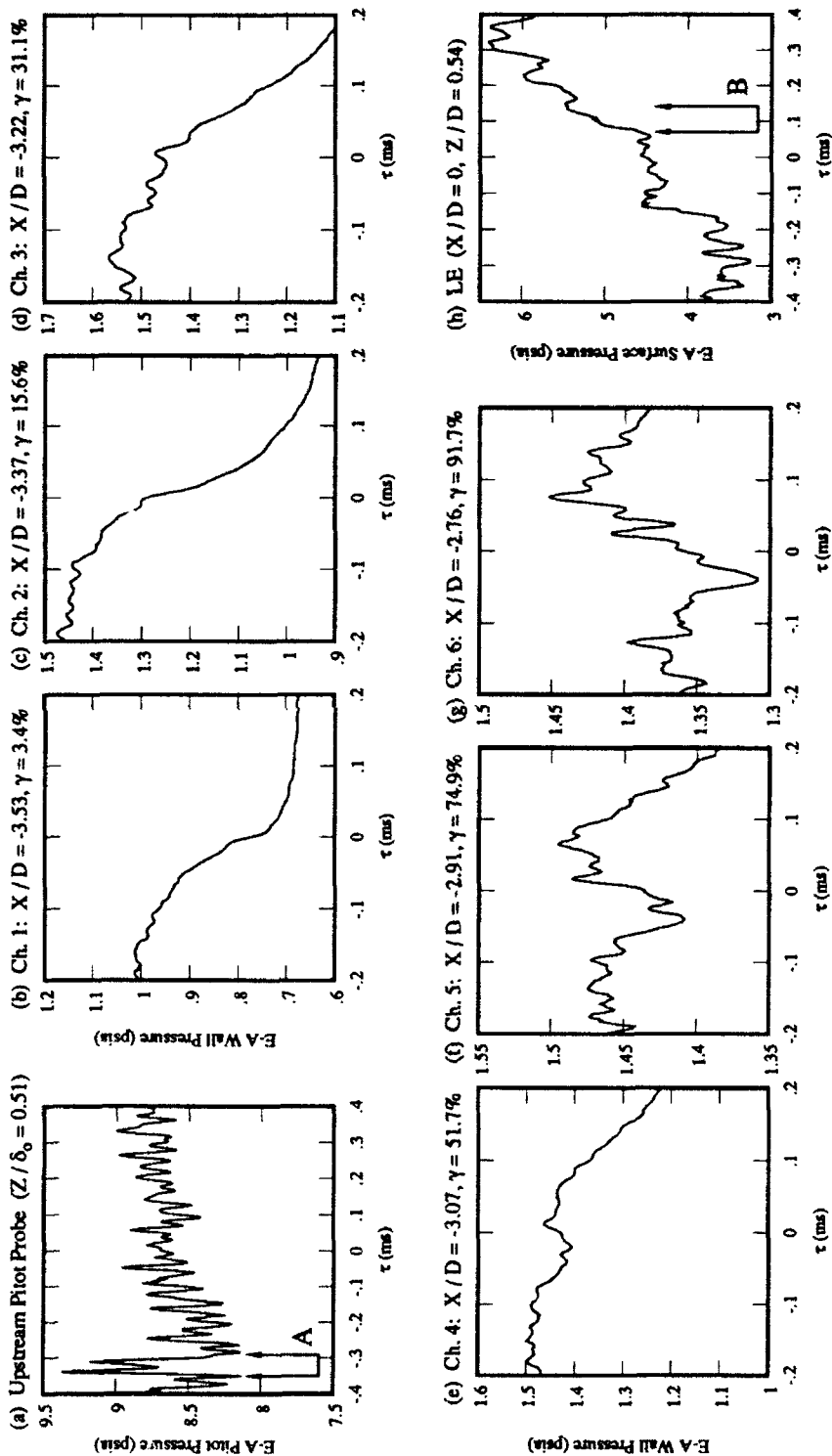
5-19: Cross-Correlations Between Intermittent Region Fluctuating Wall Pressures and Leading Edge Fluctuating Surface Pressures at $Z/D = 0.40$



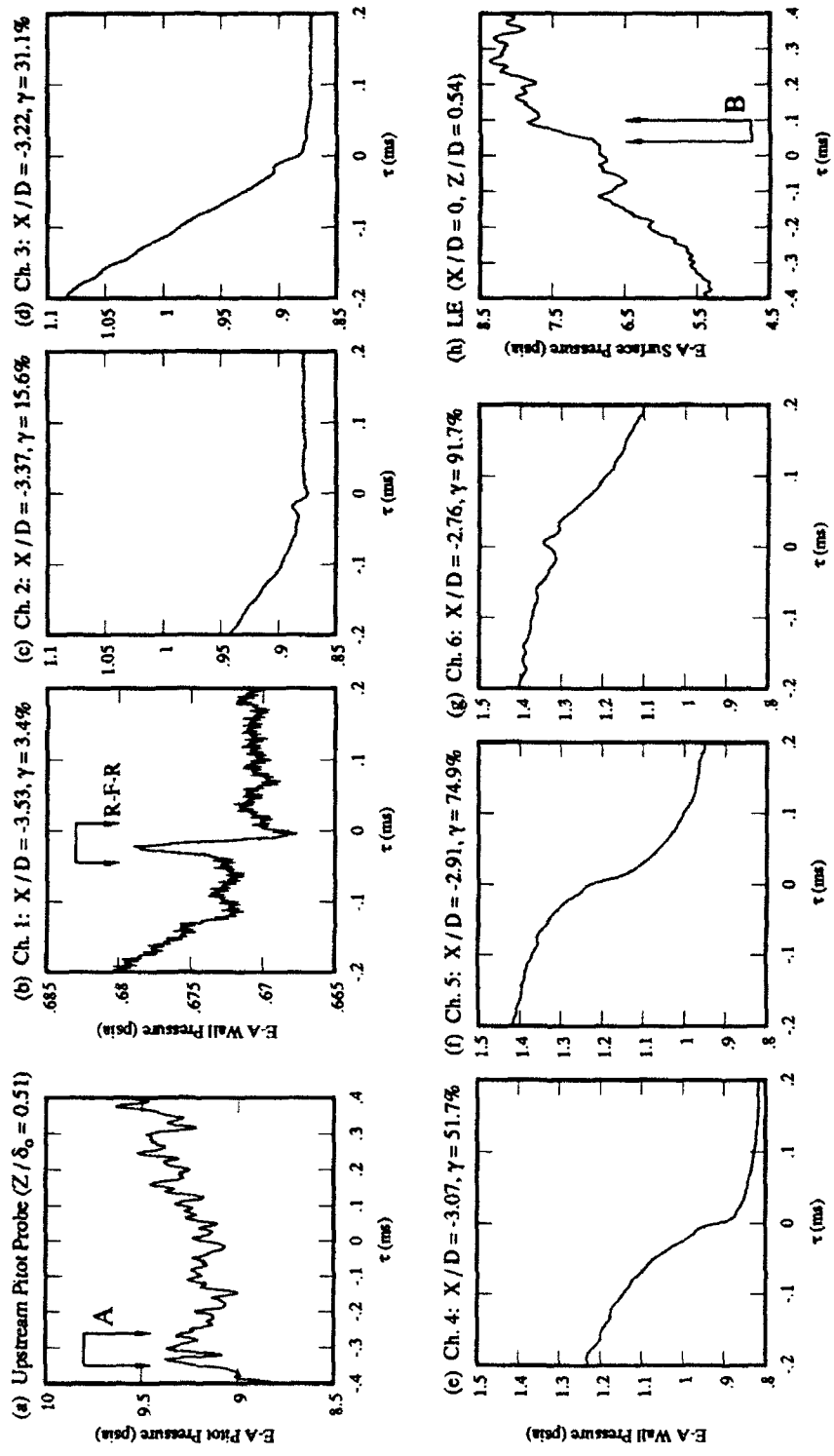
5-20: Cross-Correlations Between Separation Shock Dynamics and Fluctuating Pitot Pressures at $X / D = -10.73$



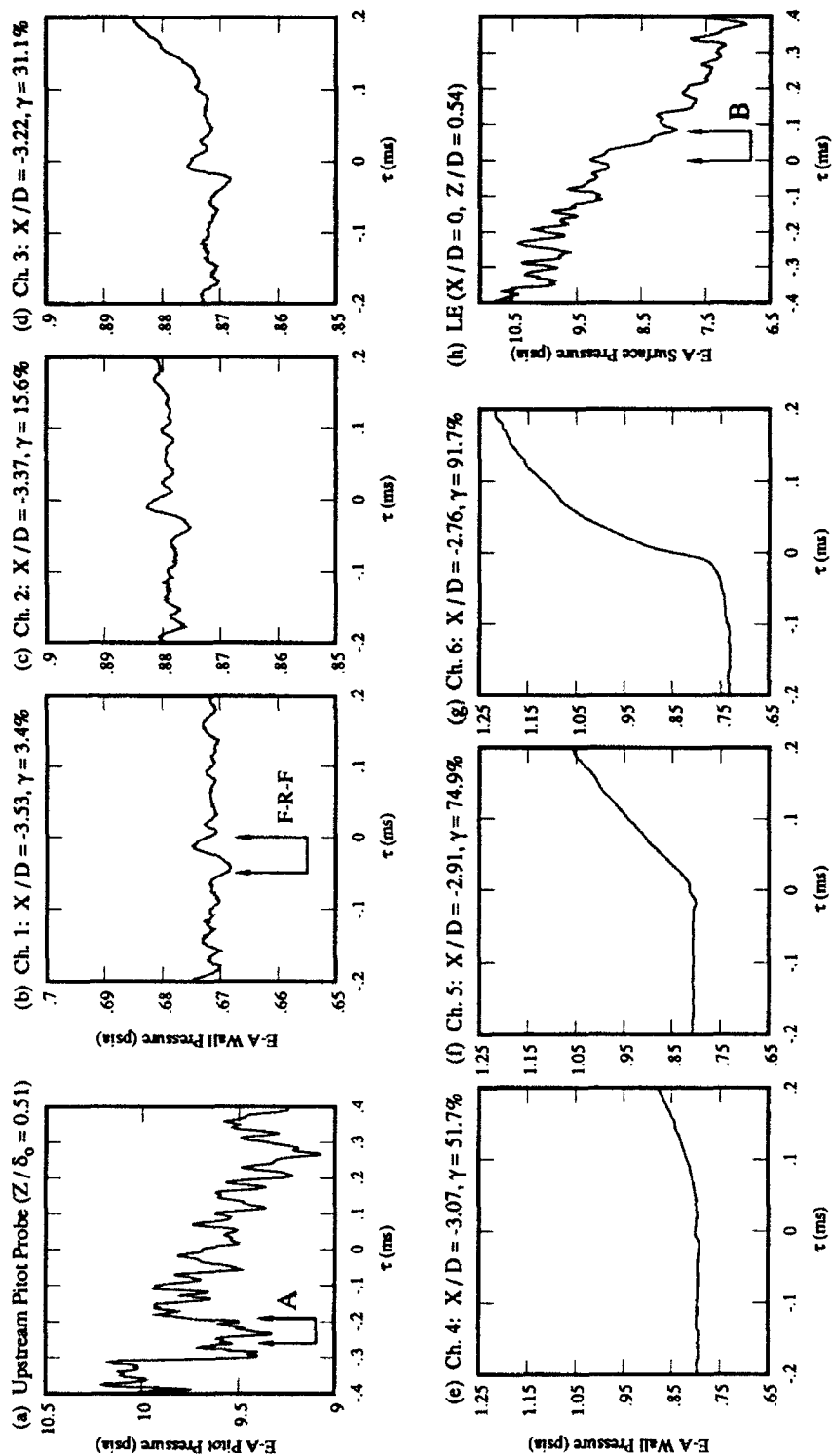
5-21: Cross-Correlations Between Separation Shock Dynamics and Fluctuating Fin Leading Edge Surface Pressures at $Z/D = 0.38$



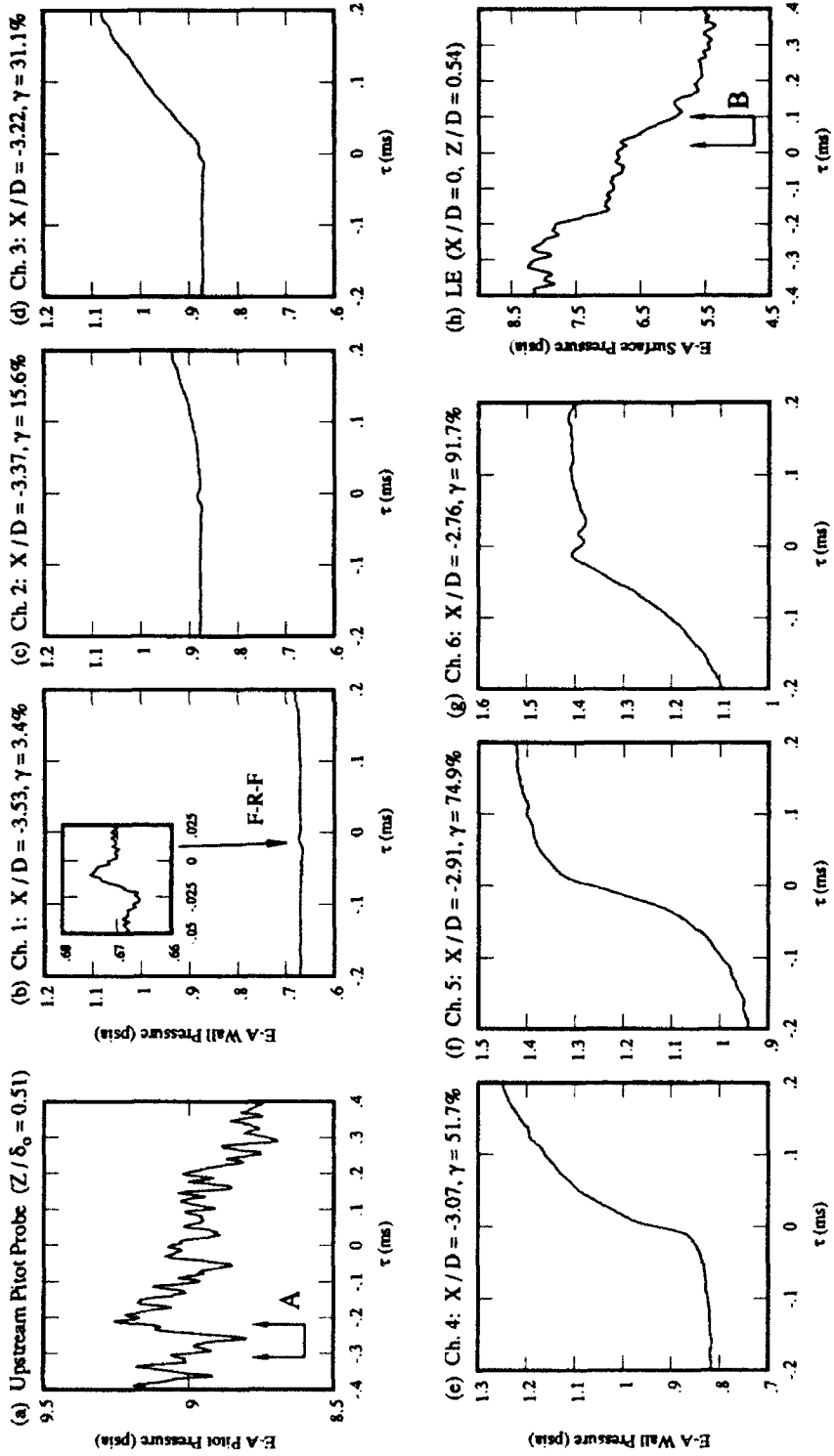
5-22: Ensemble-Averaged Pressure Histories, Downstream Sweep Over Channel 1



5-23: Ensemble-Averaged Pressure Histories, Downstream Sweep Over Channel 4



5-24: Ensemble-Averaged Pressure Histories, Upstream Sweep Over Channel 6



5-25: Ensemble-Averaged Pressure Histories, Upstream Sweep Over Channel 4

REFERENCES

1. Alvi, F.S. and Settles, G.S. (1990), "Structure of Swept Shock Wave / Turbulent Boundary Layer-Interactions Using Conical Shadowgraphy," AIAA Paper 90-1644, 21st Fluid and Plasma Dynamics Conference, Seattle, Washington, June 1990.
2. Alvi, F.S. and Settles, G.S. (1991), "A Physical Model of the Swept Shock / Boundary-Layer Interaction Flowfield," AIAA Paper 91-1768, 22nd Fluid Dynamics, Plasma Dynamics and Lasers Conference, Honolulu, Hawaii, June 1991.
3. Andreopoulos, J. and Muck, K.C. (1987), "Some New Aspects of the Shock- Wave / Boundary-Layer Interaction in Compression-Ramp Flows," *Journal of Fluid Mechanics*, Vol. 180, pp. 405-428.
4. Aso, S., Kuranaga, S. and Hayashi, M. (1991), "Detailed Measurements on Unsteady Properties in Three Dimensional Shock Wave / Turbulent Boundary Layer Interaction Induced by Blunt Fin at Mach Number 4," AIAA Paper 91-1755, 22nd Fluid Dynamics, Plasma Dynamics and Lasers Conference, Honolulu, Hawaii, June 1991.
5. Bendat, J.D. and Piersol, A.G. (1986), Random Data Analysis and Measurement Procedures, 2nd Ed, John Wiley and Sons, New York, 1986.
6. Blackwelder, R.F. and Kaplan, R.E. (1976), "On Wall Structure of the Turbulent Boundary Layer," *Journal of Fluid Mechanics*, Vol. 76, pp. 89-112.

7. Brusniak, L. (1991), "Experimental Investigation of the Driving Mechanism of the Unsteady Separation Shock Motion in a Cylinder-Induced Hypersonic Interaction," M.S. Thesis, Department of Aerospace Engineering and Engineering Mechanics, University of Texas at Austin, May 1991.
8. Brusniak, L. (1993), Private Communication, April 1993.
9. Brusniak, L. and Dolling, D.S. (1993), "Flowfield Dynamics in Blunt Fin-Induced Shock Wave Turbulent Boundary-Layer Interactions," AIAA Paper 93-3133, 24th Fluid Dynamics Conference. Orlando, Florida, July 1993.
10. Burcham, F.W. and Nugent, J. (1970), "Local Flow Field Around a Pylon-Mounted Dummy Ramjet on the X-15-2 Airplane for Mach Numbers From 2.0 to 6.7," NASA TN D-5638, Feb. 1970.
11. Das, D.K. (1987), "A Numerical Study of Turbulent Separated Shear Flows," American Society of Mechanical Engineers Forum on Turbulent Flows, FED Vol. 51, pp. 85-90.
12. Dolling, D.S. (1993a), "Fluctuating Loads in Shock Wave / Turbulent Boundary Layer Interaction: Tutorial and Update," AIAA Paper 93-0284, 31st Aerospace Sciences Meeting and Exhibit, Reno, Nevada, January 1993.
13. Dolling, D.S. (1993b), Private Communication, March 1993.
14. Dolling, D.S. and Bogdonoff, S.M. (1981), "An Experimental Investigation of the Unsteady Behavior of Blunt Fin-Induced Shock Wave Turbulent Boundary Layer Interactions," AIAA Paper 81-1287, 14th Fluid and Plasma Dynamics Conference, Palo Alto, California, June 1981.

15. Dolling, D.S. and Bogdonoff, S.M. (1982), "Blunt Fin-Induced Shock Wave / Turbulent Boundary-Layer Interaction," *AIAA Journal*, Vol. 20, December 1982, pp. 1674-1680.
16. Dolling, D.S., Brusniak, L., Erengil, M.E. and McClure, W.B. (1992), "Algorithms for Analysis of Unsteady Shock-Induced Turbulent Separated Flows," 77th Supersonic Tunnel Association Meeting, University of Notre Dame, April 1992.
17. Dolling, D.S. and Smith, D.R. (1989), "Separation Dynamics in Mach 5 Turbulent Interactions Induced by Cylinders," *AIAA Journal*, Vol. 27, No. 12, June 1989, pp. 734-742.
18. Edney, B. (1968), "Anomalous Heat Transfer and Pressure Distributions on Blunt Bodies at Hypersonic Speeds in the Presence of an Impinging Shock," Aeronautical Research Institute of Sweden, Stockholm, Sweden, Report 115, February 1968.
19. Erengil, M.E. (1989), "Separation Shock Motion and Ensemble Averaged Wall Pressures in a Mach 5 Compression Ramp Interaction," M.S. Thesis, Dept. of Aerospace Engineering and Engineering Mechanics, The University of Texas at Austin, August 1989.
20. Erengil, M.E. (1993), Private Communication, May 1993.
21. Erengil, M.E. and Dolling, D.S. (1991), "Correlation of Separation Shock Motion with Pressure Fluctuations in the Incoming Boundary Layer," *AIAA Journal*, Vol. 29, November 1991, pp. 1868-1877.
22. Erengil, M.E. and Dolling, D.S. (1993a), "Effects of Sweepback on Unsteady Separation in Mach 5 Compression Ramp Interactions," *AIAA Journal*, Vol. 31, February 1993, pp. 303-311.

23. Erenkil, M.E. and Dolling, D.S. (1993b), "Physical Causes of Separation Shock Unsteadiness in Shock Wave / Turbulent Boundary-Layer Interactions," AIAA Paper 93-3134, 24th Fluid Dynamics Conference, Orlando, Florida, July 1993.
24. Gibson, B.T. (1990), "An Experimental Study of Wall Pressure Fluctuations Near Separation in a Mach 5, Sharp Fin-Induced Turbulent Interaction," M.S. Thesis, Department of Aerospace Engineering and Engineering Mechanics, University of Texas at Austin, August 1990.
25. Gibson, B.T. and Dolling, D. S. (1991), "Wall Pressure Fluctuations Near Separation in a Mach 5, Sharp Fin-Induced Turbulent Interaction," AIAA Paper 91-0646, 29th Aerospace Sciences Meeting, Reno, Nevada, January 1991.
26. Gonzalez, J. and Dolling, D.S. (1993), "Effects of Interaction Sweepback on the Dynamics of Shock-Induced Turbulent Separation," AIAA Paper 93-0776, 31st Aerospace Sciences Meeting, Reno, Nevada, January 1993.
27. Gramann, R.A. and Dolling, D.S. (1990), "Dynamics of Separation in a Mach 5 Unswept Compression Ramp Flow," AIAA Paper 90-0380, AIAA 28th Aerospace Sciences Meeting, Reno, Nevada, January 1990.
28. Kleifges, K. (1993), "An Experimental Investigation of the Effects of Leading Edge Geometry on the Dynamics of Blunt Fin-Induced Shock Wave Turbulent Boundary Layer Interaction," M.S. Thesis, Department of Aerospace Engineering and Engineering Mechanics, University of Texas at Austin, May 1993.

29. Knight, D.D., Horstman, C.C., Shapey, B. and Bogdonoff, S.M. (1987), "Structure of Supersonic Turbulent Flow Past a Sharp Fin," *AIAA Journal*, Vol. 25, November, 1987, pp. 1331-1337.
30. Kussoy, M.I. and Horstman, K.C. (1993), "Three-Dimensional Hypersonic Shock Wave/Turbulent Boundary-Layer Interactions," *AIAA Journal*, Vol. 31, January 1993, pp. 8-9.
31. Lakshamanan, B. and Tiwari, S.N. (1993), "Study of Supersonic Intersection Flowfield at modified Wing-Body Junctions," *AIAA Journal*, Vol. 31, May, 1993, pp. 877-883.
32. McClure, W.B. (1991), Unpublished boundary layer properties measured in the Balcones Research Center Mach 5 Wind Tunnel, The University of Texas at Austin, October 1991.
33. McClure, W.B. (1992), "An Experimental Study of the Driving Mechanism and Control of the Unsteady Shock-Induced Turbulent Separation in a Mach 5 Compression Corner Flow," Ph.D. Dissertation, Department of Aerospace Engineering and Engineering Mechanics, The University of Texas at Austin, August 1992.
34. Pozefsky, P., Blevins, R.D. and Laganelli, A.L. (1989), "Thermo-Vibro-Acoustic Loads and Fatigue of Hypersonic Flight Vehicle Structures," AFWAL TR-89-3014, February 1989.
35. Rodi, P., Dolling, D.S. and Knight, D.D. (1991), "An Experimental/Computational Study of Heat Transfer in Sharp Fin Induced Turbulent Interactions at Mach 5," AIAA Paper 91-1764, 22nd Fluid Dynamics, Plasma Dynamics, and Lasers Conference, Honolulu, Hawaii, June 1991.

36. Schmisser, J.D., and Dolling, D.S. (1992), "Unsteady Separation in Sharp Fin-Induced Shock Wave / Turbulent Boundary Layer Interaction at Mach 5," AIAA Paper 92-0748, 30th Aerospace Sciences Meeting, Reno, Nevada, January 1992.
37. Schmisser, J.D. (1992), "An Experimental Study of Fluctuating Wall Pressures in a Highly Swept, Sharp Fin-Induced, Mach 5 Shock Wave / Turbulent Boundary Layer Interaction," M.S. Thesis, Department of Aerospace Engineering and Engineering Mechanics, University of Texas at Austin, May 1992.
38. Settles, G.S., and Dolling, D.S. (1986), "Swept Shock Wave / Boundary-Layer Interactions," *AIAA Progress in Astronautics and Aeronautics: Tactical Missile Aerodynamics*, M. Hemsch and J. Nielsen, eds., Vol. 104, AIAA, New York, 1986, pp. 297-379.
39. Settles, G.S., and Dolling, D.S. (1990), "Swept Shock / Boundary-Layer Interactions - Tutorial and Update," AIAA Paper 90-0375, 28th Aerospace Sciences Meeting, Reno, Nevada, January 1990.
40. Settles, G.S., and Lu, F.K. (1985), "Conical Symmetry of Shock Wave Boundary Layer Interactions Generated by Swept and Unswept Fins," *AIAA Journal*, Vol. 23, July 1985, pp. 1021-1027.
41. Sun, C.-C. and Childs, M.E. (1973), "A Modified Wall Wake Velocity Profile for Turbulent Compressible Boundary Layers," *AIAA Journal of Aircraft*, Vol. 10, June 1973, pp. 381-384.

42. Tran, T.T., Tan, D.K.M., and Bogdonoff, S.M. (1985), "Surface Pressure Fluctuations in a Three-Dimensional Shock Wave / Turbulent Boundary Layer Interaction at Various Shock Strengths," AIAA Paper 85-1562, 18th Fluid Dynamics and Plasma Dynamics and Lasers Conference, Cincinnati, Ohio, July 1985.
43. Tran, T.T. (1987), "An Experimental Investigation of Unsteadiness in Swept Shock Wave/Turbulent Boundary Layer Interactions," Ph.D. Dissertation, Mechanical and Aerospace Engineering Department, Princeton University, March 1987.
44. Zorumski, W.E. (1987), "Fluctuating Pressure Loads Under High Speed Boundary Layers," NASA TM-100517, October 1987.
45. Zubin, M.A., and Ostapenko, N.A. (1979), "Structure of Flow in the Separation Region Resulting from Interaction of a Normal Shock Wave with a Boundary Layer in a Corner," *Izvestiya Akademii Nauk SSSR, Mekhanika Zhidkosti i Gaza*, Vol. 14, May-June 1979, pp. 51-58.

VITA

Scott Raymond Nowlin was born on May 2, 1970, in Lansing, Michigan, the son of Jon O. and Janet E. Nowlin. After graduating from Carson City High School, Carson City, Nevada, in 1988, he accepted an appointment to the United States Air Force Academy in Colorado Springs, Colorado. He received a commission as a Second Lieutenant in the United States Air Force and was awarded the degree of Bachelor of Science in Aeronautical Engineering as a Distinguished Graduate of the United States Air Force Academy in May of 1992. He entered the Graduate School of the University of Texas the following September.

Permanent address: 4441 Conte Dr.
Carson City, Nevada 89701-6520

This thesis was typed by the author.